

# Nanostructured Conversion-Type Negative Electrode Materials for Low-Cost and High-Performance Sodium-Ion Batteries

Xiujuan Wei, Xuanpeng Wang, Xin Tan, Qinyou An,\* and Liqiang Mai\*

Emerging sodium-ion batteries (SIBs) have attracted a great attention as promising energy storage devices because of their low cost and resource abundance. Nevertheless, it is still a major challenge to develop anode materials with outstanding rate capability and excellent cycling performance. Compared to intercalation-type anode materials, conversion-type anode materials are very potential due to their high specific capacity and low cost. A new insight and summary on the recent research advances on nanostructured conversion-type anode materials for SIBs is provided herein. The corresponding synthesis methods, sodium storage properties, electrochemical mechanisms, advanced techniques on studying the crystal structures, and optimization strategies for high-performance batteries are presented. Finally, the remaining challenges and perspectives for the future development of conversion-type anode materials in the energy storage fields are proposed.

## 1. Introduction

In the past few decades, lithium-ion batteries (LIBs) have been considered as the dominant energy storage devices for applications in portable electronics and electric vehicles because of their environmentally benign, high safety, and relatively high energy density.<sup>[1]</sup> However, the limited lithium source results in the increasing cost of lithium, failing to satisfy the growing requirement for large-scale energy storage applications.<sup>[2]</sup> Recently, sodium-ion batteries (SIBs) have been explored as one of hopeful alternatives to LIBs due to their abundant resource as well as low cost. In comparison with lithium (ionic radius of 76 pm), sodium has a larger ionic radius of 102 pm and atomic mass, which causes a sluggish reaction kinetics and large volume expansion of electrode materials during sodiation/desodiation processes.<sup>[3]</sup> Furthermore, some common materials used for LIBs are not suitable for SIBs. Hence, it is extremely urgent to develop advanced electrode materials for high-performance SIBs.

Dr. X. J. Wei, X. P. Wang, X. Tan, Prof. Q. Y. An, Prof. L. Q. Mai  
State Key Laboratory of Advanced Technology  
for Materials Synthesis and Processing  
International School of Materials Science and Engineering  
Wuhan University of Technology  
Wuhan 430070, P. R. China  
E-mail: anqinyou86@whut.edu.cn; mlq518@whut.edu.cn

 The ORCID identification number(s) for the author(s) of this article can be found under <https://doi.org/10.1002/adfm.201804458>.

DOI: 10.1002/adfm.201804458

As an important component of batteries, negative electrode materials with high specific capacity and long-life cycling property are crucial to increase the overall energy-storage density of cells. Negative electrode materials based on electrochemical reaction mechanisms are categorized into three categories: intercalation, alloying, and conversion.<sup>[4]</sup> Carbon materials and Ti-based oxides are developed as SIB negative electrode materials on the basis of intercalation reaction mechanism.<sup>[5]</sup> For example, Wen et al.<sup>[5a]</sup> reported expanded graphite as excellent SIB negative electrode material. The as-prepared expanded graphite has the long-range-ordered layered structure with large interlayer distance. The capacity of 184 mAh g<sup>-1</sup> is achieved

at 100 mA g<sup>-1</sup> and the corresponding capacity retention is 73.92% after 2000 cycles. The free-standing flexible N-carbon nanofiber (CNF) films fabricated by electrospinning method were reported by Wang et al.<sup>[5b]</sup> As SIB anodes, the obtained N-CNF films exhibit a specific capacity of 210 mAh g<sup>-1</sup> after 7000 cycles at 5 A g<sup>-1</sup>. In addition, Le et al.<sup>[5f]</sup> synthesized the TiO<sub>2</sub> mesostructure-graphene nanocomposite through microwave-assisted approach and investigated its sodium storage properties. A stable specific capacity of 126 mAh g<sup>-1</sup> can be obtained for the 18 000th cycle at 10 C. Although these electrode materials exhibit long-term cycling performance, they deliver limited specific capacity due to intrinsically low theoretical capacities. Alloy-based anode materials, such as tin, antimony, and red phosphorus, can deliver high specific capacities by forming Na-rich compounds.<sup>[6]</sup> However, these materials suffer from huge volume change during cycling, resulting in electrode pulverization and capacity fade.<sup>[7]</sup> Moreover, these pure elements have a high production cost, further hindering their industrial applications. Recently, metal oxides, sulfides, selenides, phosphides, nitrides, and fluorides have been investigated as conversion-type negative electrode materials owing to their high theoretical capacity and low cost.<sup>[8]</sup> For instance, Zhou et al.<sup>[8a]</sup> synthesized porous carbon-encapsulated Fe<sub>3</sub>O<sub>4</sub> and Co<sub>3</sub>O<sub>4</sub> nanocrystals for SIBs. The as-prepared carbon encapsulated metal oxides show superior electrochemical performance. The capacities of 657 and 583 mAh g<sup>-1</sup> can be achieved at a current density of 0.1 A g<sup>-1</sup> for carbon-encapsulated Fe<sub>3</sub>O<sub>4</sub> and Co<sub>3</sub>O<sub>4</sub>, respectively. Xiao et al.<sup>[8b]</sup> designed the Fe<sub>1-x</sub>S nanoparticles (NPs) embedded in carbon nanotubes (Fe<sub>1-x</sub>S@CNTs) and applied them as negative electrode materials for SIBs. The Fe<sub>1-x</sub>S@CNTs electrodes deliver a high specific capacity of 449.2 mAh g<sup>-1</sup> at 0.5 A g<sup>-1</sup>

for the 200th cycle. Over the years, extensive efforts have been carried out to develop and design advanced conversion-type negative electrode materials for SIBs, achieving great advances in improving sodium storage property of these compounds.

In this review, we summarize the recent progresses on nanostructured conversion-type negative electrode materials for SIBs. The synthesis methods and sodium storage performances of conversion-type anodes are listed in Table 1. Moreover, the advanced characterization techniques and optimization strategies are discussed in detail. In addition, the relationship between electrode design and enhanced electrochemical performance is also analyzed. Finally, a summary and perspective on potential research direction for conversion-type anode in emerging SIBs are proposed.

## 2. Advantages and Challenges of Conversion-Type Anode Materials

Conversion-type anodes with multielectron reaction deliver high specific capacities, which are great promising materials for SIBs (Figure 1). Conversion reaction involves the formation and breaking of new chemical bonds during insertion/extraction of Na<sup>+</sup>. Generally, the conventional type of conversion reaction can be written as<sup>[9]</sup>



In which, M represents a transition metal, such as Fe, Co, Ni, Cu, Mn, etc., while X denotes the anionic species (O, S, Se, P, N, F). Compared with intercalation-type materials, the full reduction of the transition metal to metallic state leads to higher theoretical capacities through conversion reaction. For example, Fe<sub>3</sub>O<sub>4</sub> as a representative conversion-type anode is fully reduced by sodium to form Fe and Na<sub>2</sub>O during discharge process, delivering a high theoretical capacity of 924 mAh g<sup>-1</sup>. In addition, the reaction potential of conversion-type anode can be tuned by combining different transition metal cations and the anionic species, which can efficiently ensure the safety of battery.<sup>[10]</sup> Furthermore, many conversion-type anode materials such as Fe<sub>3</sub>O<sub>4</sub> and FeS<sub>2</sub> exist in natural forms, possessing the low production cost.

Although the conversion-type anode materials exhibit many advantages, there are still some challenges due to their low ionic/electronic conductivity, relatively large volume change, and undesirable electrolyte decomposition. The low conductivity may cause poor kinetics and degrade the rate capability. The large volume expansion leads to the pulverization of electrodes, resulting in the fast capacity fading. In addition, the electrolyte decomposition may lead to undesirable resistance growth, affecting the electrochemical performance of electrode materials. Thus, numerous efforts are still needed to make the conversion-type anodes practical alternative materials for SIBs.

## 3. Optimization Strategies

To address the aforementioned challenges, various optimization strategies have been adopted to enhance sodium storage



**Xiujuan Wei** received her B.S. degree in Department of Material and Chemical Engineering from Zhengzhou University of Light Industry in 2013. She is working toward the Ph.D. degree in Wuhan University of Technology. Her current research involves the transitional metal chalcogenides for rechargeable batteries.



**Xuanpeng Wang** received his B.S. degree in School of Materials and Chemical Engineering from Henan University of Urban Construction in 2013. He received his Master degree from School of Materials Science and Engineering from Wuhan University of Technology in 2016. He is currently working toward the

Ph.D. degree in Wuhan University of Technology and his current research focuses on the new-type energy storage materials and devices.



**Liqiang Mai** is Chair Professor of Materials Science and Engineering at Wuhan University of Technology (WUT). He received his Ph.D. from WUT in 2004. He carried out his postdoctoral research in the laboratory of Prof. Zhonglin Wang at Georgia Institute of Technology in 2006–2007 and worked as advanced research

scholar in the laboratory of Prof. Charles M. Lieber at Harvard University in 2008–2011. His current research interests focus on nanowire materials and devices for energy storage.

performance of conversion-type anode materials, including structure design, carbon hybridization, and electrolyte optimization. In particular, nanostructure engineering has been proved to be a promising strategy to improve sodium storage property of electrodes.<sup>[11]</sup> Nanostructured materials can increase active surface area and reduce ion diffusion time, enhancing their reaction kinetics during discharge/charge processes. Furthermore, the hollow/pore structured nanomaterials have been widely studied to alleviate large volume change and enhance the cycling life of conversion-type anode materials.<sup>[12]</sup> In addition,

**Table 1.** A summary of synthesis method and electrochemical performance of conversion-type anodes used in SIBs.

Types of materials	Synthesis method	Morphology	Electrochemical Performance <sup>a)</sup>
$\gamma\text{-Fe}_2\text{O}_3\text{@C}^{[60a]}$	Spray pyrolysis method	3D porous hybrids	740/200th/200 mA g <sup>-1</sup>
$\text{Fe}_2\text{O}_3\text{@N-PCNFs}^{[60b]}$	Electrospinning method	Peapod-like hybrids	806/100th/200 mA g <sup>-1</sup>
$\alpha\text{-Fe}_2\text{O}_3/\text{rGO}^{[40]}$	Microwave method	Nanoparticle hybrids	310/150th/100 mA g <sup>-1</sup>
$\text{MnFe}_2\text{O}_4\text{@C}^{[61]}$	Electrospinning method	Nanofiber composites	360/4200th/2000 mA g <sup>-1</sup>
$\text{CoFe}_2\text{O}_4\text{-PPy}^{[62]}$	Hydrothermal method	Interconnected nanotubes	220/2000th/1000 mA g <sup>-1</sup>
$\text{Co}_3\text{O}_4/\text{C}^{[63a]}$	Interface-modulated method	Yolk-shell dodecahedrons	240/200th/1000 mA g <sup>-1</sup>
$\text{Co}_3\text{O}_4^{[63b]}$	Template-directed method	2D holey nanosheets	300/100th/800 mA g <sup>-1</sup>
$\text{m-Co}_3\text{O}_4^{[64]}$	Template-assisted method	Mesoporous microspheres	416/100th/90 mA g <sup>-1</sup>
$\text{Co}_3\text{O}_4/\text{N-C}^{[66]}$	Sacrificial template method	Hollow polyhedrons	229/150th/1000 mA g <sup>-1</sup>
$\text{CuCo}_2\text{O}_4\text{@C}^{[67c]}$	Electrospinning method	Hybrid films	314/1000th/1000 mA g <sup>-1</sup>
$\text{NiO}^{[69]}$	Solvothermal method	Ultrathin nanosheets	266/100th/1000 mA g <sup>-1</sup>
$\text{CoNiO}_2^{[70]}$	Solvothermal method	Porous nanosheets	746.6/100th/200 mA g <sup>-1</sup>
$\text{CuO}/\text{C}^{[72]}$	Spray pyrolysis method	Micro-nanostructured spheres	402/600th/200 mA g <sup>-1</sup>
$\text{CuO@CMK-8}^{[74]}$	Hydrothermal method	Nanocomposites	477/200th/100 mA g <sup>-1</sup>
$\text{CuO@C}^{[49]}$	Electrospinning method	Nanofibers	401/500th/500 mA g <sup>-1</sup>
$\text{FeS}_2/\text{CNT}^{[76a]}$	Solvothermal method	Network composites	394/400th/200 mA g <sup>-1</sup>
$\text{FeS}/\text{CA}^{[76b]}$	Freeze-drying method	Macroporous hybrids	280/200th/500 mA g <sup>-1</sup>
$\text{FeS}^{[77]}$	Electrospinning method	Porous nanofibers	592/150th/500 mA g <sup>-1</sup>
$\text{CL-C}/\text{FeS}^{[78]}$	Solvothermal method	Microspheres	265/200th/1000 mA g <sup>-1</sup>
$\text{Fe}_{1-x}\text{S}^{[79]}$	Sulfurization method	Porous structure	563/200th/100 mA g <sup>-1</sup>
$(\text{Fe}_{0.5}\text{Ni}_{0.5})_9\text{S}_8^{[59]}$	Spray pyrolysis method	Yolk-shell structure	527/100th/1000 mA g <sup>-1</sup>
$\text{Co}_9\text{S}_8/\text{MoS}_2\text{-CN}^{[18a]}$	Template-assisted method	Yolk-shell structure	438/150th/1000 mA g <sup>-1</sup>
$\text{CNT@CoS@C}^{[80]}$	Bottom-up method	Sandwich-type structure	415/100th/100 mA g <sup>-1</sup>
$\text{CoS@C}^{[81]}$	Template-assisted method	Yolk-shell microspheres	532/100th/200 mA g <sup>-1</sup>
$7\text{-CoS}/\text{C}^{[82]}$	Sulfurization method	Nanorods	542/2000th/1000 mA g <sup>-1</sup>
$\text{CoS@rGO}^{[83]}$	Solvothermal method	Nanoplate composites	420/1000th/1000 mA g <sup>-1</sup>
$\text{CoS}_2^{[85]}$	Solvothermal method	Hollow microstructure	690/100th/1000 mA g <sup>-1</sup>
$\text{CoS}_x^{[17a]}$	Solvothermal method	Hollow structures	572/100th/500 mA g <sup>-1</sup>
$\text{NiS}_x/\text{CNT@C}^{[87]}$	Oil bath method	Hierarchical structure	340/200th/100 mA g <sup>-1</sup>
$\text{NiS}^{[88]}$	Refluxing method	Hollow spheres	499.9/50th/100 mA g <sup>-1</sup>
$\text{NiS}_2^{[89]}$	Hydrothermal method	Mesoporous nanospheres	319/1000th/500 mA g <sup>-1</sup>
$\alpha\text{-MnS@N,S-NTC}^{[90]}$	Hydrothermal method	1D nanostructure	291/200th/250 mA g <sup>-1</sup>
$\text{FeSe}_2^{[15a]}$	Solution-based method	Ultra-small nanoparticles	450/300th/800 mA g <sup>-1</sup>
$\text{FeSe}_2^{[24]}$	Hydrothermal method	Microspheres	372/2000th/1000 mA g <sup>-1</sup>
$\text{FeSe}_2^{[29]}$	Hydrothermal method	Nanorod clusters	515/400th/1000 mA g <sup>-1</sup>
$\text{FeSe}_2\text{@C}^{[92]}$	Selenization method	Hollow nanocubes	450/100th/100 mA g <sup>-1</sup>
$\text{Fe}_7\text{Se}_8\text{@NC}^{[93]}$	Thermal method	Nanoparticles	339/1200th/1000 mA g <sup>-1</sup>
$\text{FeSe@FeS}^{[94]}$	Solid-state method	Core-shell structures	485/1400th/3000 mA g <sup>-1</sup>
$\text{CoSe@carbon NWS}^{[97]}$	Hydrothermal method	Peapod-like nanowires	299/100th/100 mA g <sup>-1</sup>
$\text{CoSe}/\text{C}^{[98]}$	Sacrificial template method	Yolk-shell structures	531.6/50th/500 mA g <sup>-1</sup>
$\text{CoSe}_x\text{-rGO}^{[99]}$	Spray pyrolysis method	Crumple-structured composite	420/50th/300 mA g <sup>-1</sup>
$\text{CoSe}_2\text{@C/CNTs}^{[100]}$	Template-assisted method	Hollow structures	390/1000th/1000 mA g <sup>-1</sup>
$\text{CoSe}_2/\text{C}^{[103]}$	Solid-state method	Cobblestone-like nanospheres	345/10 000th/4500 mA g <sup>-1</sup>
$\text{NiSe}_2^{[104]}$	Template-assisted method	Nanoplates	318/100th/1000 mA g <sup>-1</sup>
$\text{NiSe}_2^{[105]}$	Hydrothermal method	Nanooctahedra	313/4000th/5000 mA g <sup>-1</sup>
$\text{NiSe@C}^{[107]}$	Selenization method	Hollow microspheres	325/45th/300 mA g <sup>-1</sup>

Table 1. Continued.

Types of materials	Synthesis method	Morphology	Electrochemical Performance <sup>a)</sup>
ZnSe/MWCNT <sup>[109]</sup>	Solvothermal method	Microsphere composites	382/180th/500 mA g <sup>-1</sup>
RGO@CoP@C-FeP <sup>[111]</sup>	Phosphorization method	Core-shell structure	456.2/200th/100 mA g <sup>-1</sup>
CoP/CNS <sup>[112]</sup>	Phosphorization method	Nanocomposites	498/200th/100 mA g <sup>-1</sup>
Ni <sub>2</sub> P@cPGN <sup>[115]</sup>	Self-template method	Nanohybrids	161/100th/200 mA g <sup>-1</sup>
Ni <sub>2</sub> P@C/GA <sup>[116]</sup>	Solvothermal method	3D porous structure	253.6/100th/100 mA g <sup>-1</sup>
Cu <sub>3</sub> P <sup>[118]</sup>	Phosphorization method	Nanowires	215.2/100th/200 mA g <sup>-1</sup>

<sup>a)</sup>The electrochemical performance is listed as capacity/cycle number/current density. The unit of capacity is mAh g<sup>-1</sup>.

the configuration of carbon hybridization is another effective approach to enhance the electrical conductivity and mechanical stability of electrodes, improving their rate property and cycling life.<sup>[13]</sup> Apart from the electrode design, the electrolyte composition also plays an important role for optimizing the electrochemical performance of SIBs.<sup>[3,14]</sup> These optimization strategies will be discussed based on the conversion-type anode materials.

### 3.1. Size and Morphology Control

Downsizing active materials to nanoscale can effectively shorten the diffusion length for electron/ion transport, mitigating the poor electronic/ionic conductivities of electrodes.<sup>[15]</sup> Generally, the nanoscale materials including 0D, 1D, and 2D nanomaterials are considered as a class of promising materials for SIBs. The 0D nanomaterials can improve the electrochemical reaction reversibility of conversion-type anode materials. The 1D nanomaterials such as nanowires and nanotubes provide high surface area, fast ion diffusion, and improved electron transport, enhancing the cycling stability and rate performance of anodes. Besides, the 2D nanomaterials offer excellent mechanical flexibility and large surface area for superior sodium storage. Thus, a large number of well-designed nanostructured negative electrode materials have been reported for

SIBs.<sup>[16]</sup> For example, Zhao et al.<sup>[15a]</sup> prepared ultrafine FeSe<sub>2</sub> NPs with a high yield. The ultrafine nanostructure offers the short sodium-ion diffusion pathway and improved stress accommodation. When investigated as SIB negative electrode materials, the FeSe<sub>2</sub> NPs show a high reversible capacity, outstanding rate property, and superior cycling performance. Walter et al.<sup>[15b]</sup> fabricated the FeS<sub>2</sub> nanocrystals by a facile solution-phase chemical synthesis. The as-prepared FeS<sub>2</sub> nanocrystals exhibit a size range of 50–100 nm with high crystalline. Compared with bulk FeS<sub>2</sub>, nanosized FeS<sub>2</sub> shows higher reversible capacity and better rate performance. A high specific capacity of 500 mAh g<sup>-1</sup> can be achieved at 1 A g<sup>-1</sup> after 400 cycles. The calcium vanadate (CaV<sub>4</sub>O<sub>9</sub>) nanowires synthesized through a simple hydrothermal approach followed by heat treatment were reported by Xu et al.<sup>[16b]</sup> Due to high electrical conductivity, small volume variation, and self-preserving effect, the as-prepared CaV<sub>4</sub>O<sub>9</sub> delivers excellent cycling property and superior rate capability for SIBs. In addition, the hierarchical hollow/porous structures offer more active reaction sites and accommodate the large volume expansion for electrodes, which may effectively improve their electrochemical performance.<sup>[17]</sup> Xiao et al.<sup>[17a]</sup> synthesized the CoS<sub>x</sub> hollow structure material through a solvothermal reaction and subsequent annealing process. The transmission electron microscope (TEM) images show that the obtained CoS<sub>x</sub> has uniform hierarchical hollow spheres nanostructure with a size of 150–200 nm. Benefiting from the merits of the nanoarchitecture and hollow structure, the as-prepared hierarchal CoS<sub>x</sub> hollow spheres display high capacity and cycling property. As SIB negative electrode materials, the CoS<sub>x</sub> hollow spheres deliver a high discharge specific capacity of 572 mAh g<sup>-1</sup> at a current density of 500 mA g<sup>-1</sup> after 100 cycles.

### 3.2. Carbon Hybridization

Carbonaceous materials including carbon nanotubes, carbon fibers, and reduced graphene oxide possess high electrical conductivity, which is explored to enhance the reaction kinetics of conversion-type anode materials. Designing hybrids with carbonaceous materials has been considered as one of the most promising methods to enhance

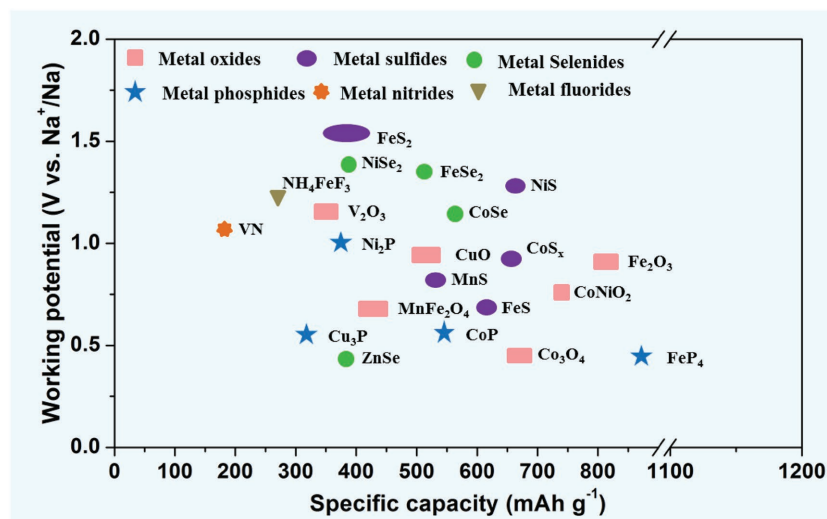


Figure 1. Average working potential versus specific capacity of conversion-type anode materials for SIBs.

sodium storage property of negative electrode materials.<sup>[18]</sup> For example, He et al.<sup>[19]</sup> reported MnO nanoparticles dispersed on the 1D N-doped carbon nanotubes as anode materials for SIBs. Benefiting from the improved specific surface area, enhanced ion diffusion, and increased electron transport, the composites exhibit promising sodium storage performance. Owing to its high electrical conductivity and good mechanical flexibility, 2D graphene sheet has also been studied in SIBs. Du et al.<sup>[20]</sup> prepared Co<sub>3</sub>S<sub>4</sub> porous nanosheets encapsulated in graphene sheets (Co<sub>3</sub>S<sub>4</sub>-PNS/GS) by freeze-drying and hydrazine treatment. The as-prepared Co<sub>3</sub>S<sub>4</sub>-PNS/GS displays sandwich-like architecture, in which the Co<sub>3</sub>S<sub>4</sub> porous nanosheets are evenly distributed between the interlayers of graphene sheets. When evaluated as SIB negative electrode material, the Co<sub>3</sub>S<sub>4</sub>-PNS/GS electrode delivers outstanding rate property and long-life cycling performance. The excellent electrochemical performance can be ascribed to the unique 3D sandwich-type structure improving the electron/ion transport and buffering the large volume change. Recently, iron sulfide-carbon interlocked graphene (Fe<sub>7</sub>S<sub>8</sub>@C-G) composites synthesized by electrostatic interactions and postsulfurization were reported by Huang et al.<sup>[21]</sup> The TEM images indicate that the Fe<sub>7</sub>S<sub>8</sub> nanoparticles are encapsulated by amorphous carbon and interconnected with graphene sheets. The 3D networks increase the interparticle conductivity and buffer the large volume expansion during cycling, thus enhancing the rate property and cycling performance of electrodes. Lin et al.<sup>[22]</sup> synthesized the NiS<sub>2</sub>@CoS<sub>2</sub> nanocrystals encapsulated in N-doped carbon nanocubes (NiS<sub>2</sub>@CoS<sub>2</sub>@C@C) for high-performance SIBs. The obtained NiS<sub>2</sub>@CoS<sub>2</sub>@C@C samples show high specific capacity, superior rate performance, and long-life cycling property, which are attributed to double carbon layer and porous structures.

### 3.3. Electrolyte Optimization

The suitable electrolytes play an important role in improving sodium storage property of conversion-type anode materials. Generally, the conventional carbonate-based electrolytes include ethylene carbonate, dimethyl carbonate, diethyl carbonate, etc. However, the carbonate solvents will react with polysulfides and induce side-reaction with some of conversion-type anode. Therefore, the electrolyte additives and ether-based electrolytes are explored to enhance the cycle life and rate performance of conversion-type anodes.<sup>[23]</sup> For instance, Zhang et al.<sup>[24]</sup> investigated the sodium-ion storage performance of FeSe<sub>2</sub> microspheres using ether-based electrolyte (1 M NaCF<sub>3</sub>SO<sub>3</sub> in diethyleneglycol dimethylether). The results show that the as-prepared FeSe<sub>2</sub> exhibits a discharge capacity of 372 mAh g<sup>-1</sup> after 2000 cycles at 1 A g<sup>-1</sup>, corresponding to the capacity retention of 89.0%. However, the capacity of FeSe<sub>2</sub> decays fast using carbonate-based electrolytes. Su et al.<sup>[25]</sup> reported ZnS nanospheres as SIB negative electrode material with an ether-based electrolyte. The obtained ZnS nanospheres display a high specific capacity of over 1000 mAh g<sup>-1</sup> at 20 mA g<sup>-1</sup> with a high coulombic efficiency of 90%. Moreover, the specific capacity of 774 mAh g<sup>-1</sup> can still be preserved for the 100th cycle. The first-principle calculations demonstrate that the ether-based electrolytes can effectively improve the electron transport and ion diffusion with

lower energy barrier, thus improving sodium storage property of electrodes. The fluoroethylene carbonate (FEC) as an efficient electrolyte additive has been used to form stable solid electrolyte interphase (SEI) films, improving the cycling performance of anode materials.<sup>[26]</sup> Wang et al.<sup>[26b]</sup> fabricated the exfoliated MoS<sub>2</sub>-C composites through chemical exfoliation and hydrothermal method. The exfoliated structure can offer short diffusion pathway for ion and accommodate large volume expansion. In addition, the optimized electrolyte with FEC additive is beneficial to form a thin and stable SEI layer. As a result, the composites deliver excellent sodium storage performance.

## 4. Synthesis Methods for Conversion-Type Anode Materials

### 4.1. Liquid Phase Method

#### 4.1.1. Hydrothermal and Solvothermal Methods

As an economical and environmentally friendly synthesis method, the hydrothermal and solvothermal methods have been widely used to synthesize a variety of nanomaterials with good crystallinity and narrow size distributions.<sup>[27]</sup> Moreover, these methods have also achieved great success in the preparation of conversion-type anode materials with controlled size, morphology, composition, and structure for application in SIBs.<sup>[28]</sup>

Ren et al.<sup>[28a]</sup> reported the preparation of ultrathin MoS<sub>2</sub> nanosheets@metal organic framework (MOF)-derived N-doped carbon nanowalls on flexible carbon cloth current collector (noted as CC@CN@MoS<sub>2</sub>) and applied them as anode materials for SIBs. In this synthesis (Figure 2a), cobalt-based MOF is used as a precursor to synthesize the porous N-doped carbon nanowall arrays via a solution route and a subsequent thermal treatment plus the acid etching process. Then, ultrathin MoS<sub>2</sub> nanosheets are successfully generated on the surface of N-doped carbon nanowall arrays via the hydrothermal method. The unique 2D hybrid structures enhance the reversible capacity and rate performance of MoS<sub>2</sub>. Geng et al.<sup>[28b]</sup> successfully fabricated metallic 1T MoS<sub>2</sub> grown on graphene scaffold. First, graphene was deposited onto nickel foam. The nickel was etched away using FeCl<sub>3</sub> to obtain hollow microtube scaffold. Then a solution consisting of MoO<sub>3</sub>, thioacetamide precursors, and graphene foam dispersed in ethanol was used to grow the MoS<sub>2</sub>-graphene-MoS<sub>2</sub> through the solvothermal process. The sandwich-structured 1T MoS<sub>2</sub>-graphene-1T MoS<sub>2</sub> morphologies are displayed in Figure 2b,c. From these images, it can be observed that the interior and exterior surfaces of the tube are covered by MoS<sub>2</sub>. Furthermore, Niu et al.<sup>[28c]</sup> reported the fabrication of MoSe<sub>2</sub> grown on N,P-co-doped carbon nanosheets (MoSe<sub>2</sub>/N,P-rGO) by a solvothermal reaction between Na<sub>2</sub>MoO<sub>4</sub> and Se dissolved in N<sub>2</sub>H<sub>4</sub>·H<sub>2</sub>O on the surface of graphene oxide (GO) and a subsequent calcination process. As displayed in Figure 2d, the as prepared MoSe<sub>2</sub> nanosheets loosely stack together to form a 3D network and leave a large number of voids within it, which would facilitate the infiltration of electrolyte and accommodate the volume change during cycling. Adopting a simple hydrothermal reaction, our group<sup>[29]</sup> successfully fabricated the FeSe<sub>2</sub> clusters consisting of nanorods. From the

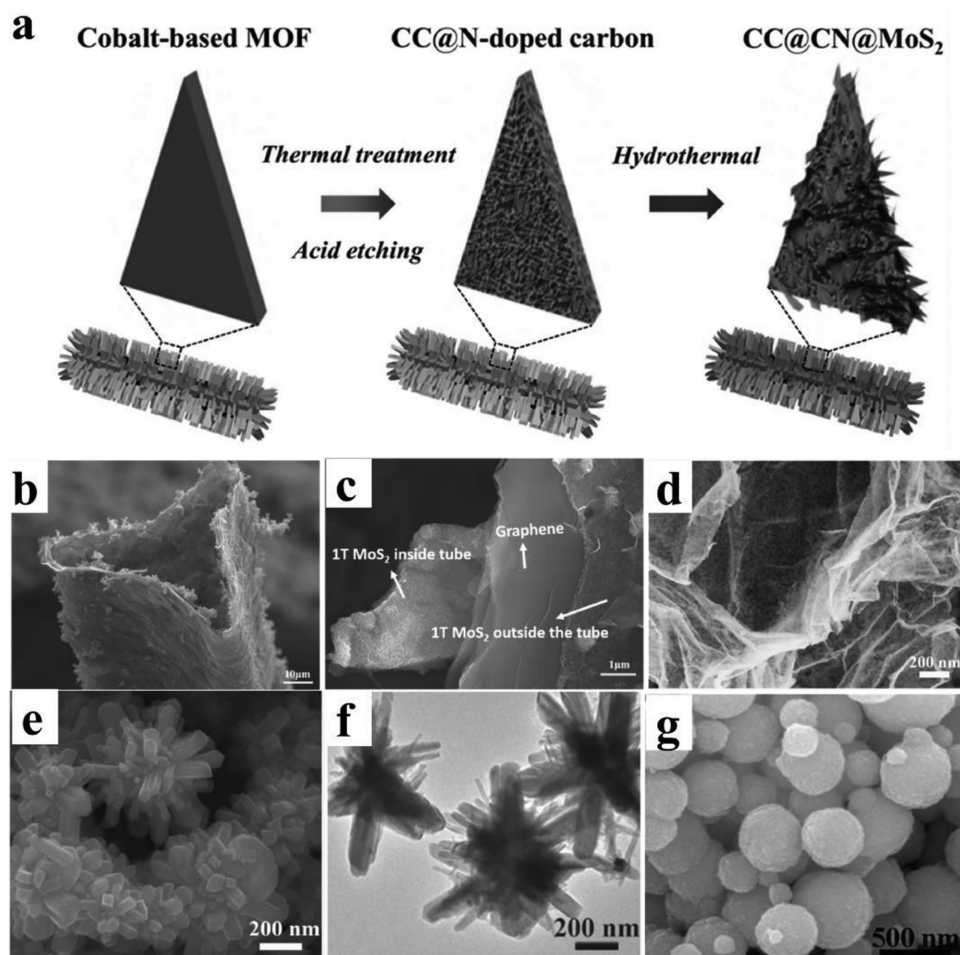


**Figure 2.** a) Schematic illustration of synthesis of the CC@CN@MoS<sub>2</sub> arrays. b,c) High-magnification image of a double side-coated graphene tube and cross-section of the edge of a graphene tube, respectively. d) SEM image of MoS<sub>2</sub>/N,P-rGO. e) SEM image of the FeSe<sub>2</sub> clusters. f) TEM image of the urchin-like CoSe<sub>2</sub>. g) SEM image of the as-prepared FeSe<sub>2</sub>, Fe<sub>0.5</sub> sample. a) Reproduced with permission.<sup>[28a]</sup> Copyright 2017, Wiley-VCH. b,c) Reproduced with permission.<sup>[28b]</sup> Copyright 2017, Wiley-VCH. d) Reproduced with permission.<sup>[28c]</sup> Copyright 2017, Wiley-VCH. e) Reproduced with permission.<sup>[29]</sup> Copyright 2017, Springer. f) Reproduced with permission.<sup>[30]</sup> Copyright 2016, Wiley-VCH. g) Reproduced with permission.<sup>[31]</sup> Copyright 2016, Wiley-VCH.

scanning electron microscope (SEM) image, it can be clearly observed that the FeSe<sub>2</sub> clusters were composed of nanorods (Figure 2e). The as-prepared FeSe<sub>2</sub> clusters exhibited superior sodium storage performance. Urchin-like CoSe<sub>2</sub> was prepared by Chen and co-workers through one-step solvothermal method and investigated as SIB negative electrode material.<sup>[30]</sup> As shown in Figure 2f, the as-prepared CoSe<sub>2</sub> displays uniform urchin-like morphology assembled by nanorods. The diameter of the nanorods is about 20–100 nm and the urchin is about 1 μm in size. Time-dependent experiment is also carried out to study its morphology formation mechanism. The initial precursor shows the morphology of nanospheres, and then these nanospheres gathered together to gradually transfer into the shape of nanorod. With the time prolonging, the percentage of nanorods increased. When the time increased to 24 h, the urchin-like structure assembled by nanorods was completely formed. A series of Co-doped FeS<sub>2</sub> with different Co contents were successfully synthesized via a feasible one-step solvothermal approach.<sup>[31]</sup> As displayed in Figure 2g, the as-prepared Co<sub>0.5</sub>Fe<sub>0.5</sub>S<sub>2</sub> (Fe<sub>0.5</sub>) spherical particles exhibit similar average

diameters of about 100 nm with a very uniform morphology. The energy-dispersive X-ray spectroscopy mapping images of the obtained Fe<sub>0.5</sub> sample have also been tested to investigate the distribution of elements. The results clearly indicate that S, Fe, and Co are distributed uniformly in the bulk. The formation of Co-doped FeS<sub>2</sub> is resulted from the ion exchange between the FeS<sub>2</sub> and Co<sup>2+</sup> ions. When employed as SIB negative electrode materials for the first time, the optimized Co<sub>0.5</sub>Fe<sub>0.5</sub>S<sub>2</sub> nanospheres deliver excellent electrochemical performance.

In addition, the single crystalline FeS<sub>2</sub> particles synthesized through a facile solvothermal approach were reported by Huang and co-workers.<sup>[32]</sup> The capacity fading reasons of microsized FeS<sub>2</sub> particles were studied, which caused by structure collapse and exfoliation of electrodes. The electrochemical performance of microsized FeS<sub>2</sub> is improved by controlling voltage range, adopting appreciate binder and coating graphene. Zhao et al.<sup>[33]</sup> synthesized the lychee-like FeS<sub>2</sub>@FeS<sub>2</sub> core-shell microspheres by a simple hydrothermal method and further studied their sodium storage properties. The SEM and TEM images show that the obtained FeS<sub>2</sub>@FeS<sub>2</sub> samples have the diameters of about

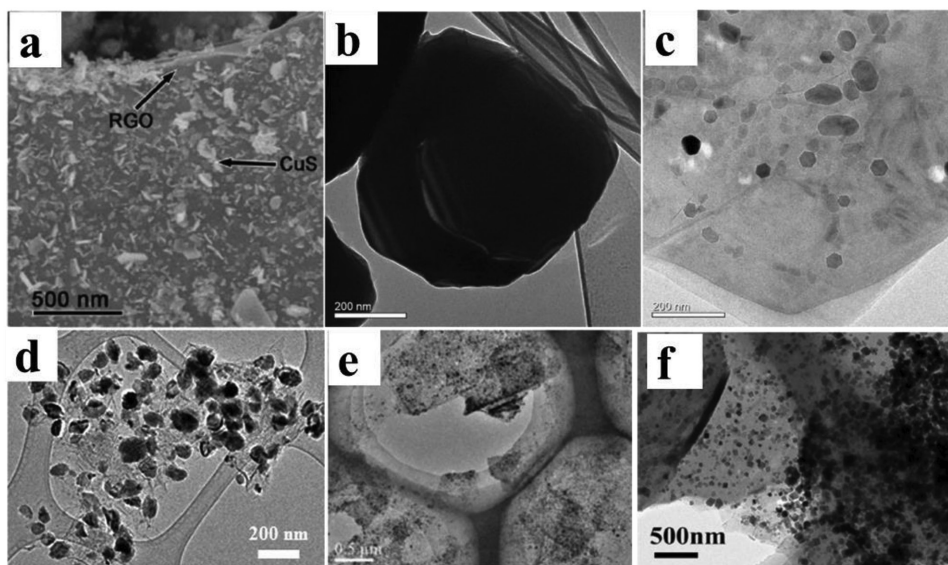


**Figure 3.** a) SEM image of CuS–RGO-2 sample. b,c) TEM images of pure NiS and NiS–RGO-2, respectively. d) TEM image of  $\alpha$ -Fe<sub>2</sub>O<sub>3</sub>/rGO2 nanocomposite. e) TEM image of Fe<sub>2</sub>O<sub>3</sub>–RGO composite. f) TEM image of MFO/RGO-2. a) Reproduced with permission.<sup>[37]</sup> Copyright 2017, American Chemical Society. b,c) Reproduced with permission.<sup>[38]</sup> Copyright 2015, Elsevier. d) Reproduced with permission.<sup>[40]</sup> Copyright 2015, Elsevier. e) Reproduced with permission.<sup>[41]</sup> Copyright 2015, Elsevier. f) Reproduced with permission.<sup>[43]</sup> Copyright 2015, Elsevier.

2–3  $\mu\text{m}$ . The surface of FeS<sub>2</sub> core is uniformly encapsulated by porous FeSe<sub>2</sub> nanoparticles. As anode material for SIBs, lychee-like FeS<sub>2</sub>@FeSe<sub>2</sub> electrodes deliver excellent rate performance and long-life cycling property, which is benefited from the unique core–shell microsphere structure. Li et al.<sup>[34]</sup> fabricated greigite Fe<sub>3</sub>S<sub>4</sub> particles through a simple hydrothermal approach. The SEM image shows that the particles possess the octahedral structure with the size of 100–200 nm. When applied as negative electrode material for SIBs, the obtained Fe<sub>3</sub>S<sub>4</sub> delivers superior sodium storage performance based on conversion reaction.

#### 4.1.2. Microwave Method

Microwave chemistry has been widely used in liquid phase fabrication of the inorganic nanomaterials because of its high reaction rate, short reaction times, improved yields with less side products, low cost, and environment friendliness.<sup>[35]</sup> When applied in the preparation of conversion-type anode materials, the microwave method also shows a great advantage.<sup>[36]</sup> For example, Li et al.<sup>[37]</sup> prepared CuS–reduced graphene oxide (RGO) composites through microwave-assisted method and successfully applied them to SIBs. As shown in **Figure 3a**, the CuS nanosheets are evenly distributed on the surface of RGO nanosheets, which is favorable for improving the connection between CuS and electrolyte and eventually enhances the sodium-ion storage performance. At the same time, it is also found that the sample synthesized using 200 mg GO in microwave-assisted process (donated as CuS–RGO-2) exhibits the best electrochemical property. In addition, Qin et al.<sup>[38]</sup> prepared layered NiS–RGO composites via a simple microwave-assisted process and subsequent calcination process. As displayed in **Figure 3b**, the NiS shows typical bulk structure with a size of about 400–500 nm before the addition of RGO. However,

when RGO was added to the composites, the bulk NiS is converted to nanoparticles with a size of about 20–50 nm and uniformly distributed on the surface of RGO matrix (**Figure 3c**), which is beneficial for enhancing the sodium storage property. Compared with the pure NiS sample, the NiS–RGO composites exhibit distinctly improved electrochemical performance. The MoS<sub>2</sub>–RGO composites were also synthesized through the same microwave-assisted method by Qin et al.<sup>[39]</sup> From the SEM and TEM images, it can be noticed that the MoS<sub>2</sub> and RGO are interconnected, forming 3D hierarchical nanostructures. The packed RGO can buffer the large volume expansion of electrodes and raise the electrical conductivity of the composites, enhancing the electrochemical performance of MoS<sub>2</sub>. The  $\alpha$ -Fe<sub>2</sub>O<sub>3</sub>/rGO nanocomposites were successfully prepared through a facile microwave hydrothermal method within 15 min by Wang and co-workers.<sup>[40]</sup> In this synthesis, the microwave method saves a lot of time and offers a great deal of potential for large-scale reactions. The morphology and microstructure of  $\alpha$ -Fe<sub>2</sub>O<sub>3</sub>/rGO nanocomposites were investigated by SEM and TEM. The TEM image shows that nanosized  $\alpha$ -Fe<sub>2</sub>O<sub>3</sub> particles are evenly dispersed on the rGO nanosheets (**Figure 3d**). There are a large number of nanovoids existing in  $\alpha$ -Fe<sub>2</sub>O<sub>3</sub> nanoparticles, mainly due to the high energy microwave process. The nanovoids are favorable for accommodating the large volume changes during the electrochemical reaction. Besides, Liu et al.<sup>[41]</sup> also synthesized Fe<sub>2</sub>O<sub>3</sub>–RGO composites through a microwave-assisted approach, as shown in **Figure 3e**. The RGO sheets can act as a conductive network in the composites, which enhances the electronic transport of electrodes. The obtained Fe<sub>2</sub>O<sub>3</sub>–RGO composites are investigated as SIB anode, delivering the improved reversible capacity and cycling stability. The microwave irradiation offers a simple and scalable approach to synthesize the graphene-based materials for energy storage systems.<sup>[42]</sup> Zhang et al.<sup>[43]</sup> fabricated MgFe<sub>2</sub>O<sub>4</sub>/RGO

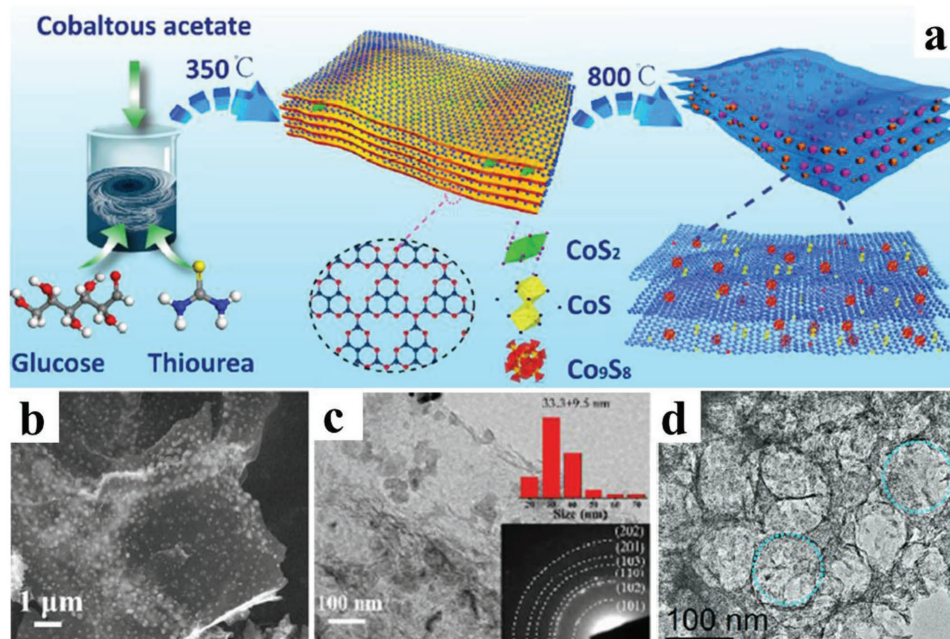


**Figure 4.** a) Schematic diagram for the synthesis of the  $\text{CoS}_x\text{@NSC-}\gamma$  nanocomposite. b) SEM image of  $\text{Co}_{1-x}\text{S/FGNs}$  composites. c) TEM image of  $\text{Co}_{1-x}\text{S/FGNs}$  composites, and insets are the particle size distribution and SAED pattern. d) TEM images of  $\text{MoS}_2\text{@NHPC}$ . a) Reproduced with permission.<sup>[45]</sup> Copyright 2017, American Chemical Society. b,c) Reproduced with permission.<sup>[46]</sup> Copyright 2017, Royal Society of Chemistry. d) Reproduced with permission.<sup>[47b]</sup> Copyright 2016, Elsevier.

composites by a simple microwave-assisted method and evaluated their sodium storage property. The obtained  $\text{MgFe}_2\text{O}_4$  particles are uniformly dispersed on the surface of RGO and possess the size of about 30–50 nm, as displayed in Figure 3f. Benefiting from the synergistic effect of  $\text{MgFe}_2\text{O}_4$  and RGO, the as-prepared  $\text{MgFe}_2\text{O}_4/\text{RGO}$  composites exhibit superior electrochemical performance.

#### 4.1.3. Sol–Gel Method

Sol–gel method is an efficient approach for synthesizing nanomaterials. First, a suspension comprised of colloidal particles (sol) is formed, and then the sol is turned into a gel after the aggregation process of colloidal particles. Second, the gel is heat treated to produce the expected material. Generally, the chemical reaction involved in this method is based on inorganic polymerization.<sup>[44]</sup>

Guo et al.<sup>[45]</sup> synthesized hierarchically 2D  $\text{CoS}_x$  ( $\text{CoS}$  and  $\text{Co}_9\text{S}_8$ ) quantum dots embedded N/S-doped carbon (NSC) sheet samples through a sol–gel process. The synthesis procedure of  $\text{CoS}_x\text{@NSC}$  composites is schematically illustrated in Figure 4a. Cobalt acetate, thiourea, and glucose are first mixed to obtain a gel precursor and then this gel precursor is heated at 350 °C, while the sacrificial template of graphitic carbon nitride ( $\text{C}_3\text{N}_4$ ) nanosheets is generated from the decomposition of thiourea. With further calcination at 800 °C, the intermediate product is converted into the desired product. The TEM image reveals that the as-prepared  $\text{CoS}_x\text{@NSC-1}$  is 2D transparent nanosheet morphology. The  $\text{CoS}_x$  nanoparticles are embedded in the NSC nanosheets with the average size of 3–5 nm. The

$\text{CoS}_x\text{@NSC}$  composites deliver the superior rate property and excellent cycle life, which can be attributed to the ultrafine  $\text{CoS}_x$  particle size and enriched N and S codoped carbon nanosheets (CNSs). Chen et al.<sup>[46]</sup> prepared  $\text{Co}_{1-x}\text{S/functional}$  graphene nanosheets (FGNs) through a simple sol–gel approach and two-step thermal treatments. In this synthesis, urea is used as a soft template and nitrogen source while citric acid acts as a carbon source. The  $\text{Co}^{2+}$  is uniformly distributed in organic precursors at the sol–gel stage. Then urea can be decomposed and transformed into a self-sacrifice template ( $\text{g-C}_3\text{N}_4$ ) for the growth of 2D nitrogen-doped graphene frameworks and  $\text{Co}^{2+}$  ions are transformed into Co nanoparticles at the first-step of heat treatment. From the SEM image, it can be clearly observed that the in situ grown Co nanoparticles are uniformly distributed and embedded in FGNs. At last, the Co nanoparticles are converted into  $\text{Co}_{1-x}\text{S}$  nanoparticles on the 2D FGNs under the reaction with sulfur powder to obtain the final  $\text{Co}_{1-x}\text{S/FGNs}$  composites with the similar structure of  $\text{Co/FGNs}$ , as shown in Figure 4b. The particle size distribution analysis shows that the size of  $\text{Co}_{1-x}\text{S}$  nanoparticles is about 25–45 nm (Figure 4c). The selected-area electron diffraction pattern (inset in Figure 3c) shows multiple diffraction rings, confirming the existence of  $\text{Co}_{1-x}\text{S}$ . The  $\text{Co}_{1-x}\text{S}$  nanoparticles shorten the electron/ion transport pathway and ultrathin FGNs enhance the electrical conductivity of electrodes. As a result,  $\text{Co}_{1-x}\text{S/FGNs}$  as SIB anodes exhibit high initial coulombic efficiency and reversible specific capacity, excellent rate property, and superior cycling performance. Several other conversion-type anode materials are also obtained using a facile sol–gel process.<sup>[47]</sup> The ultrasmall  $\text{MoS}_2$  nanosheets embedded in N-doped hierarchical porous carbon matrix ( $\text{MoS}_2\text{@NHPC}$ ) were reported by Tang et al. and

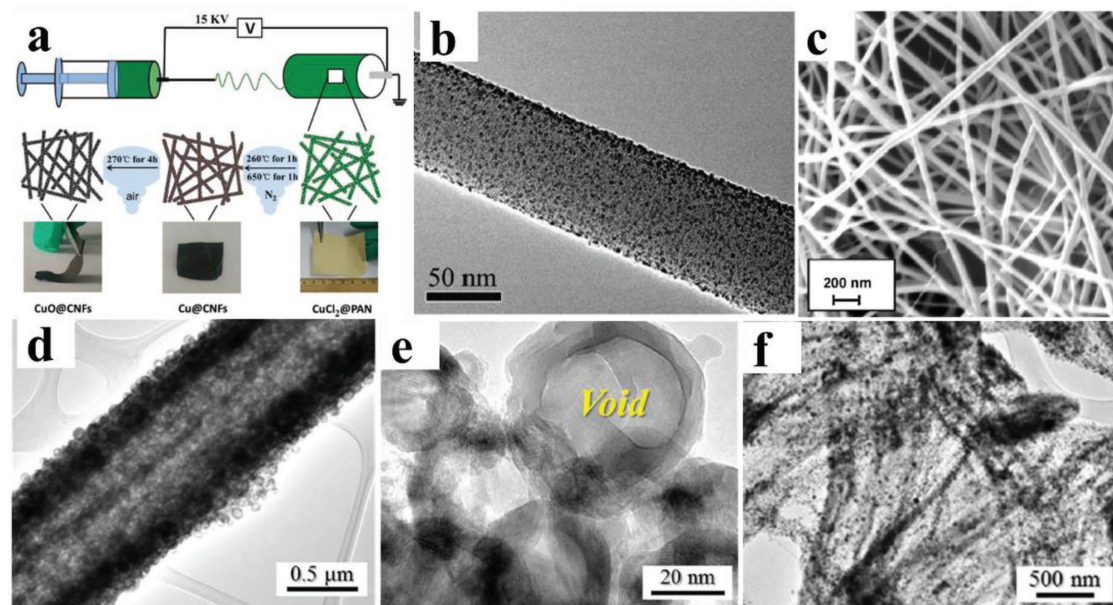


**Figure 5.** a) Schematic illustration of the formation process for CuO@C nanofibers. b) TEM image of 2-CuO@C. c) SEM image of the MoS<sub>2</sub>-carbon nanofiber composites. d,e) TEM image of hollow nanosphere FeSe<sub>2</sub>@GC-rGO composite nanofiber. f) TEM image of NiSe<sub>2</sub>-rGO-C. a,b) Reproduced with permission.<sup>[49]</sup> Copyright 2016, Wiley-VCH. c) Reproduced with permission.<sup>[50]</sup> Copyright 2014, Wiley-VCH. d,e) Reproduced with permission.<sup>[52]</sup> Copyright 2016, Nature Publishing Group. f) Reproduced with permission.<sup>[53]</sup> Copyright 2016, Nature Publishing Group.

evaluated as negative electrode material for SIBs.<sup>[47b]</sup> Acetic acid-induced chitosan viscolloid and ammonium tetrathiomolybdate (ATMD) are used as carbon source and the precursor of MoS<sub>2</sub>, respectively. During the synthesis process, the electrostatic adsorption between the MoS<sub>4</sub><sup>2-</sup> produced by ATMD solution and NH<sub>3</sub><sup>+</sup> on the chitosan is facilitated to form uniform encapsulation of MoS<sub>2</sub> into the carbon matrix. Additionally, polystyrene nanosphere is utilized as an efficient template to form hierarchical pores. The morphological feature of MoS<sub>2</sub>@NHPC was investigated by TEM. The TEM image shows that the MoS<sub>2</sub>@NHPC samples possess well-constructed hierarchical porous structure (Figure 4d). The unique architecture is favorable for the improvement of electrochemical performance.

## 4.2. Electrospinning Method

Electrospinning as an attractive approach has been adopted to synthesize 1D materials due to its simple set-up, controllable size, and versatility. This scalable method has also been successfully applied to synthesize a number of conversion-type anode materials that incorporated into the nanofibers for SIBs. It is worth mentioning that the electrospun electrode materials have attracted wide attention for energy storage system, due to their high specific surface areas, short ion diffusion path, good mechanical property, and enhanced ionic conductivities.<sup>[48]</sup>

Wang et al.<sup>[49]</sup> synthesized the CuO quantum dots encapsulated in carbon nanofibers (CuO@C) through a facile electrospinning and subsequent heat treatment process. The preparation process of CuO@C nanofibers is schematically illustrated in Figure 5a. In this synthesis, Cu<sup>2+</sup> promotes the formation of carbon and carbon matrix confines the growth of CuO particles. Finally, the uniform CuO quantum dots encapsulated

in the carbon frame were prepared. The reaction conditions and the precursor solution composition have a big influence on the structure of hybrids and the size of CuO grains. The as-prepared 2-CuO@C displays the average diameter of 80 nm and the length up to hundreds of micrometers (Figure 5b). The unique 3D network structure provides various advantages, such as short transport length and good mechanical strength. Zhu et al.<sup>[50]</sup> fabricated single-layered MoS<sub>2</sub> nanoplates embedded in carbon nanofibers via a feasible electrospinning method. As displayed in Figure 5c, the as-prepared MoS<sub>2</sub>-carbon nanofibers have a diameter of about 50 nm and show uniform, thin, interconnection with each other, forming a 3D network, which offers the efficient transport pathway for ion/electron. As a result, the as-prepared MoS<sub>2</sub>-carbon nanofiber electrodes show a high reversible capacity and outstanding cycling property. Xiong et al.<sup>[51]</sup> also synthesized MoS<sub>2</sub>/carbon nanofibers (MoS<sub>2</sub>-CNFs) via a facile electrospinning process. The fabricated MoS<sub>2</sub>-CNFs are composed of interconnected nanofibers with a size of ≈150 nm in diameters. Meanwhile, the MoS<sub>2</sub>-CNFs films show superior membrane flexibility. When tested as the binder-free SIB negative electrode materials, the MoS<sub>2</sub>-CNFs deliver a high reversible specific capacity, superior rate performance, and outstanding cycling capability. In addition, Cho et al.<sup>[52]</sup> successfully synthesized hollow nanosphere FeSe<sub>2</sub>@GC-rGO composite nanofibers through the electrospinning method and evaluated their sodium storage performance. The morphological features of FeSe<sub>2</sub>@GC-rGO hybrids are investigated by TEM. As shown in Figure 5d,e, the TEM images reveal that the hybrid nanofibers are composed of hollow nanospheres formed by the process of the nanoscale Kirkendall diffusion, mainly due to the diffusion of Fe cations outward faster than that of Se anion inward. Benefiting from the advantages of the FeSe<sub>2</sub> hollow structure and conductive rGO matrix, the FeSe<sub>2</sub>@GC-rGO hybrid

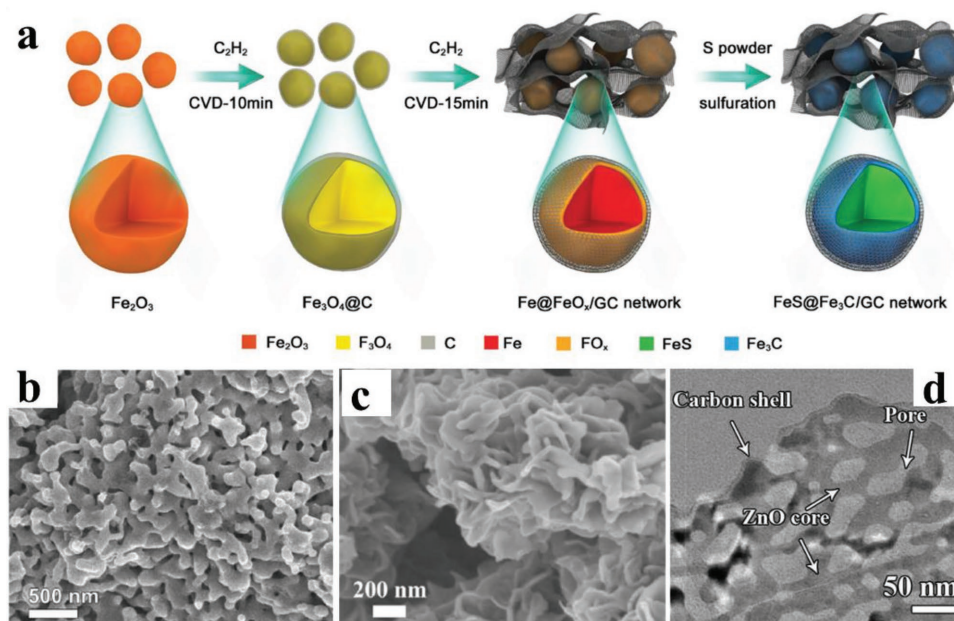


**Figure 6.** a) Schematic illustration of the synthesis of 3D interconnected FeS@Fe<sub>3</sub>C@GC networks. b) SEM image of FeS/C-15. c) SEM image of the MoS<sub>2</sub>@C-700. d) TEM image of C-ZnO nanosheets. a,b) Reproduced with permission.<sup>[54]</sup> Copyright 2017, Wiley-VCH. c) Reproduced with permission.<sup>[55]</sup> Copyright 2017, Elsevier. d) Reproduced with permission.<sup>[56]</sup> Copyright 2018, Elsevier.

nanofibers display improved electrochemical properties compared with bare FeSe<sub>2</sub> nanofibers. Using the similar electrospinning and subsequent selenization process, Kang and co-workers prepared NiSe<sub>2</sub>-rGO-C composite nanofibers and studied their Na-ion storage properties.<sup>[53]</sup> The as-prepared NiSe<sub>2</sub>-rGO-C hybrids have a wood pulp fiber-like porous morphology and the ultrafine NiSe<sub>2</sub> nanocrystals are evenly dispersed on the surface of hybrid nanofibers, as shown in Figure 5f. The unique porous-structured hybride nanofibers have good structural stability and exhibit the enhanced sodium-ion storage performance.

#### 4.3. Chemical Vapor Deposition Method

The chemical vapor deposition (CVD) method is one of the most extensively adopted routes to synthesize nanomaterials for energy storage fields.<sup>[12c]</sup> It offers a low-energy and facile process in the synthesis of conversion-type negative electrode materials. For instance, Wang et al.<sup>[54]</sup> reported in situ synthesis of 3D FeS@Fe<sub>3</sub>C@GC composite via a feasible CVD approach followed by the sulfuration strategy. The fabrication process of 3D FeS@Fe<sub>3</sub>C@GC networks is schematically illustrated in Figure 6a. First, Fe<sub>2</sub>O<sub>3</sub> nanoparticles are synthesized via a hydrothermal and subsequent annealing process. And then, using the time-saving catalytic CVD method, the individual Fe<sub>2</sub>O<sub>3</sub> nanoparticles are connected by graphitic carbon to form the porous 3D integrated Fe@FeO<sub>x</sub>/GC composites under C<sub>2</sub>H<sub>2</sub> gas for 15 min. In the end, the Fe@FeO<sub>x</sub>/GC composite is transformed into FeS@Fe<sub>3</sub>C@GC composites with the well-defined network under the sulfuration process. The formation of the unique structure can be ascribed to the catalytic effect of iron-group metals and metal oxides during the CVD process. The SEM image reveals that the as-prepared FeS/C-15

composites possess the porous 3D interconnected structure, as displayed in Figure 6b. The unique structures shorten the diffusion pathways of electron/ion and enhance the structural stability of FeS@Fe<sub>3</sub>C@GC composites, endowing the electrode materials with excellent rate property and superior cycle life. Li et al.<sup>[55]</sup> prepared MoS<sub>2</sub> nanosheets coated with semi-graphitized carbon through a simple CVD approach. From the SEM image, it can be seen that the as-prepared MoS<sub>2</sub>@C-700 shows a hierarchical flower-like structure assembled by nanosheets with several nanometers, as represented in Figure 6c. The thicknesses of the nanosheets are significantly increased after the carbon layer coating by CVD compared with the bare MoS<sub>2</sub> nanosheets. The results demonstrate that the feasible CVD strategy has the merits of good shape retention as well as thickness controllability. Owing to the improved electron transport and structural stability, the MoS<sub>2</sub>@C electrodes show long-life cycling performance. Adopting a scalable hydrothermal method and a subsequent CVD process, Teng et al.<sup>[56]</sup> successfully synthesized the carbon-coated ZnO 2D porous nanosheets. The morphology of C-ZnO composites is characterized by TEM. It can be observed that the sizes of the uniformly distributed pores are less than 40 nm and the thickness of the carbon-coating layer is about 5 nm, as depicted in Figure 6d. The unique C-ZnO porous structure can offer sufficient space to accommodate large volume expansion during sodiation/desodiation process and provide a better conductivity and a shorter ion diffusion distance, leading to improved electrochemical performance.

#### 4.4. Other Methods

In addition to the above methods, many other effective approaches are also proposed to synthesize conversion-type

anode materials with different morphologies and structures. For example, Liu et al.<sup>[57]</sup> synthesized a unique FeS<sub>2</sub>@C yolk-shell nanostructure via a simple etching method combined with a sulfidation-in-nanobox process. The hydrochloric acid is applied to partially remove Fe<sub>3</sub>O<sub>4</sub> core to form a yolk-shell structure and then the yolk-shell FeS<sub>2</sub>@C nanoboxes (FeS<sub>2</sub>@C-45) are obtained via the subsequent sulfidation at high temperature. The average sizes of FeS<sub>2</sub> cores in FeS<sub>2</sub>@C-0 (unetched sample) and FeS<sub>2</sub>@C-45 are about 630 and 320 nm, respectively. Compared with FeS<sub>2</sub>@C-0, FeS<sub>2</sub>@C-45 has a larger void space between FeS<sub>2</sub> core and the carbon shell, which is favorable for accommodating the large volume change of FeS<sub>2</sub> during cycling process. When tested as SIB anode, the FeS<sub>2</sub>@C-45 electrodes show high reversible specific capacity, high rate performance, and long-term cycling property. Liquid phase exfoliation (LPE) is a scalable and effective method for fabricating layer nanosheets from a variety of layered materials. Liu et al.<sup>[58]</sup> synthesized high-quality MoS<sub>2</sub> nanosheet dispersion by LPE method and then constructed MoS<sub>2</sub>/single-wall nanotubes (SWNTs) hybrids. The SEM and TEM images demonstrate that the as-prepared MoS<sub>2</sub> nanosheets are evenly distributed in the SWNT network. When investigated as negative electrode materials for SIBs, the MoS<sub>2</sub>/SWNT composites show high specific capacity and outstanding cycling property because of their big porosity and excellent mechanical strength. Furthermore, Kim and Kang<sup>[59]</sup> prepared (Fe<sub>0.5</sub>Ni<sub>0.5</sub>)<sub>9</sub>S<sub>8</sub> yolk-shell powders through the spray pyrolysis followed by the sulfidation process and applied them as negative electrode materials for SIBs. The morphology and structure features of (Fe<sub>0.5</sub>Ni<sub>0.5</sub>)<sub>9</sub>S<sub>8</sub> samples are confirmed by SEM and TEM. The SEM and TEM images display that the (Fe<sub>0.5</sub>Ni<sub>0.5</sub>)<sub>9</sub>S<sub>8</sub> samples possess yolk-shell structure and the shell part is composed of ultrafine nanocrystals with the size of <50 nm. The obtained (Fe<sub>0.5</sub>Ni<sub>0.5</sub>)<sub>9</sub>S<sub>8</sub> samples exhibit large initial discharge and charge capacities at 0.1 A g<sup>-1</sup>. The excellent sodium storage property can be ascribed to the unique yolk-shell structure and multicomponent sulfide composition.

## 5. Conversion-Type Anode Materials for Sodium-Ion Batteries

### 5.1. Metal Oxides

#### 5.1.1. Iron-Based Oxides

Iron-based oxides are considered as attractive SIB anode materials because of their nontoxicity, low cost, abundance, and large specific capacity. Nevertheless, Fe-based oxides suffer from the large volume change and low electronic conductivity. To solve the abovementioned problems, great efforts have been devoted to designing nanostructured material with various morphologies and constructing carbon composites.<sup>[60]</sup> For instance, Zhang et al.<sup>[60a]</sup> reported 3D porous  $\gamma$ -Fe<sub>2</sub>O<sub>3</sub>@C nanocomposite as SIB negative electrode material. The Fe<sub>2</sub>O<sub>3</sub> nanoparticles are uniformly embedded in carbon matrix, possessing an average size of 5 nm. The obtained  $\gamma$ -Fe<sub>2</sub>O<sub>3</sub>@C nanocomposite has an average size of 400 nm, exhibiting the 3D porous spherical structure. Owing to the synergistic effect of porous carbon matrix and  $\gamma$ -Fe<sub>2</sub>O<sub>3</sub> nanoparticles, the  $\gamma$ -Fe<sub>2</sub>O<sub>3</sub>@C

nanocomposite delivers long-life cyclability and excellent rate capability. Xia et al.<sup>[60b]</sup> designed a novel peapod-like nanostructured composite, which consists of Fe<sub>2</sub>O<sub>3</sub> nanoparticles and N-doped porous carbon nanofibers (Fe<sub>2</sub>O<sub>3</sub>@N-PCNFs). **Figure 7a–c** shows the TEM images and elemental mapping of Fe<sub>2</sub>O<sub>3</sub>@N-PCNFs. It can be observed that macropores and micropores exist in the as-prepared sample and the thickness of N-doped carbon shell is about 20 nm. The elements of Fe, O, C, and N are evenly dispersed in the as-prepared products. When employed as negative electrode material for SIBs, the obtained Fe<sub>2</sub>O<sub>3</sub>@N-PCNFs deliver a discharge capacity of 806 mAh g<sup>-1</sup> at 200 mA g<sup>-1</sup> for the 100th cycle. Even at a high current density of 2 A g<sup>-1</sup>, the composite still offers a specific capacity of 396 mAh g<sup>-1</sup> after 1500 cycles. The superior sodium storage performance is ascribed to the excellent stress relaxation, enhanced ions, and electrons transportation resulted from the unique structure. Li et al.<sup>[60c]</sup> synthesized amorphous Fe<sub>2</sub>O<sub>3</sub>/graphene nanosheets composite (Fe<sub>2</sub>O<sub>3</sub>@GNS) via a facile method, as illustrated in **Figure 7d**. When applied as SIB anode, the amorphous Fe<sub>2</sub>O<sub>3</sub>@GNS exhibits better rate property than that of the crystalline Fe<sub>2</sub>O<sub>3</sub>@GNS-500 (**Figure 7e**). The amorphous Fe<sub>2</sub>O<sub>3</sub>@GNS composites still achieve a specific capacity of 110 mAh g<sup>-1</sup> at 2 A g<sup>-1</sup> for the 500th cycle, as displayed in **Figure 7f**. The excellent property of Fe<sub>2</sub>O<sub>3</sub>@GNS can be ascribed to amorphous structures and the strong interfacial interaction.

The spinel ferrites exhibit superior electrochemical property resulting from the synergetic effect of binary metals, regarded as a promising SIB anode. Liu et al.<sup>[61]</sup> fabricated the MnFe<sub>2</sub>O<sub>4</sub>@C nanofibers (MFO@C) via a facile electrospinning technique. **Figure 8a,b** presents the TEM and high-resolution transmission electron microscopy (HRTEM) images of MFO@C, demonstrating that MnFe<sub>2</sub>O<sub>4</sub> nanoparticles are homogeneously encapsulated in porous N-doped carbon matrix. It is worthy to note that the MnFe<sub>2</sub>O<sub>4</sub> nanoparticles are ultrafine with an average size of 3.3 nm (**Figure 8c**). The d-spacings of 0.30 and 0.21 nm are shown in **Figure 8d**, corresponding to the (220) and (400) planes of MnFe<sub>2</sub>O<sub>4</sub>. The ultrasmall MnFe<sub>2</sub>O<sub>4</sub> nanoparticle structure shortens sodium ion diffusion time and the N-doped carbon nanofibers enhance the electric conductivity. Thus, the as-prepared MFO@C exhibits high-rate capability and cycling performance (**Figure 8e,f**). Wen and co-workers<sup>[62]</sup> prepared interconnected CoFe<sub>2</sub>O<sub>4</sub>-polypyrrole (PPy) nanotubes (CFO-PPy-NTs) through an in situ hydrothermal method (**Figure 8g**). Benefiting from the synergetic effect of CoFe<sub>2</sub>O<sub>4</sub> particles and interconnected PPy nanotube, the composites display superior electrochemical performance. A stable specific capacity of 220 mAh g<sup>-1</sup> can be achieved for the 2000th cycle at 1000 mA g<sup>-1</sup>, as shown in **Figure 8h**.

#### 5.1.2. Cobalt-Based Oxides

Cobalt oxides are also considered as promising negative electrode materials because of their low cost and high capacity based on typical conversion reaction. However, their inferior electronic conductivity and large volume expansion during sodium ion insertion/extraction processes result in poor rate performance and irreversible capacity loss. To solve these issues, various approaches have been used to improve sodium storage

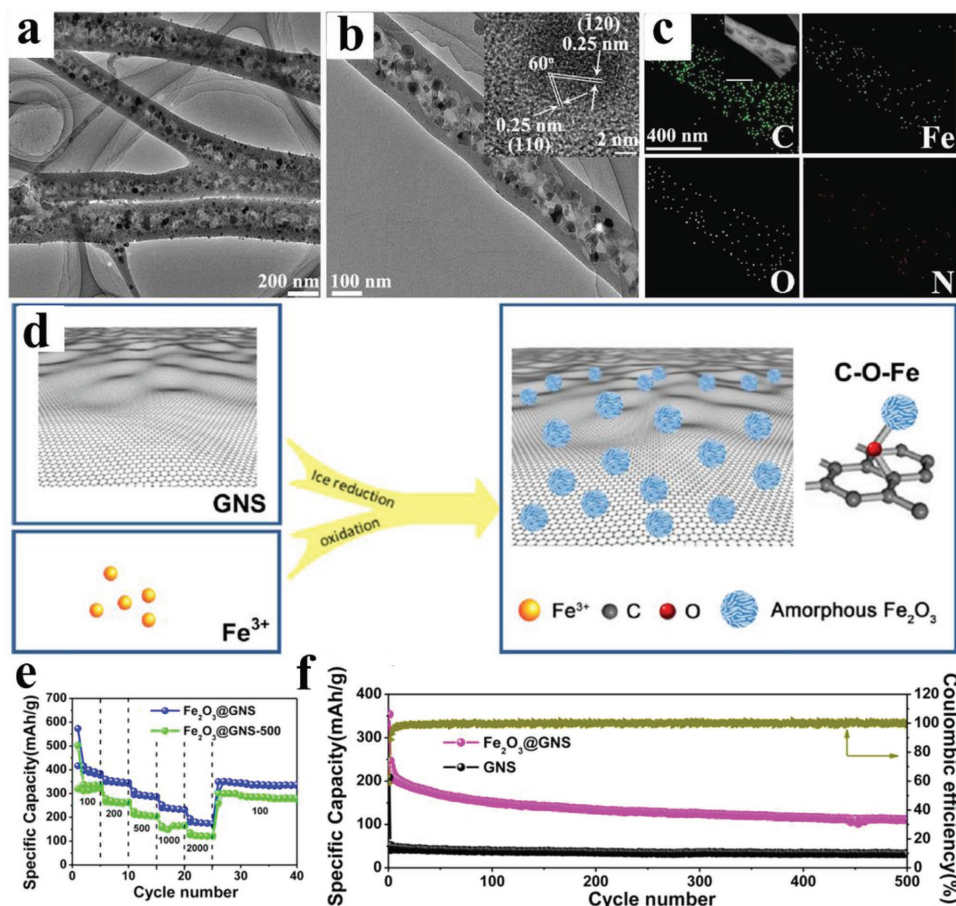


**Figure 7.** a,b) TEM images of Fe<sub>2</sub>O<sub>3</sub>@N-PCNFs. The inset of panel (b) shows an HRTEM image of Fe<sub>2</sub>O<sub>3</sub>@N-PCNFs. c) Elemental mapping of Fe<sub>2</sub>O<sub>3</sub>@N-PCNFs. d) Schematic illustration of the synthesis of Fe<sub>2</sub>O<sub>3</sub> and GNS composites. e) Rate capability of Fe<sub>2</sub>O<sub>3</sub>@GNS and Fe<sub>2</sub>O<sub>3</sub>@GNS-500. f) Cycling performance for Fe<sub>2</sub>O<sub>3</sub>@GNS and pure grahene nanosheets cycled at a current of 2 A g<sup>-1</sup>, and Coulombic efficiency of the Fe<sub>2</sub>O<sub>3</sub>@GNS sample. a–c) Reproduced with permission.<sup>[60b]</sup> Copyright 2017, Wiley-VCH. d–f) Reproduced with permission.<sup>[60e]</sup> Copyright 2016, American Chemical Society.

performance of cobalt oxides.<sup>[63]</sup> For example, Wu et al.<sup>[63a]</sup> adopted a facile interface-modulated approach to synthesize hierarchical yolk–shell Co<sub>3</sub>O<sub>4</sub>/C dodecahedrons. **Figure 9a** displays the schematic illustration of the synthesis of Co<sub>3</sub>O<sub>4</sub>/C by controlling the heat-treatment process. The unique yolk–shell structure (Figure 9b) provides enough space for volume expansion and carbon matrix improves the conductivity of Co<sub>3</sub>O<sub>4</sub>/C dodecahedrons. As an SIB anode material, the as-prepared yolk–shell Co<sub>3</sub>O<sub>4</sub>/C dodecahedrons exhibit high rate capability (Figure 9c). Recently, Chen et al.<sup>[63b]</sup> synthesized 2D holey Co<sub>3</sub>O<sub>4</sub> nanosheets by a template-directed strategy. It is demonstrated that the tunable holey sizes can efficiently enhance sodium-ion storage performance. The holey assembly of Co<sub>3</sub>O<sub>4</sub> nanoparticles (ACN) prepared with 0.3, 0.5, and 5 mmol Co precursors have the pore sizes of 5, 10, and 20 nm (donated as HACN-5, HACN-10, HACN-20), respectively, as shown in Figure 9d–f. The results show that the HACN-10 electrode exhibits highest sodium ion storage capacity and superior cycling property (Figure 9g). Yang et al.<sup>[64]</sup> prepared the mesoporous Co<sub>3</sub>O<sub>4</sub> (m-Co<sub>3</sub>O<sub>4</sub>) microspheres via nanocasting route by adopting KIT-6 silica as a template. The obtained m-Co<sub>3</sub>O<sub>4</sub> samples display well-ordered and interconnected network structure. When used as SIB anode, the m-Co<sub>3</sub>O<sub>4</sub> shows a high initial capacity of 782 and 707 mAh g<sup>-1</sup> at 30 and

90 mA g<sup>-1</sup>, respectively. At high rates of 810 and 2430 mA g<sup>-1</sup>, the specific capacities of 357 and 267 mAh g<sup>-1</sup> are achieved, respectively. The shale-like Co<sub>3</sub>O<sub>4</sub> assembled by nanocrystallites was synthesized by Li et al. and employed as negative electrode material for SIBs.<sup>[65]</sup> The SEM and TEM images exhibit that the as-prepared Co<sub>3</sub>O<sub>4</sub> samples have hierarchical layer-by-layer structure and a single Co<sub>3</sub>O<sub>4</sub> layer has obvious wrinkled surface, which is favorable for the permeability of the electrolyte. The reversible capacities of 380 and 153.8 mAh g<sup>-1</sup> are obtained at rates of 50 and 5000 mA g<sup>-1</sup>, respectively. To further improve the cycling stability and rate property of Co<sub>3</sub>O<sub>4</sub> electrode materials, Kang et al.<sup>[66]</sup> prepared Co<sub>3</sub>O<sub>4</sub>/N–C polyhedrons by annealing the Co-TATB MOF. The Co<sub>3</sub>O<sub>4</sub>/N–C polyhedrons show the hollow structure and the rough surface consisting of nanoparticles. For sodium storage, the Co<sub>3</sub>O<sub>4</sub>/N–C electrode exhibits a high reversible capacity of 468 mAh g<sup>-1</sup> at 0.1 A g<sup>-1</sup> and a stable capacity of 229 mAh g<sup>-1</sup> for the 150th cycle at 1 A g<sup>-1</sup>.

Bimetallic oxides have been recognized as promising host material for SIBs because of their high electrochemical activities.<sup>[67]</sup> Jiao and co-workers fabricated the N-doped CuCo<sub>2</sub>O<sub>4</sub>@C film through a simple electrospinning technique and used it as SIB anode.<sup>[67c]</sup> The TEM images show that the CuCo<sub>2</sub>O<sub>4</sub> grains have an average size of about 3 nm and

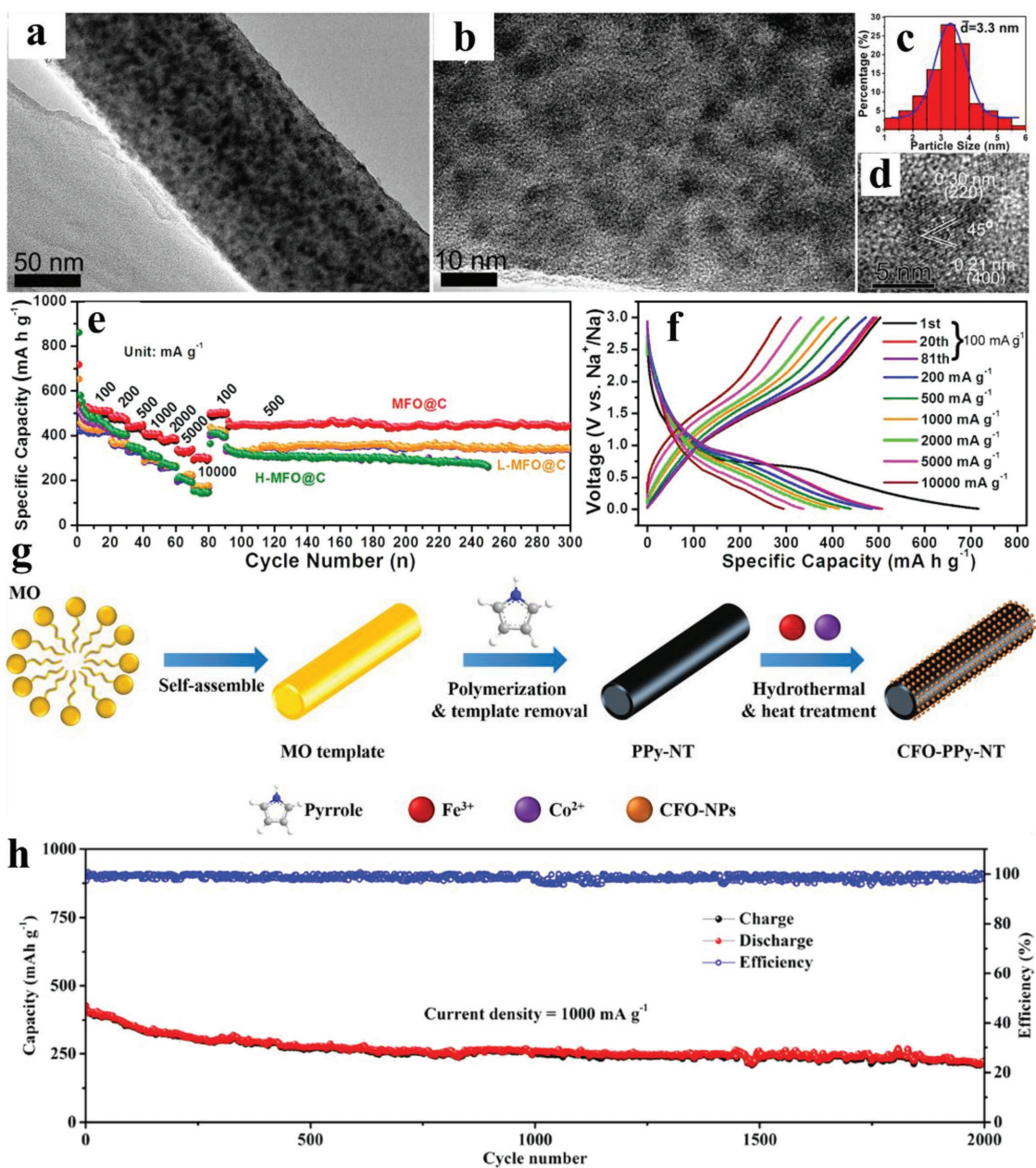


**Figure 8.** a) TEM and b) HRTEM images of the as-prepared MFO@C nanofibers. c) MnFe<sub>2</sub>O<sub>4</sub> particle size distribution diagram and d) lattice fringes. e) Rate capability and cycling performance of MFO@C, L-MFO@C, and H-MFO@C electrodes in the potential window of 0.01.3.0 V. f) Galvanostatic charge/discharge profiles of MFO@C at different rates. g) Fabrication process of the CFO-PPy-NT. h) Long-term cycle performance of CFO-PPy-NTs at 1000 mA g<sup>-1</sup>. a–f) Reproduced with permission.<sup>[61]</sup> Copyright 2016, American Chemical Society. g,h) Reproduced with permission.<sup>[62]</sup> Copyright 2017, American Chemical Society.

homogeneously embedded in carbon matrix (3-CCO@C). As SIB anode material, the 3-CCO@C composite delivers a specific capacity of 314 mAh g<sup>-1</sup> at 1 A g<sup>-1</sup> after 1000 cycles and a reversible capacity of 296 mAh g<sup>-1</sup> at a high current density of 5 A g<sup>-1</sup>. The outstanding cycling performance as well as excellent rate property can be ascribed to N-doped carbon matrix mitigating the large volume expansion and ultrasmall CuCo<sub>2</sub>O<sub>4</sub> nanodots improving the utilization rate. The reaction mechanism of self-supported CCO@C electrode was also investigated. In the initial discharge process, the CuCo<sub>2</sub>O<sub>4</sub> is reduced to Cu and Co. During

the subsequent cycles, the reversible reaction occurs between Co/Cu and Co<sub>3</sub>O<sub>4</sub>/CuO. Fang et al.<sup>[67d]</sup> synthesized the 2D porous hybrid Co<sub>3</sub>O<sub>4</sub>/ZnO nanosheets by annealing CoZn-MOF. The as-prepared CoZn-O<sub>2</sub> nanosheets converted from CoZn(1:1)-MOF consist of numerous ultrathin wafers, displaying mesoporous structure. Benefiting from the porous nanosheets feature and two-phase synergistic effect, the CoZn-O<sub>2</sub> electrode exhibits superior electrochemical property. A specific capacity of 242 mAh g<sup>-1</sup> is achieved at 2 A g<sup>-1</sup> and the corresponding capacity retention can reach at 91% after 1000 cycles.

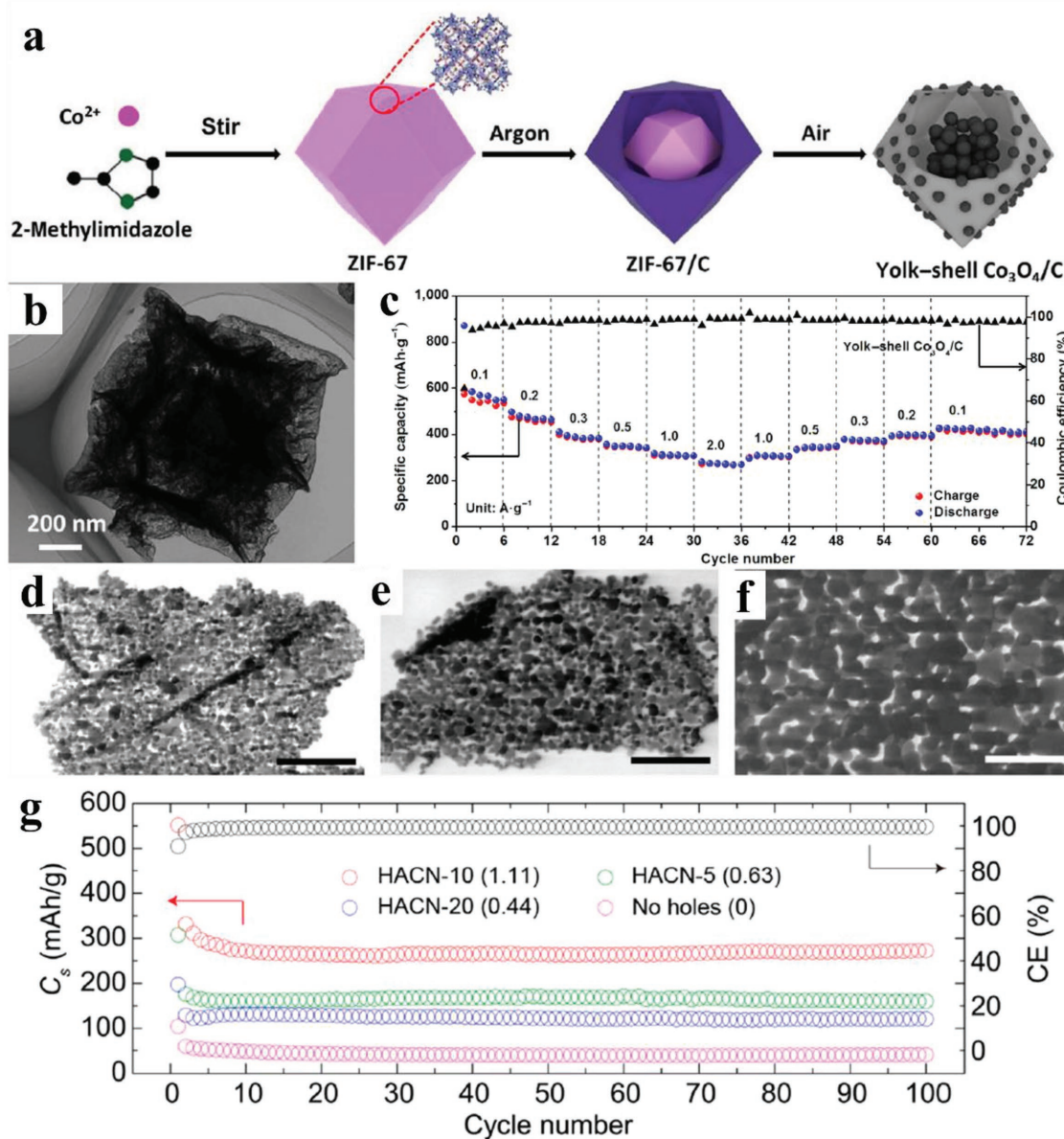


**Figure 9.** a) Schematic of ZIF-67-derived hierarchical yolk-shell  $\text{Co}_3\text{O}_4/\text{C}$  dodecahedrons. b) TEM image of yolk-shell  $\text{Co}_3\text{O}_4/\text{C}$ . c) Rate capability of yolk-shell  $\text{Co}_3\text{O}_4/\text{C}$  tested at rates ranging from 0.1 to 2.0  $\text{A g}^{-1}$ . d–f) STEM images of  $\text{Co}_3\text{O}_4$  HACN-5, HACN-10, and HACN-20, respectively. g) Cycling performance of holey ACN with different pores at 0.8  $\text{A g}^{-1}$  for 100 cycles. a–c) Reproduced with permission.<sup>[63a]</sup> Copyright 2017, Springer. d–g) Reproduced with permission.<sup>[63b]</sup> Copyright 2017, American Chemical Society.

### 5.1.3. Other Metal Oxides

In addition to the above-discussed metal oxide, nickel-based, copper-based, and vanadium-based oxides have also been reported as SIB anode. Zou et al.<sup>[68]</sup> prepared the hierarchical NiO/Ni/graphene composites through carbonization and oxidation treatments of Ni-MOFs. The as-prepared NiO/Ni/graphene composites have a hollow structure with the diameter of 1.5  $\mu\text{m}$ . When investigated as SIB anode, the NiO/Ni/graphene electrode exhibits good cycle life and rate property, benefiting from the ultrafine NiO/Ni nanoparticles, uniform graphene coating, and hierarchical hollow structure. To further improve sodium storage property of NiO, Sun et al.<sup>[69]</sup> fabricated

ultrathin NiO nanosheets through a feasible solvothermal approach followed by annealing in air. The SEM and TEM images show that the obtained NiO has crumpled nanosheet structure with the thickness of 4–5 nm. The ultrathin NiO nanosheets as SIB anode provide a high specific capacity of 299  $\text{mAh g}^{-1}$  at 1  $\text{A g}^{-1}$ . After 100 cycles, the specific capacity still retains at 266  $\text{mAh g}^{-1}$ . The hierarchically porous  $\text{CoNiO}_2$  nanosheet array film fabricated by a feasible solvothermal process followed by annealing treatment was reported Chang et al.<sup>[70]</sup> When employed as SIB negative electrode material, the obtained  $\text{CoNiO}_2$  nanosheet array film shows a large specific capacity of 746.6  $\text{mAh g}^{-1}$  for the 100th cycle at 0.2  $\text{A g}^{-1}$  and a capacity of 419  $\text{mAh g}^{-1}$  at 1.6  $\text{A g}^{-1}$ .

Cupric oxide (CuO) is regarded as a potential negative electrode material for SIBs, owing to its high theoretical capacity (674 mAh g<sup>-1</sup>), low cost, and environmental compatibility. Zhang and co-workers reported the porous CuO nanorod arrays fabricated by engraving copper foils.<sup>[71]</sup> The TEM image confirms that the CuO nanorods contain numerous holes and have a rough surface. The CuO nanorod array electrode exhibits superior sodium storage property, offering a specific capacity of 640 mAh g<sup>-1</sup> at 0.2 A g<sup>-1</sup>. Lu et al.<sup>[72]</sup> synthesized the micro-nanostructured CuO/C spheres by aerosol spray pyrolysis. The obtained CuO/C spheres have a spherical structure with CuO nanoparticles (≈10 nm) uniformly encapsulated in the carbon matrix (10-CuO/C). The 10-CuO/C sphere exhibits superior sodium storage performance due to the robust micro-nanostructure. A discharge capacity of 402 mAh g<sup>-1</sup> can be achieved at 0.2 A g<sup>-1</sup> for the 600th cycle. Chen et al.<sup>[73]</sup> prepared the 3D network structure CuO via in situ engraving approach. The as-prepared CuO sample shows 3D network structure with flower-like porous nanosheets surrounded by nanowires. When tested as negative electrode material for SIBs, the CuO sample provides a specific capacity of 680 and 280 mAh g<sup>-1</sup> at 50 and 1000 mA g<sup>-1</sup>, respectively. Rath et al.<sup>[74]</sup> synthesized ultrafine CuO nanoparticles embedded in mesopores carbons (CMK-3 and CMK-8) by hydrothermal approach. The HRTEM images confirm that the particle sizes of CuO are about 4 and 12 nm in the CuO@CMK-8 and CuO@CMK-3, respectively. The CuO@CMK-8 electrode exhibits a specific capacity of 477 mAh g<sup>-1</sup> at 0.1 A g<sup>-1</sup> for the 200th cycle, corresponding to a high coulombic efficiency of 99.7%. Zhang et al.<sup>[75]</sup> synthesized porous CuO/Cu<sub>2</sub>O hybrid hollow octahedrons by annealing Cu-based MOF templates and investigated their sodium-ion storage properties. The SEM and TEM images confirm that the CuO/Cu<sub>2</sub>O composites are composed of clustered nanoparticles and have porous octahedron structure. Benefiting from the synergistic effect of CuO and Cu<sub>2</sub>O and good mechanical stability resulted from porous structures, the obtained CuO/Cu<sub>2</sub>O electrode shows superior electrochemical performance.

## 5.2. Metal Sulfides

### 5.2.1. Iron-Based Sulfides

Metal sulfides have attracted great attention as SIB negative electrode materials owing to their low cost and high specific capacities. In addition, metal sulfides show enhanced mechanical stability, electrical conductivity, and better reversibility compared to their metal oxide counterparts. Typically, iron sulfides manifest prominent advantages such as natural abundance, environmental benignity, and high theoretical capacity. However, iron sulfides suffer from low conductivity and large volume expansion during cycling process.

To address the above issues, designing various nanostructures and carbon composites have been carried out to improve sodium storage property of iron sulfides.<sup>[76]</sup> For instance, Chen et al.<sup>[76a]</sup> obtained FeS<sub>2</sub>/CNT neural network composite via a simple solvothermal method. The unique nanostructure provides large specific surface area, short ion diffusion pathway, and sufficient space for volume expansion. Therefore, FeS<sub>2</sub>/

CNT composites show a stable capacity of 394 mAh g<sup>-1</sup> at 0.2 A g<sup>-1</sup> for the 400th cycle. Additionally, Li et al.<sup>[76b]</sup> used the double-helix structure in carrageenan-metal hydrogels to fabricate porous metal sulfide/carbon aerogels (M<sub>x</sub>S<sub>y</sub>/CAs). As displayed in **Figure 10a,b**, the as-prepared FeS/CA has a 3D macroporous network and some mesopores can be seen on the surface. The unique structure promotes the ion/electron transport kinetics and stabilizes the structures of M<sub>x</sub>S<sub>y</sub>/CAs, enhancing the sodium-ion storage properties of electrodes. As negative electrode material for SIBs, FeS/CA delivers high reversible capacity and rate performance (Figure 10c). Cho et al.<sup>[77]</sup> prepared the porous FeS nanofibers through electrospinning and subsequent sulfidation. The ultrafine nanovoids form in the FeS nanofibers (Figure 10d), which was caused by Kirkendall effect. Compared to the hollow Fe<sub>2</sub>O<sub>3</sub> nanofibers, the porous FeS nanofibers show robust structure and excellent electrochemical performance for SIBs. The porous FeS nanofibers deliver a high discharge capacity of 592 mAh g<sup>-1</sup> for the 150th cycle at 0.5 A g<sup>-1</sup> (Figure 10e). Cao et al.<sup>[78]</sup> synthesized the chrysanthemum-like carbon/FeS microspheres (CL-C/FeS) by solvothermal method, as displayed in Figure 10f. The SEM image indicates that a large amount of nanosheets assemble into 3D interconnected chrysanthemum-like structure (Figure 10g). As expected, the CL-C/FeS displays outstanding cycling properties with a reversible capacity of 265 mAh g<sup>-1</sup> for the 200th cycle at 1 A g<sup>-1</sup> (Figure 10h), which is much better than commercial FeS. Compared to single metal sulfides, multicomponent metal sulfides deliver better electrochemical performance for SIBs. The large-scale fabrication of uniform Fe<sub>1-x</sub>S nanostructures via a sulfurization treatment of Fe<sub>2</sub>O<sub>3</sub> nanocubes were reported by Li et al.<sup>[79]</sup> The structural features of as-prepared Fe<sub>1-x</sub>S samples are confirmed by TEM. The TEM image exhibits that the obtained Fe<sub>1-x</sub>S has a highly porous structure. The elements of Fe and S are uniformly dispersed in the nanostructures. When employed as negative anode materials for SIBs, the uniform Fe<sub>1-x</sub>S nanostructure electrodes show outstanding sodium storage property. In particular, the large discharge capacity of 563 mAh g<sup>-1</sup> can be preserved at 0.1 A g<sup>-1</sup> after 200 cycles. To explore the commercial application of as-prepared Fe<sub>1-x</sub>S electrodes, a full cell based on Na<sub>0.6</sub>Co<sub>0.1</sub>Mn<sub>0.9</sub>O<sub>2</sub> cathode and Fe<sub>1-x</sub>S anode are assembled. A discharge capacity of 380 mA h g<sup>-1</sup> can be achieved at 20 mA g<sup>-1</sup> for the 100th cycle. Kim and Kang<sup>[59]</sup> prepared yolk-shell structured (Fe<sub>0.5</sub>Ni<sub>0.5</sub>)<sub>9</sub>S<sub>8</sub> powders through spray pyrolysis and postsulfidation process. When applied as negative electrode material for SIBs, the obtained (Fe<sub>0.5</sub>Ni<sub>0.5</sub>)<sub>9</sub>S<sub>8</sub> electrode delivers an initial specific capacity of 601 mAh g<sup>-1</sup> at 1 A g<sup>-1</sup>. The specific capacity of (Fe<sub>0.5</sub>Ni<sub>0.5</sub>)<sub>9</sub>S<sub>8</sub> can maintain 527 mAh g<sup>-1</sup> for 100th cycle.

### 5.2.2. Cobalt-Based Sulfides

Recently, cobalt sulfides have also been investigated as a host material for SIBs because of their high theoretical capacity and earth abundance. Wang et al.<sup>[18a]</sup> designed and synthesized yolk-shell structured Co<sub>9</sub>S<sub>8</sub>/MoS<sub>2</sub>-CN composites for SIBs. Benefiting from the synergistic effects of binary sulfides, in situ N-doped carbon coating, and yolk-shell structure, the Co<sub>9</sub>S<sub>8</sub>/MoS<sub>2</sub>-CN composites provide a high discharge capacity of

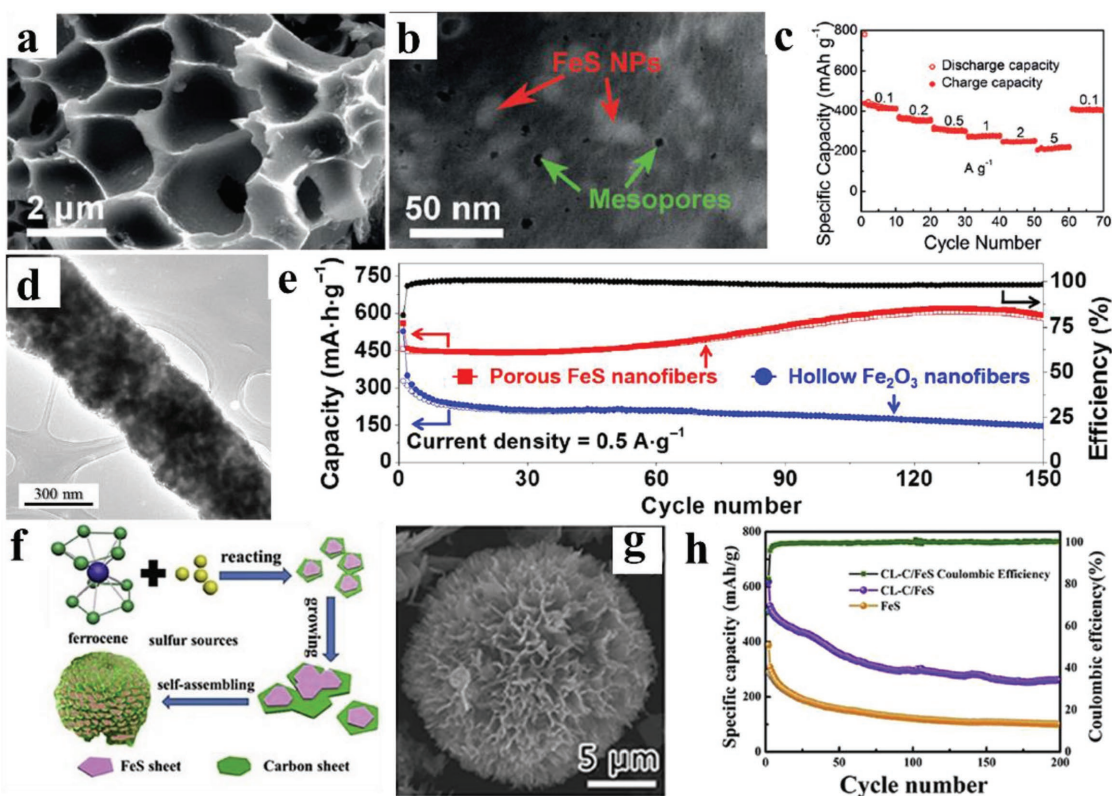


**Figure 10.** a,b) FESEM images of FeS/CA. c) The specific capacity of the FeS/CA at different current densities. d) TEM image of the porous FeS nanofibers containing numerous nanovoids after sulfidation at 400 °C for 8 h. e) Cycle performance of the porous FeS and hollow Fe<sub>2</sub>O<sub>3</sub> nanofibers for sodium-ion storage at a constant current density of 500 mA g<sup>-1</sup>. f) Schematic illustration of the formation process of CL-C/FeS. g) SEM image of CL-C/FeS. h) Cycling performance of commercial FeS and CL-C/FeS at 1 A g<sup>-1</sup>. a–c) Reproduced with permission.<sup>[76b]</sup> Copyright 2016, Wiley-VCH. d,e) Reproduced with permission.<sup>[77]</sup> Copyright 2017, Springer. f–h) Reproduced with permission.<sup>[78]</sup> Copyright 2017, Elsevier.

438 mAh g<sup>-1</sup> at 1 A g<sup>-1</sup> after 150 cycles. Impressively, the stable capacity of 421 mAh g<sup>-1</sup> can be achieved for the 250th cycle at 2 A g<sup>-1</sup>. Han et al.<sup>[80]</sup> synthesized the sandwich-type CNT@CoS@C composite via a bottom-up approach and studied their sodium storage property. According to the electrochemical performance test, the CNT@CoS@C composite shows the corresponding capacity retention of 74% for the 500th cycle at 0.5 A g<sup>-1</sup>. Li et al.<sup>[81]</sup> reported the mesoporous CoS@C yolk-shell microspheres (M-CoS@C). The fabrication process of M-CoS@C samples is schematically illustrated in **Figure 11a**. **Figure 11b** presents the TEM image of M-CoS@C composite, confirming the yolk-shell structure and the carbon shell size of 23 nm. Compared to the capacity of M-CoS decreasing to 55 mAh g<sup>-1</sup> within 5 cycles, the obtained M-CoS@C composite delivers a high specific capacity of 532 mAh g<sup>-1</sup> at 0.2 A g<sup>-1</sup> for the 100th cycle (**Figure 11c**). Moreover, the M-CoS@C electrode displays better rate property than that of M-CoS (**Figure 11d**). The outstanding electrochemical performance of M-CoS@C composite is benefited from the synergistic effect of the mesoporous CoS yolk and alveolus-like carbon shell structure. The ultrasmall CoS nanoparticles encapsulated in carbon nanorods were reported by Zhou et al.<sup>[82]</sup> **Figure 11e** displays the TEM image of the obtained 7-CoS/C (CoS nanoparticles with an average size of 7 nm), exhibiting that the nanorods have the width of ≈200 nm and the length of ≈2 μm. When

employed as negative electrode material for SIBs, the 7-CoS/C provides a capacity of 542 mAh g<sup>-1</sup> at 1 A g<sup>-1</sup> for the 2000th cycle (**Figure 11f**). The discharge capacities are 510 and 356 mAh g<sup>-1</sup> at 5 and 40 A g<sup>-1</sup>, respectively (**Figure 11g**). The long-life cycling property and excellent rate performance of 7-CoS/C are ascribed to the advantageous integration of ultrafine nanoparticles and porous nanorods architecture. The CoS@rGO composite fabricated through a facile solvothermal strategy was reported by Peng et al.<sup>[83]</sup> The TEM image reveals that the CoS nanoplates are distributed on the surface of graphene and have the thickness of about 10 nm (**Figure 11h**). The CoS@rGO composite as SIB negative electrode material exhibits impressive long-life cycling performance, as exhibited in **Figure 11i**. The high specific capacity of 420 mAh g<sup>-1</sup> is achieved even for the 1000th cycle at 1 A g<sup>-1</sup>. Otherwise, the capacity of pure CoS decreases to 263 mAh g<sup>-1</sup> for the 100th cycle, which demonstrates the excellent cyclability of CoS@rGO composite. Han et al.<sup>[84]</sup> prepared CNT-supported CoS@C hollow nanoparticles by a template-free method. The TEM image confirms that the CoS hollow nanoparticles are encapsulated by a thin carbon layer with a uniform thickness of ≈6 nm. The construction of CoS-based hybrid has many advantages, including accelerated electron and ion transport and the enhanced mechanical integrity resulted from 1D conductive networks, hollow structure, and surface carbon layer. When assessed as negative electrode

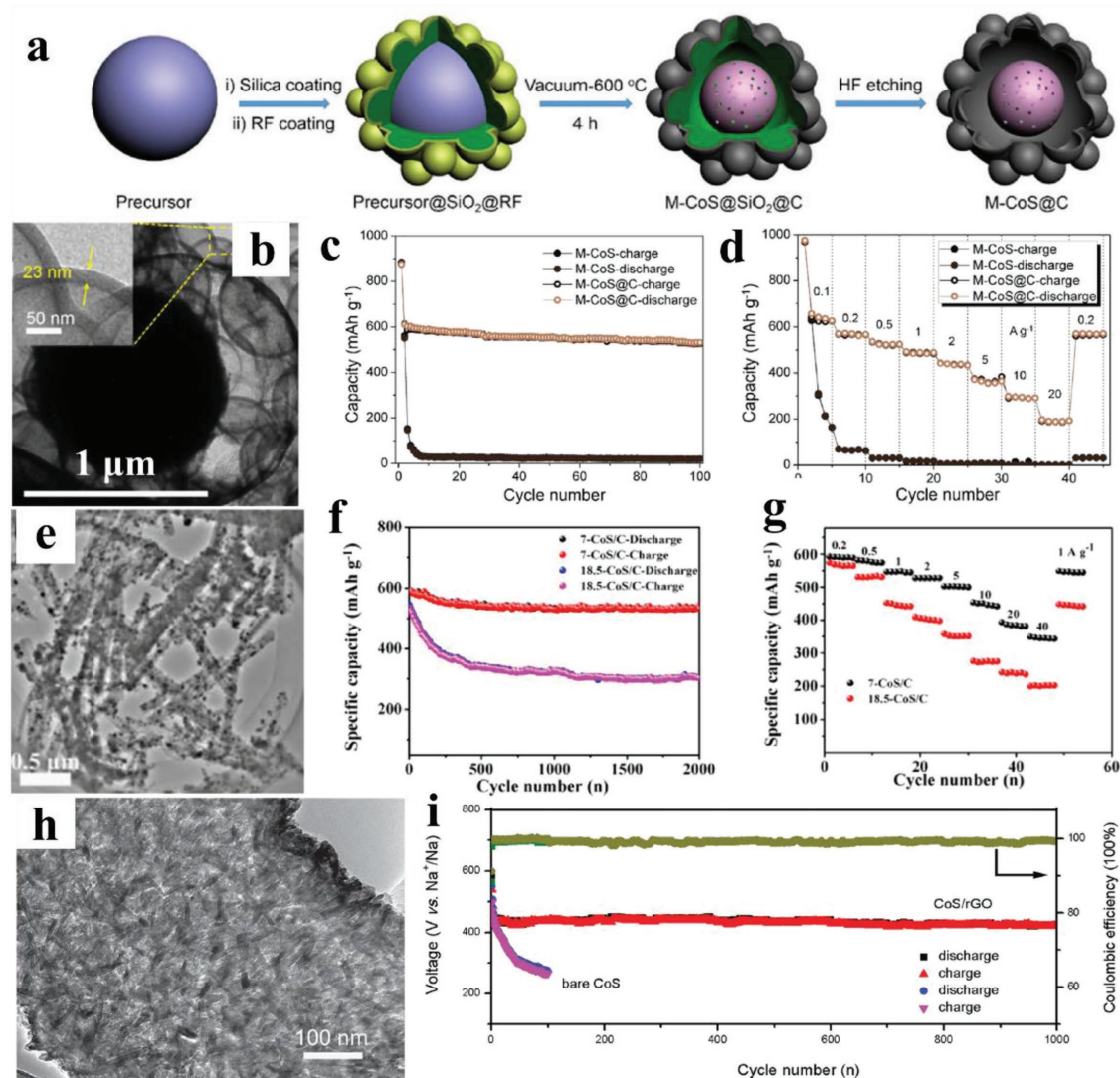


**Figure 11.** a) Schematic illustration of the synthesis of yolk-shell M-CoS@C. b) TEM image of the yolk-shell M-CoS@C. c,d) Cycling performances at  $0.2 \text{ A g}^{-1}$  and rate capability at various current rates of the M-CoS and the yolk-shell M-CoS@C, respectively. e) TEM image of the as-prepared 7-CoS/C. f,g) Cycling performance at a current density of  $1 \text{ A g}^{-1}$  in the voltage range of 0.6–3 V versus  $\text{Na}^+/\text{Na}$  and rate capability of the 7-CoS/C and 18.5-CoS/C electrodes, respectively. h) TEM image of the as-prepared CoS@rGO composite. i) Cycling performance (left) and Coulombic efficiency (right) of the CoS@rGO composite at a current density of  $1 \text{ A g}^{-1}$ . a–d) Reproduced with permission.<sup>[81]</sup> Copyright 2017, Elsevier. e–g) Reproduced with permission.<sup>[82]</sup> Copyright 2017, Elsevier. h,i) Reproduced with permission.<sup>[83]</sup> Copyright 2016, Wiley-VCH.

material for SIBs, the obtained CoS-based hybrids show a reversible capacity of  $562 \text{ mAh g}^{-1}$  at  $0.1 \text{ A g}^{-1}$  and achieve a high capacity retention rate of 90% at  $0.5 \text{ A g}^{-1}$  after 200 cycles. The CoS<sub>2</sub> micro/nanostructure materials synthesized through hydrothermal/solvothermal methods were reported by Liu et al.<sup>[85]</sup> The SEM image reveals that the as-prepared H-CoS<sub>2</sub> samples have hollow structure with the size of  $\approx 3\text{--}4 \mu\text{m}$  and consist of typical octahedrons with the edge length of 300 nm. As SIB anode material, H-CoS<sub>2</sub> electrodes exhibit enhanced electrochemical performance compared with that of P-CoS<sub>2</sub> and O-CoS<sub>2</sub>. In particular, a high specific capacity of  $690 \text{ mAh g}^{-1}$  can be maintained for the 100th cycle  $1 \text{ A g}^{-1}$ . In addition, it is demonstrated that the obtained H-CoS<sub>2</sub> shows better cycling stability in the potential range of 1.0–3.0 V.

### 5.2.3. Other Metal Sulfides

A few other metal sulfides have also been explored as SIB negative electrode materials, such as nickel sulfides and manganese sulfide. Wang et al.<sup>[86]</sup> fabricated NiS<sub>2</sub>-GNS composites through a facile hydrothermal method. When assessed as negative electrode material for SIBs, the NiS<sub>2</sub>-GNS composites deliver specific capacities of 407 and  $168 \text{ mAh g}^{-1}$  at current densities of 0.1 and 2 C, respectively. Zhao et al.<sup>[87]</sup> synthesized NiS<sub>x</sub>/CNT@C composite and applied it as negative electrode material for SIBs. The NiS<sub>x</sub>/CNT@C composite shows hierarchical structure, in which NiS<sub>x</sub> nanoparticles grow on carbon nanotube, wrapped by an ultrathin carbon layer. It offers a reversible specific capacity of  $400 \text{ mAh g}^{-1}$  at  $0.1 \text{ A g}^{-1}$ . After 200 cycles, a

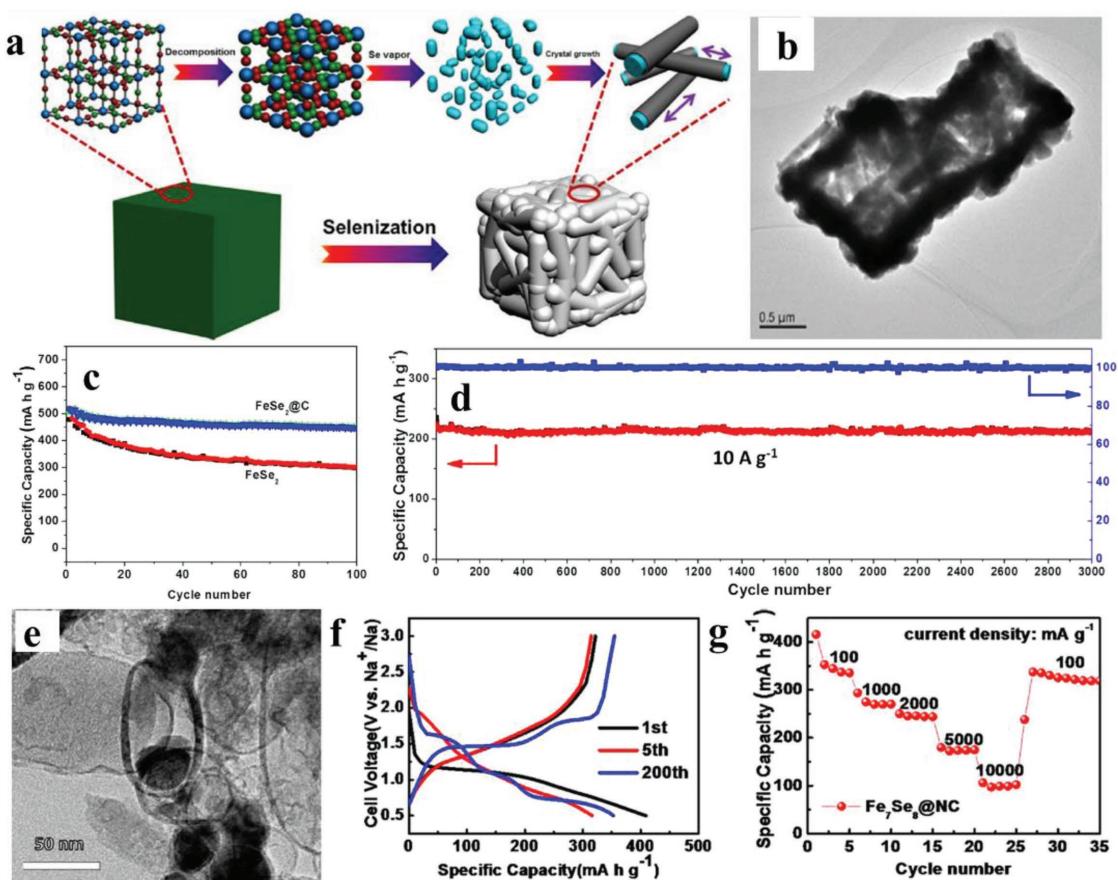


**Figure 12.** a) The formation mechanism of 3D hierarchical iron selenide hollow nanocubes. b) TEM image of the as-prepared  $\text{FeSe}_2@\text{C}$  hollow cubes. c) Cycling performance of  $\text{FeSe}_2@\text{C}$  and  $\text{FeSe}_2$  electrodes at a current density of  $0.1 \text{ A g}^{-1}$ . d) Long-term cycling performance of  $\text{FeSe}_2@\text{C}$  electrode at the current density of  $10 \text{ A g}^{-1}$ . e) TEM image of synthesis of  $\text{Fe}_7\text{Se}_8@\text{NC}$  nanoparticles. f) Charge/discharge curves of  $\text{Fe}_7\text{Se}_8@\text{NC}$  as SIB anode at  $500 \text{ mA g}^{-1}$ . g) Rate performance of  $\text{Fe}_7\text{Se}_8@\text{NC}$  at current densities from 100 to  $10\,000 \text{ mA g}^{-1}$ . a–d) Reproduced with permission.<sup>[92]</sup> Copyright 2017, Elsevier. e–g) Reproduced with permission.<sup>[93]</sup> Copyright 2017, Elsevier.

specific capacity of  $340 \text{ mAh g}^{-1}$  can be maintained. The hollow  $\text{NiS}$  spheres fabricated through a simple refluxing method were reported by Zhang et al.<sup>[88]</sup> The synthesized  $\text{NiS}$  spheres show hierarchical hollow structure with a diameter of  $220 \text{ nm}$ . The unique hollow structure shortens ion diffusion pathway and buffers the volume expansion, enhancing the sodium storage property. The reversible specific capacities of  $683.8$  and  $337.4 \text{ mAh g}^{-1}$  can be achieved at  $0.1$  and  $5 \text{ A g}^{-1}$ , respectively. A specific capacity of  $499.9 \text{ mAh g}^{-1}$  can be retained for the 50th cycle at  $100 \text{ mA g}^{-1}$ , corresponding to capacity retention of 73%. Sun et al.<sup>[89]</sup> prepared mesoporous  $\text{NiS}_2$  nanospheres by facile hydrothermal strategy. When evaluated as negative electrode material for SIBs, the  $\text{NiS}_2$  nanospheres deliver a capacity of  $319 \text{ mAh g}^{-1}$  at  $0.5 \text{ A g}^{-1}$  for the 1000th cycle and a reversible capacity of  $253 \text{ mAh g}^{-1}$  at  $5 \text{ A g}^{-1}$ . Recently, Liu et al.<sup>[90]</sup> synthesized  $\alpha\text{-MnS}@N,S\text{-NTC}$  composite and tested its sodium storage performance. The as-prepared  $\alpha\text{-MnS}@N,S\text{-NTC}$  composite shows the 1D nanostructure with the length of  $0.5\text{--}1 \mu\text{m}$  and diameter of  $100 \text{ nm}$ . For sodium-ion storage, the  $\alpha\text{-MnS}@N,S\text{-NTC}$  composite exhibits a specific capacity of  $291 \text{ mAh g}^{-1}$  at  $250 \text{ mA g}^{-1}$  for the 200th cycle. The  $\alpha\text{-MnS}@N,S\text{-NTC}$  anode and  $\text{Na}_3\text{V}_2(\text{PO}_4)_2\text{O}_2\text{F}$  (NVPOF)

cathode are assembled as full cells, delivering a discharge capacity of  $78 \text{ mAh g}^{-1}$  at  $0.6 \text{ C}$  for the 100th cycle. The results indicate that  $\alpha\text{-MnS}@N,S\text{-NTC}$  composite is a promising anode for SIBs.

### 5.3. Metal Selenides

#### 5.3.1. Iron-Based Selenides

Iron selenides are considered as potential anode materials for SIBs, because of their good conductivity, low cost, and high capacity. Zhang et al.<sup>[91]</sup> fabricated  $\text{FeSe}_2$  microspheres wrapped by sulfur-doped rGO ( $\text{FeSe}_2/\text{SG}$ ) composites via a facile hydrothermal method. When investigated as SIB anode material, the  $\text{FeSe}_2/\text{SG}$  composites exhibit excellent electrochemical performances. To further improve sodium-ion storage performance of  $\text{FeSe}_2$ , Fan et al.<sup>[92]</sup> synthesized hierarchical hollow  $\text{FeSe}_2@\text{C}$  nanocubes through a thermally induced selenization process of Prussian blue microcubes templates (Figure 12a). The TEM image displays that  $\text{FeSe}_2@\text{C}$  nanocubes are assembled by nanorods and possess hierarchical hollow structure, as repre-

sented in Figure 12b. Figure 12c presents the comparison of cycling properties of the  $\text{FeSe}_2@\text{C}$  and  $\text{FeSe}_2$  at  $0.1 \text{ A g}^{-1}$ . It can be observed that the  $\text{FeSe}_2@\text{C}$  electrode provides higher specific capacity than the bare  $\text{FeSe}_2$ . A specific capacity of  $450 \text{ mAh g}^{-1}$  can be retained for the 100th cycle. Impressively, the  $\text{FeSe}_2@\text{C}$  electrode shows ultralong-life cycling stability at  $10 \text{ A g}^{-1}$ , delivering a capacity of  $212 \text{ mAh g}^{-1}$  for the 3000th cycle (Figure 12d). Recently, the  $\text{Fe}_7\text{Se}_8@\text{NC}$  nanoparticles as SIB anode were reported for the first time by Huang and co-workers.<sup>[93]</sup> The  $\text{Fe}_7\text{Se}_8@\text{NC}$  was prepared by a simple thermal method adopting Prussian blue as precursor. The  $\text{Fe}_7\text{Se}_8$  nanoparticles are encapsulated by carbon shell with the thickness of 5–10 nm, as displayed in Figure 12e. Figure 12f displays the discharge/charge profiles of  $\text{Fe}_7\text{Se}_8@\text{NC}$  at  $0.5 \text{ A g}^{-1}$ , revealing that the initial discharge/charge capacities of  $409/322 \text{ mAh g}^{-1}$  can be obtained. According to the rate capability test (Figure 12g), the  $\text{Fe}_7\text{Se}_8@\text{NC}$  delivers reversible capacities of 331 and  $293 \text{ mAh g}^{-1}$  at 0.1 and  $1 \text{ A g}^{-1}$ , respectively.

To enhance the electrochemical performance of iron chalcogenides, Wang et al.<sup>[94]</sup> synthesized a hierarchical microcapsule structured  $\text{FeSe}@FeS$  materials by a solid-state reaction. The hierarchical core-shell structures can effectively buffer the large volume change, enhancing the cycling stability of electrodes. When evaluated as SIB anodes, the obtained  $\text{FeSe}@FeS$  samples show a stable capacity of  $485 \text{ mAh g}^{-1}$  for the 1400th cycle at  $3 \text{ A g}^{-1}$ . Park and Kang<sup>[95]</sup> synthesized 3D multiroom-structured  $(\text{NiFe})\text{Se}_x\text{-GC-CNT}$  composite microspheres by spray pyrolysis and a feasible selenization strategy. The structural features of  $(\text{NiFe})\text{Se}_x\text{-GC-CNT}$  composites are depicted by SEM and TEM. The results demonstrate that the obtained composites have the spherical morphology and tens of empty nanovoids caused by the decomposition of dextrin and phase segregation. The metal selenide nanocrystals possess ultrasmall size lower than 50 nm. Benefiting from the ultrafine  $(\text{NiFe})\text{Se}_x$  nanocrystals and conductive CNT framework, the as-prepared  $(\text{NiFe})\text{Se}_x\text{-GC-CNT}$  composites exhibit superior rate property and outstanding cycle life for SIBs. Specifically, the specific capacity of  $455 \text{ mAh g}^{-1}$  can be achieved at  $300 \text{ mA g}^{-1}$  for the 100th cycle, corresponding to the capacity retention of 92.2% from the second cycle. Hong et al.<sup>[96]</sup> fabricated hierarchical  $(\text{Co}_{1/3}\text{Fe}_{2/3})\text{Se}_2$  nanofibers with fiber-in-tube structure via electrospinning and a subsequent selenization approach. The TEM image depicts that the as-prepared  $(\text{Co}_{1/3}\text{Fe}_{2/3})\text{Se}_2$  samples have the fiber-in-tube structure and the nanofibers are decorated by ultrafine  $(\text{Co}_{1/3}\text{Fe}_{2/3})\text{Se}_2$  nanorods with the thickness of 14.9 nm. When assessed as SIB negative electrode material, the hierarchical  $(\text{Co}_{1/3}\text{Fe}_{2/3})\text{Se}_2$  nanofibers deliver reversible discharge capacities of 585 and  $497 \text{ mAh g}^{-1}$  at current densities of 0.1 and  $5.0 \text{ A g}^{-1}$ , respectively.

### 5.3.2. Cobalt-Based Selenides

Cobalt selenides including CoSe and  $\text{CoSe}_2$  have attracted wide attention for energy storage application due to their high electrochemical activities. Nevertheless, these materials suffer from large volume expansion, leading to poor cycling performance. In recent years, various methods have been adopted to enhance the mechanical stability of cobalt selenide

electrode. For instance, Wu et al.<sup>[97]</sup> synthesized the peapod-like  $\text{CoSe}@carbon$  NWs through a feasible hydrothermal method followed by annealing strategy and applied them as electrode material for SIBs. The diameters of CoSe nanoparticles which embedded in carbon nanowires range from 100 to 200 nm. The capacities of  $\text{CoSe}@carbon$  NWs are 350 and  $327 \text{ mAh g}^{-1}$  at 0.1 and  $0.2 \text{ A g}^{-1}$ , respectively. Zhang et al.<sup>[98]</sup> prepared yolk-shell structured  $\text{CoSe}/\text{C}$  dodecahedra using Co-based MOF as a sacrificial template. The TEM image shows that the  $\text{CoSe}/\text{C}$  dodecahedra have the yolk-shell structure with high porosity and the dodecahedra are composed of numerous ultrasmall nanoparticles. Benefiting from the unique yolk-shell structured mesoporous structure, the  $\text{CoSe}/\text{C}$  composites as SIB anode exhibit a capacity of  $597.2 \text{ mA h g}^{-1}$  at  $0.2 \text{ A g}^{-1}$ . Even at a rate of  $16 \text{ A g}^{-1}$ , the specific capacity can still reach at  $361.9 \text{ mA h g}^{-1}$ . The crumple-structured  $\text{CoSe}_x\text{-rGO}$  composite obtained by spray pyrolysis was reported by Park and Kang.<sup>[99]</sup> The TEM image exhibits that  $\text{CoSe}_x$  nanoparticles are uniformly encapsulated in the crumpled rGO nanosheets (Figure 13a). The  $\text{CoSe}_x\text{-rGO}$  prepared at  $800 \text{ }^\circ\text{C}$  shows superior cycling property, delivering the capacity of  $420 \text{ mAh g}^{-1}$  for the 50th cycle at  $0.3 \text{ A g}^{-1}$  (Figure 13b).

The hollow  $\text{CoSe}_2@\text{C}/\text{CNTs}$  composites with excellent sodium storage performance were reported by Tang et al.<sup>[100]</sup> The  $\text{CoSe}_2@\text{C}/\text{CNTs}$  composites exhibit hollow polyhedral structure, as shown in Figure 13c. Figure 13d represents the rate performances of  $\text{CoSe}_2@\text{C}/\text{CNTs}$ ,  $\text{CoSe}_2@\text{GC}$ , and bare  $\text{CoSe}_2$ . The results indicate that the  $\text{CoSe}_2@\text{C}/\text{CNTs}$  possess better rate capability than that of  $\text{CoSe}_2@\text{GC}$  and bare  $\text{CoSe}_2$ . Kang and co-workers synthesized the box-in-box structured  $\text{Co}/(\text{NiCo})\text{Se}_2$  nanocubes.<sup>[101]</sup> The TEM image shows that outer Ni-Co selenide shell has the thickness of 60 nm (Figure 13e). The unique yolk-shell structures can efficiently accommodate large volume change during cycling process, enhancing sodium storage property of electrode materials. Figure 13f shows the cycling performances of  $\text{Co}/(\text{NiCo})\text{Se}_2$  and  $\text{CoSe}_2$  nanocubes. It can be observed that the  $\text{Co}/(\text{NiCo})\text{Se}_2$  electrode exhibits higher capacity than  $\text{CoSe}_2$  electrode, owing to the unique yolk-shell structure and synergistic effect of the multicomponent selenide composition. Recently, Fang et al.<sup>[102]</sup> prepared hierarchical Cu-doped  $\text{CoSe}_2$  ( $\text{Cu-CoSe}_2$ ) microboxes as high-performance SIB anode material. The  $\text{Cu-CoSe}_2$  microboxes assembled by nanosheets are synthesized via sequential ion exchange, as schematically illustrated in Figure 13g. The TEM image indicates that the  $\text{Cu-CoSe}_2$  microboxes possess the hierarchical hollow structure (Figure 13h). Compared to the  $\text{CoSe}_2$  microboxes, the  $\text{Cu-CoSe}_2$  electrode displays excellent cycling property with the capacity retention of 94% for the 500th cycle at  $1 \text{ A g}^{-1}$  (Figure 13i). Ge et al.<sup>[103]</sup> synthesized 3D hierarchical structure materials composed of cobblestone-like  $\text{CoSe}_2/\text{C}$  nanospheres. In the fabrication process, the citric acid can act as chelating agent and carbon precursor. The 3D hierarchical framework and porous structure are confirmed by SEM image, which facilitates the penetration of electrolyte and shorten ion diffusion pathway. The TEM image demonstrates that the cobblestone-like nanospheres with the size of less than 25 nm are uniformly distributed in the carbon framework. The unique structure increases the reaction active sites of electrodes, enhancing their electrochemical performance for sodium-ion

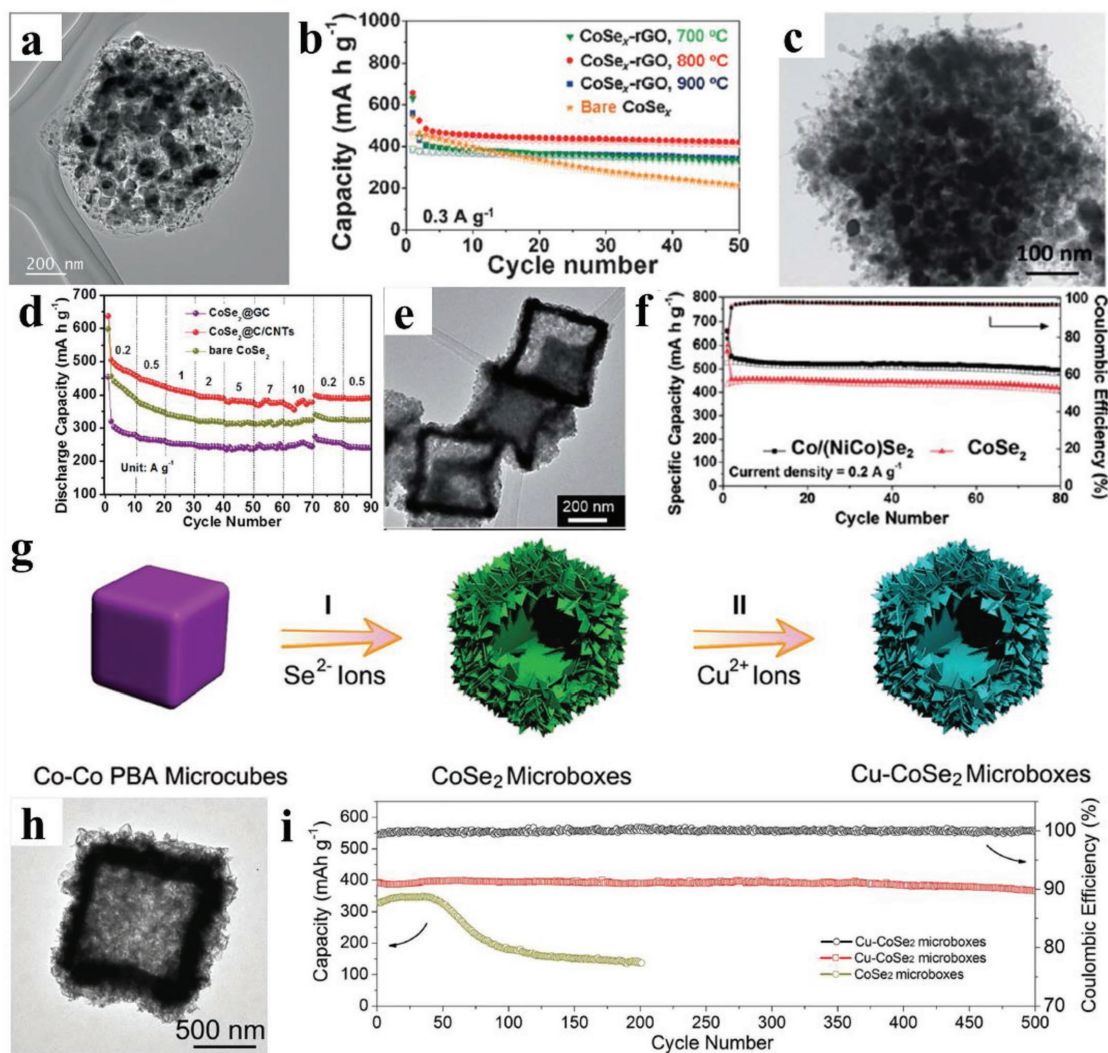


**Figure 13.** a) TEM image of  $\text{CoSe}_2$ -rGO composite powders prepared at 800 °C. b) Cycling performance of the bare  $\text{CoSe}_2$  and  $\text{CoSe}_2$ -rGO composite powders. c) TEM image of  $\text{CoSe}_2$ @C/CNTs, exhibiting the polyhedral  $\text{CoSe}_2$ @C/CNTs integrated with tangled CNTs and carbon-coated  $\text{CoSe}_2$  nanospheres. d) Rate capability of  $\text{CoSe}_2$ @C/CNTs,  $\text{CoSe}_2$ @GC, and bare  $\text{CoSe}_2$  anodes. e) TEM image of the  $\text{Co}/(\text{NiCo})\text{Se}_2$  nanocubes with box-in-box structure. f) Cycling performances and coulombic efficiencies of the  $\text{Co}/(\text{NiCo})\text{Se}_2$  and  $\text{CoSe}_2$  nanocubes at a current density of 0.2 A g<sup>-1</sup>. g) Schematic illustration of the two-step ion-exchange reactions for the synthesis of  $\text{Cu-CoSe}_2$  microboxes. h) TEM image of  $\text{Cu-CoSe}_2$  microboxes. i) Cycling performances of the  $\text{CoSe}_2$  and  $\text{Cu-CoSe}_2$  microbox electrodes at a current density of 1 A g<sup>-1</sup>. a,b) Reproduced with permission.<sup>[99]</sup> Copyright 2016, Wiley-VCH. c,d) Reproduced with permission.<sup>[100]</sup> Copyright 2017, Royal Society of Chemistry. e,f) Reproduced with permission.<sup>[101]</sup> Copyright 2017, Royal Society of Chemistry. g-i) Reproduced with permission.<sup>[102]</sup> Copyright 2018, Wiley-VCH.

storage. The as-prepared  $\text{CoSe}_2/\text{C}$  electrodes exhibit an initial discharge capacity of 545 mAh g<sup>-1</sup> at 0.5 A g<sup>-1</sup>, achieving a coulombic efficiency of 85.6%. Impressively, the specific capacity can still remain at 345 mAh g<sup>-1</sup> at 4.5 A g<sup>-1</sup> for the 10 000th cycle, indicating the ultralong cycling stability of obtained  $\text{CoSe}_2/\text{C}$  samples.

### 5.3.3. Other Metal Selenides

Recently, some work reported that nickel selenides, copper selenides, and zinc selenides are promising negative electrode materials for SIBs because of their unique physiochemical properties. Cho et al.<sup>[53]</sup> synthesized  $\text{NiSe}_2$ -rGO-C composite

nanofibers through electrospinning followed by selenization strategy. When investigated as SIB anode materials, the  $\text{NiSe}_2$ -rGO-C composite electrodes deliver an initial discharge capacity of 717 mAh g<sup>-1</sup> at 0.2 A g<sup>-1</sup> and remain at 468 mAh g<sup>-1</sup> for the 100th cycle. Fan et al.<sup>[104]</sup> fabricated 2D structured  $\text{NiSe}_2$  nanoplates via a simple MOF-template method. The  $\text{NiSe}_2$  nanoplates consist of numerous nanocrystals with the size ranging from 10 to 100 nm, coated by a carbon layer with several nanometers thick. A discharge capacity of 318 mAh g<sup>-1</sup> can be achieved at 1 A g<sup>-1</sup> for the 100th cycle due to the unique structure of  $\text{NiSe}_2$  nanoplates. The  $\text{NiSe}_2$  nanooctahedra prepared by hydrothermal approach was reported by Zhu et al.<sup>[105]</sup> The SEM and TEM images show that the obtained  $\text{NiSe}_2$  nanooctahedra possess single crystal of cubic structure with the size of

150–250 nm. As negative electrode material for SIBs, the NiSe<sub>2</sub> nanooctahedra electrode delivers an initial Coulombic efficiency of over 90%, specific capacity of 313 mAh g<sup>-1</sup> at 5 A g<sup>-1</sup> after 4000 cycles and 175 mAh g<sup>-1</sup> at 20 A g<sup>-1</sup>. The Ni<sub>0.85</sub>Se/C hollow nanowires synthesized using Se/C nanowires as templates were reported by Yang et al.<sup>[106]</sup> The as-prepared Ni<sub>0.85</sub>Se/C hollow nanowires have the diameter of 350–400 nm and many nanoparticles are dispersed on the surface of nanowires. As SIB anode, the Ni<sub>0.85</sub>Se/C hollow nanowires can provide a specific capacity of 390 mAh g<sup>-1</sup> at 0.2 C after 100 cycles. The excellent electrochemical property is ascribed to the tubular carbon framework.

Xu et al.<sup>[107]</sup> fabricated the carbon-encapsulated metal selenides via a general MOF-derived selenidation method. The synthesized NiSe@C composite exhibits hierarchical hollow microsphere structure, in which NiSe nanoparticles have a size of tens of nanometers and are encapsulated by graphene-like carbon matrix. The obtained Cu<sub>2</sub>Se@C shows uniform octahedron structure with a rough and porous surface, and the small Cu<sub>2</sub>Se nanoparticles are embedded in carbon framework. When employed as SIB negative electrode material, the NiSe@C composite shows a large capacity of 325 mAh g<sup>-1</sup> at 0.3 A g<sup>-1</sup> for the 45th cycle and maintains a capacity of 160 mAh g<sup>-1</sup> at 3 A g<sup>-1</sup> after 2000 cycles. The as-prepared Cu<sub>2</sub>Se@C composite exhibits a specific capacity of 268 mAh g<sup>-1</sup> at 0.1 A g<sup>-1</sup> for the 100th cycle. Li et al.<sup>[108]</sup> reported the Cu<sub>2-x</sub>Se nanorods prepared by a feasible water evaporation-induced self-assembly process and applied them as negative electrode materials for SIBs. The morphological features of obtained Cu<sub>2-x</sub>Se samples are revealed by SEM and TEM. The results indicate that the Cu<sub>2-x</sub>Se samples have 1D rod-like structure with diameters of 300–800 nm. Because of the excellent electronic conductivity and 1D structure, the Cu<sub>2-x</sub>Se samples manifest excellent cycling performance and good rate capability. Tang et al.<sup>[109]</sup> fabricated ZnSe/multiwalled carbon nanotube (MWCNT) composites through a facile hydrothermal and a subsequent grinding process. In the obtained composites, ZnSe microspheres possess a porous architecture with a uniform diameter of 2 μm and consist of numerous nanoparticles. Owing to the continuous electron transport path and superior stress relaxation, the as-prepared ZnSe/MWCNT composites deliver a high initial Coulombic efficiency of 88% and the discharge capacity of 382 mAh g<sup>-1</sup> can be maintained for the 180th cycle at 0.5 A g<sup>-1</sup>. The excellent sodium storage property of ZnSe/MWCNT composites makes them a promising anode for SIBs.

#### 5.4. Other Metal Compounds

In recent years, other metal compounds based on conversion reactions such as metal phosphides, metal nitrides, and metal fluorides have also been evaluated as promising negative electrode materials for SIBs. For example, Zhang et al.<sup>[110]</sup> fabricated FeP<sub>4</sub> samples through a simple ball milling. The as-prepared FeP<sub>4</sub> particles with a wide size range of 1–10 μm are revealed by SEM images. When evaluated as SIB anode, the obtained FeP<sub>4</sub> electrodes deliver a large initial specific capacity of 1137 mAh g<sup>-1</sup> at 89 mA g<sup>-1</sup> and a high Coulombic efficiency of 84.0%. Li et al.<sup>[111]</sup> synthesized RGO@CoP@C–FeP composite by a low-temperature phosphorization

approach. The SEM and TEM images reveal that the RGO@CoP@C–FeP composite has core–shell structure, composed of porous FeP core, CoP shell, and wrinkled RGO nanosheets (Figure 14a,b). When used as SIB anode material, the RGO@CoP@C–FeP composite displays outstanding electrochemical performance. Figure 14c displays the cycling performance of RGO@CoP@C–FeP, CoP@C–FeP, and C–FeP electrodes at 0.1 A g<sup>-1</sup>. It can be observed that the RGO@CoP@C–FeP electrode delivers higher discharge capacity than CoP@C–FeP and C–FeP electrode. The improved property of RGO@CoP@C–FeP electrode is attributed to the unique core–shell structure and well-designed components. The core–shell structures can efficiently accommodate the volume expansion of materials during cycling process, enhancing the structural stability of materials. The RGO nanosheets improve the charge transfer kinetics of electrode materials, leading to a high rate capability. The CoP/CNS composite (CoP-O) synthesized by one-step calcination of Co-MOF and red P was reported by Zhang et al.<sup>[112]</sup> The CoP nanoparticles with an average size of 11.3 nm are uniformly dispersed in nitrogen-doped CNSs, as shown in Figure 14d. Benefiting from the robust P–C bonds and conductive CNSs, the CoP/CNS composite exhibits the long-life cycling performance and excellent rate property (Figure 14e). The capacities at different rates of 0.1 and 20 A g<sup>-1</sup> are 598 and 174 mAh g<sup>-1</sup> based on the total mass of the composite. The reaction mechanism of CoP/CNS composite was revealed by X-ray diffraction (XRD), X-ray photoelectron spectroscopy (XPS), X-ray absorption near edge structure (XANES) spectroscopy, and HRTEM. During the discharge process, CoP is transformed to Co and Na<sub>3</sub>P after sodiation. When the electrode is charged to 2.5 V, the CoP can be reproduced. Li et al.<sup>[113]</sup> prepared CoP nanoparticles via a simple ball milling process. The obtained CoP samples exhibit the amorphous characteristics conformed by TEM image. The CoP nanoparticles as SIB anode display a large initial capacity of 770 mAh g<sup>-1</sup> at 100 mA g<sup>-1</sup>. The Co<sub>2</sub>P–3D PNC composites synthesized by a cobalt nitrate-induced polyvinylpyrrolidone (PVP)-blowing and subsequent phosphidation method were reported by Zhou and Fan.<sup>[114]</sup> The SEM images show that the as-prepared Co<sub>2</sub>P–3D PNC composites have a 3D porous that is 5–25 nm. The unique architecture of obtained Co<sub>2</sub>P–3D PNC composites offers great merits of short ion diffusion distance, excellent structural stability, and enhanced electronic transport, leading to high reversible capacity, long-life cycling performance, and outstanding rate property. The obtained Co<sub>2</sub>P–3D PNC electrodes provide a high discharge specific capacity of 827 mAh g<sup>-1</sup> for initial cycle at 50 mA g<sup>-1</sup>. The specific capacity can be retained at 271 mAh g<sup>-1</sup> at 500 mA g<sup>-1</sup> for the 700th cycle.

Wu et al.<sup>[115]</sup> fabricated the Ni<sub>2</sub>P@CpGN sample by assemble and self-template method. The Ni<sub>2</sub>P nanoparticles possess an average size of 24 nm, encapsulated in porous graphene network (Figure 14f). When evaluated as SIB anode, Ni<sub>2</sub>P@CpGN electrode exhibits better cycling performance than that of Ni<sub>2</sub>P@carbon. The charge capacity can still maintain 161 mAh g<sup>-1</sup> at 0.2 A g<sup>-1</sup> for the 100th cycle, corresponding to a capacity retention of 89% (Figure 14g). Miao et al.<sup>[116]</sup> fabricated Ni<sub>2</sub>P@carbon/graphene aerogel (GA) 3D interconnected porous structure material via a solvothermal reaction followed by phosphorization strategy and evaluated its

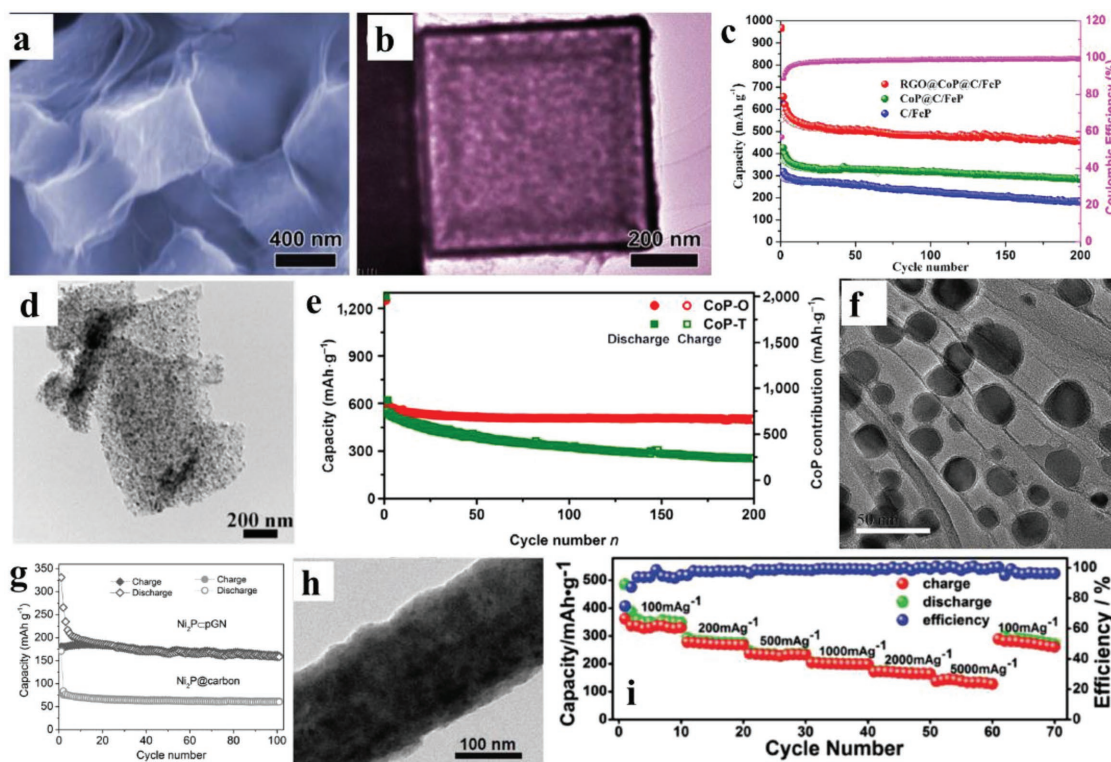


**Figure 14.** a) SEM image of the RGO@CoP@FeP composites. b) A typical TEM image of core-shell structured CoP@FeP microcube. c) Cycling performance of the RGO@CoP@C-FeP, CoP@C-FeP, and C-FeP electrodes. d) TEM images of the as-prepared CoP-O. e) Cyclic performance of CoP-O and CoP-T at a current density of  $0.1 \text{ A g}^{-1}$ . f) TEM image of the obtained  $\text{Ni}_2\text{P@CpGN}$ . g) Cycling performance of the  $\text{Ni}_2\text{P@CpGN}$  and  $\text{Ni}_2\text{P@carbon}$  electrodes at  $0.2 \text{ A g}^{-1}$ . h) TEM image of the as-prepared  $\text{Cu}_3\text{P}$  nanowires. i) Rate capability of CPNWs at different current densities from 100 to  $5000 \text{ mA g}^{-1}$ . a–c) Reproduced with permission.<sup>[111]</sup> Copyright 2017, Elsevier. d,e) Reproduced with permission.<sup>[112]</sup> Copyright 2017, Springer. f,g) Reproduced with permission.<sup>[115]</sup> Copyright 2016, Wiley-VCH. h,i) Reproduced with permission.<sup>[118]</sup> Copyright 2016, Wiley-VCH.

sodium storage property. The detailed morphological features of  $\text{Ni}_2\text{P@C/GA}$  were characterized by TEM. The TEM images display that the  $\text{Ni}_2\text{P}$  nanoparticles coated by carbon layers are uniformly encapsulated in GA nanosheets. As negative electrode material for SIBs, the obtained  $\text{Ni}_2\text{P@C/GA}$  composites deliver long-life cycling performance and excellent rate capability owing to their well-designed structure.  $\text{NiP}_3$  sample synthesized via ball milling and ceramic approach was reported by Fullenwarth et al.<sup>[117]</sup> The electrochemical mechanism was investigated by in situ XRD method. The XRD analysis reveals that the  $\text{Na}_3\text{P}$  and nanosized Ni particles were produced during the initial discharge process. The amorphous phase appears after the first charge. When tested as SIB anode, the  $\text{NiP}_3$  electrodes exhibit a high capacity of  $900 \text{ mAh g}^{-1}$  at C/10 for the 15th cycle. Yan and co-workers reported  $\text{Cu}_3\text{P}$  nanowire via in situ growth and subsequent phosphidation strategy.<sup>[118]</sup> Figure 14h displays the TEM image of the  $\text{Cu}_3\text{P}$  nanowire, indicating that the  $\text{Cu}_3\text{P}$  nanowire consists of much smaller nanoparticles. According to the rate performance test, the as-prepared  $\text{Cu}_3\text{P}$  nanowire as SIB anode delivers stable cycling performance and good rate capability (Figure 14i). The ex situ XRD results confirm the high reversibility of conversion reaction mechanism between  $\text{Cu}_3\text{P}$  and Na. Zhao et al.<sup>[119]</sup> synthesized nanostructured  $\text{CuP}_2/\text{C}$  composites through high energy ball milling method. From

the SEM and TEM images, it can be found that the obtained  $\text{CuP}_2/\text{C}$  composites consist of sub-micrometer sized particles with a size of 30–50 nm. The crystalline  $\text{CuP}_2$  cores are coated by carbon layer with 2–5 nm thickness. The carbon layer can enhance the electrical conductivity and buffer large volume expansion of electrodes. Thus, the as-prepared  $\text{CuP}_2/\text{C}$  composites deliver high specific capacity and high-rate property.

In addition, Cui et al.<sup>[120]</sup> synthesized the mesoporous VN microparticles through solid–solid phase separation. The VN exhibits a high conductivity of  $1.23 \times 10^4 \text{ S cm}^{-1}$ . The SEM image displays the well-defined mesoporosity of VN microparticles. For sodium-ion storage, the mesoporous VN microparticles deliver a capacity of  $300 \text{ mAh g}^{-1}$  at 0.1 C and a capacity of  $100 \text{ mAh g}^{-1}$  can be achieved after 1000 cycles at 2 C. The excellent cycling performance is ascribed to unique conductive wiring networks. Recently, Kong et al.<sup>[121]</sup> synthesized  $\text{NH}_4\text{FeF}_3/\text{CNS}$  composites through a simple coprolysis method. The  $\text{NH}_4\text{FeF}_3$  nanoparticles anchored on carbon sheets have a diameter in a range from 30 to 100 nm.  $\text{NH}_4\text{FeF}_3$  has unique perovskite structure, which is beneficial for sodium-ion storage. When assessed as negative electrode material for SIBs, the  $\text{NH}_4\text{FeF}_3/\text{CNS}$  composites exhibit high specific capacity and good rate property. The improved sodium storage property of  $\text{NH}_4\text{FeF}_3/\text{CNS}$  composites can be ascribed to the open framework structure of  $\text{NH}_4\text{FeF}_3$  and conductive carbon network.

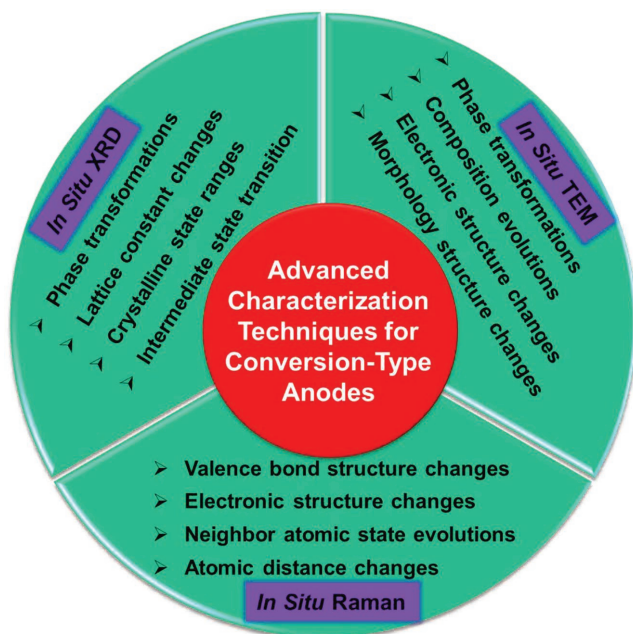


**Figure 15.** General functions of advanced in situ characterization techniques.

## 6. Advanced Techniques for Understanding Electrochemical Mechanism

According to above discussions on the different nanostructured conversion-type anode materials for SIBs, the in-depth understanding of the material behaviors under complex electrochemical environment is critical for making major breakthrough in the next generation of SIBs.<sup>[11a,122]</sup> The dynamic conditions inside a working SIBs are not intensively explored until the

various advanced in situ characterization techniques have been developed.<sup>[123]</sup> This part focuses on the advanced techniques for understanding electrochemical mechanism of the conversion-type anode materials, including in situ XRD, in situ TEM, and in situ Raman spectroscopy. In order to summarize the pivotal roles of the above advanced characterization techniques for conversion-type anode in SIBs, their general functions are proposed (Figure 15).

### 6.1. In Situ XRD

In situ XRD, as an effective tool to acquire the information of structure evolution during electrochemical process, has been widely used for detecting the capacity fading intrinsic mechanism in SIBs.<sup>[122a,124]</sup> The intermediate state, lattice constant changes, crystalline state ranges, and phase transformations will be directly tracked in real time by in situ XRD, which are of great significance in achieving superior energy storage performance.<sup>[122b,125]</sup> For conversion-type anode in SIBs, the in situ XRD plays an important role to optimizing and building better electrode materials, especially operando characterization and in-depth understanding of the irreversible transformation in the initial electrochemical processes.<sup>[126]</sup> Ou et al.<sup>[127]</sup> reported a hierarchical structured NiSe<sub>2</sub>/rGO hybrid anode by a facile one-pot approach. The hybrid anode delivers high specific capacity, enhanced cycling, and rate property when tested in SIBs. Furthermore, the reaction mechanism of two-step reversible process during sodiation/desodiation was revealed by advanced in situ XRD technique. The three obvious peaks appeared in ending of discharge process (discharged to 0.4 V), which are well indexed to Na<sub>2</sub>Se, demonstrating the formation of the Na<sub>2</sub>Se and Ni metal (Figure 16a,b). When charged back to 1.9 V, the peaks of Na<sub>2</sub>Se are disappeared, and Na<sub>x</sub>NiSe<sub>2</sub>

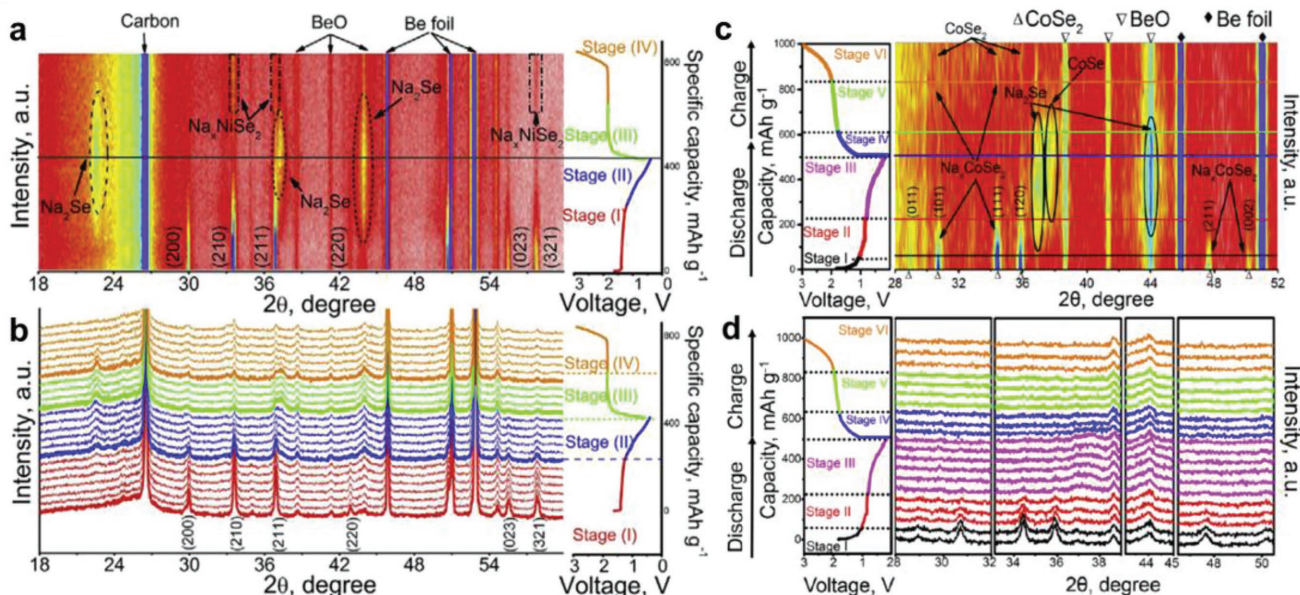


**Figure 16.** a) Contour plots and b) line plot of in situ XRD results of NiSe<sub>2</sub> electrode during the first cycle at 0.4–3.0 V. c) Contour plots and d) line plot of in situ XRD results of CoSe<sub>2</sub> electrode during the first cycle at 0.01–3.0 V. a,b) Reproduced with permission.<sup>[127]</sup> Copyright 2017, Elsevier. c,d) Reproduced with permission.<sup>[128]</sup> Copyright 2017, Elsevier.

phase has been observed, suggesting the reaction of  $\text{Na}_2\text{Se}$  and Ni metal. After charged to 3.0 V, all of the peaks are reappeared, indicating a reversible structure evolution. Additionally, the in situ XRD patterns of  $\text{NiSe}_2/\text{rGO}$  hybrid anode were conducted with the electrochemical test window of 0.01–3 V. The results demonstrating that some parts of the  $\text{NiSe}_2$  suffer from irreversible phase transformation, leading a severe capacity fading during cycling.

Same research group also systematically studied the sodium storage mechanism of  $\text{CoSe}_2$  anode based on conversion-type reactions by in situ XRD.<sup>[128]</sup> Different with the  $\text{NiSe}_2$ , the  $\text{CoSe}_2$  anode goes through three stages during desodiation and desodiation processes at electrochemical test window of 0.01–3.0 V (Figure 16c,d). The two peaks of  $\text{Na}_2\text{Se}$  and one peak of  $\text{CoSe}$  are observed when discharged to 0.8 V, suggesting new phases are formed. At the end of discharge, the additional capacity of 300  $\text{mAh g}^{-1}$  is attributed to the entire formation of  $\text{Na}_2\text{Se}$  and Co metal. When charged to 1.8 V, the peaks of  $\text{Na}_2\text{Se}$  are gradually disappeared, but the peaks of  $\text{CoSe}$  get enhanced, manifesting a reversible conversion-type reaction between  $\text{Na}_2\text{Se}$  and Co metal. When charged back to 3.0 V, the low crystallinity  $\text{CoSe}_2$  phase is observed again, suggesting the reversible reaction mechanism. Therefore, Ou et al. demonstrate that the lower electrochemical reversibility of the anode measured with 0.01–3.0 V exists with a deep conversion reaction of  $\text{CoSe}$  to form  $\text{Na}_2\text{Se}$  and Co, based on in situ XRD tests under different electrochemical windows.

Villevieille and co-workers reported two candidates of  $\text{Cu}_{0.5}\text{TiOPO}_4$  and  $\text{Fe}_{0.5}\text{TiOPO}_4$  as SIB anodes.<sup>[126b]</sup> Both two anode materials have the same space group of  $\text{P2}_1/\text{C}$ , and their crystal structure consists of corner-sharing  $\text{TiO}_6$  octahedral forming long Ti–O chains parallel to the *c*-axis. The chains are connected by  $\text{PO}_4$  tetrahedra. The  $\text{MO}_6$  octahedra share two faces with  $\text{TiO}_6$  octahedra and four corners with  $\text{PO}_4$  tetrahedra.<sup>[129]</sup>  $\text{Cu}_{0.5}\text{TiOPO}_4$  shows no obvious potential plateau with a solid-solution-like behavior upon sodiation process, leading a low discharge capacity.  $\text{Fe}_{0.5}\text{TiOPO}_4$  shows a higher specific capacity than  $\text{Cu}_{0.5}\text{TiOPO}_4$ . The reaction mechanism of the  $\text{Fe}_{0.5}\text{TiOPO}_4$  is revealed by in situ XRD analysis at the potential window of 0.01–3 V and a current density of 16.9  $\text{mA g}^{-1}$ . The anode material turns amorphous rapidly with  $\text{Fe}^{2+}$  reduced to Fe metal during first discharge process. It is significant that the amorphisation process is irreversible in following charge process. Therefore, the sodium storage mechanism of the  $\text{Fe}_{0.5}\text{TiOPO}_4$  is a typical conversion-type reaction, which is also demonstrated.

## 6.2. In Situ TEM

An in-depth understanding of anode electrode morphological structure evolutions in complex electrochemical environment is critical for the development of advanced materials for the next-generation SIBs.<sup>[123]</sup> Researchers also open the sodium ion cells to check the state changes during the sodiation or desodiation, but the observed results are not authentic for the morphological structure that will be destroyed during the disassembly process. To overcome this technical pain point, in situ TEM technique is emerging as a powerful and effective tool for detecting the

phase transformations and microstructure evolutions of electrode materials in real time.<sup>[123,130]</sup>

The in situ TEM technique has been used for observing the microstructure and composition of conversion-type anode materials in SIBs, such as  $\text{CuO}$ ,<sup>[131]</sup>  $\text{SnO}_2$ ,<sup>[132]</sup>  $\text{ZnO}$ ,<sup>[133]</sup>  $\text{V}_2\text{O}_3$ ,<sup>[134]</sup>  $\text{MoO}_3$ ,<sup>[135]</sup>  $\text{Co}_9\text{S}_8$ ,<sup>[136]</sup>  $\text{FeF}_2$ ,<sup>[137]</sup> and so on. Wang and co-workers<sup>[131]</sup> reported the real time sodiation behavior of  $\text{CuO}$  nanowires visualized directly in a solid sodium cell. The time-lapsed images show that the  $\text{CuO}$  nanowires retained a conical morphology during the sodiation, indicating the process from the surface to the center of the nanowires. Moreover, the expansion along the radial direction of  $\text{CuO}$  nanowires is nearly 27%, manifesting an anisotropic mechanism of the sodiation process (Figure 17a). To accurately identify the sodiation phase, high-resolution TEM images from two different sodiation  $\text{CuO}$  nanowires are conducted during following cycles. On the basis of the in situ TEM results, the sodiation process consisted of three steps. First,  $\text{Cu}_2\text{O}$  and  $\text{Na}_2\text{O}$  were predominantly formed. Second, the intermediate phase of  $\text{NaCuO}$  was nucleated. Finally, the full sodiation products of  $\text{Na}_6\text{Cu}_2\text{O}_6$ ,  $\text{Na}_2\text{O}$ , and Cu were obtained. This work demonstrated that the electrochemical reaction mechanism of  $\text{CuO}$  anode material is a typical conversion reaction.

Wang and co-workers<sup>[132]</sup> employed a state-of-the-art in situ TEM electrochemical detecting technique to directly observe the structural and chemical changes of  $\text{SnO}_2$  nanowires during charge/discharge processes in SIBs. During the first sodiation, the  $\text{Na}_2\text{O}$  shell began to form under the surface of  $\text{SnO}_2$  nanowires. The overall diameter of the  $\text{SnO}_2$  nanowire finally increased to 336 nm with >100% volume expansion at the end of sodiation (Figure 17b). The crack and pores were formed during desodiation process with the nanowire shrank from 336 to 273 nm (Figure 17c). Single-crystalline  $\text{ZnO}$  nanowires are also systematically studied by in situ TEM to visualize the microstructural evolution and phase transformation.<sup>[133]</sup> During the first sodiation, the sharp trip of the  $\text{ZnO}$  nanowire was completely disappeared due to the volume expansion. After an additional sodiation of 16 min, the length of the  $\text{ZnO}$  nanowire was  $\approx 1307$  nm, corresponding to a 30.7% of elongation ratio (Figure 17d). Moreover, the electron diffraction patterns of sodiated products demonstrate the formation of  $\text{NaZn}_{13}$  and  $\text{Na}_2\text{O}$  phases. The slow and step-by-step electrochemical sodiation process of  $\text{ZnO}$  nanowire was also investigated in this work, and it revealed an unexpectedly fast and uniform sodiation process, which is owed to the large amount of ion interconnected transport channels. Conversion-type  $\text{V}_2\text{O}_3$  anodes have been extensively investigated as a promising anode in SIBs because of its high theoretical capacity, abundant resources, and low cost.<sup>[134,138]</sup> Our group presents the design of multidimensionally assembled nanoarchitecture anode,  $\text{V}_2\text{O}_3/\text{CNTs}/\text{rGO}$ , for high performance SIBs.<sup>[134]</sup> The advanced in situ TEM experiments were performed to probe the morphology changes and evolutions. The schematic diagram of the nanoscale sodium-ion half cells is displayed in Figure 17e.g. For the  $\text{V}_2\text{O}_3/\text{CNTs}$ , the  $\text{V}_2\text{O}_3$  nanoparticles increased and some small cracked pores are observed during the sodiation process. Moreover, an evident volume expansion of the sodiated  $\text{V}_2\text{O}_3/\text{CNTs}$  compared to original nanotubes can be detected after 500 s (Figure 17f). For  $\text{V}_2\text{O}_3/\text{CNTs}/\text{rGO}$ , the bent rGO nanosheets are observed to

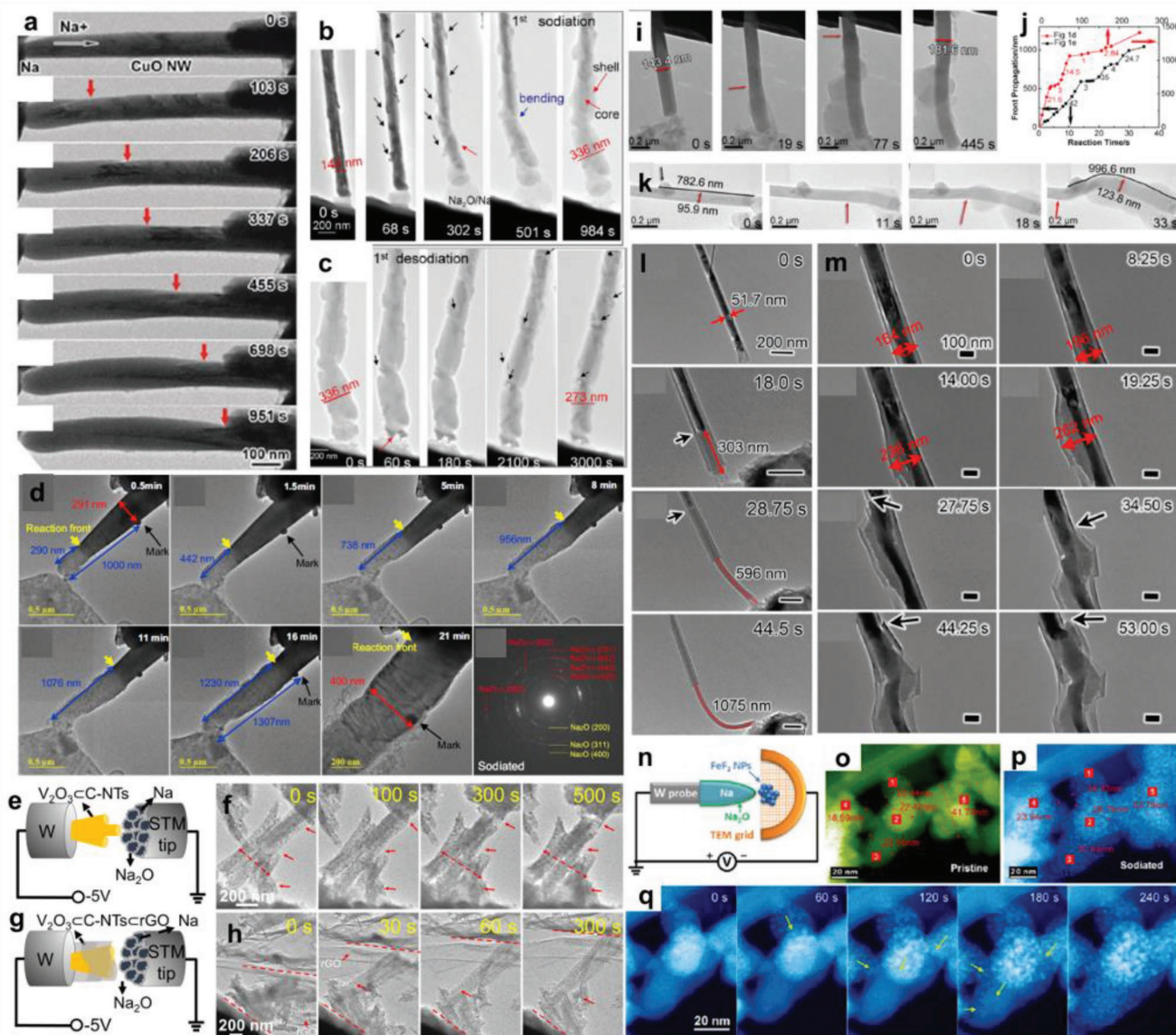


**Figure 17.** a) Time-lapse images showing the evolution of morphology of a CuO NW at an applied voltage of  $-3$  V during the first sodiation process. b,c) In situ TEM images showing the 1st sodiation and the 1st desodiation of the single SnO<sub>2</sub> nanowire, respectively. d) Time-resolved TEM images from video frames show morphology and structure evolution as a function of sodiation time and its electron diffraction (ED) patterns. Schematic and structural evolution of e,f) V<sub>2</sub>O<sub>3</sub>/C-NTs and g,h) V<sub>2</sub>O<sub>3</sub>/C-NTs/rGO electrodes observed by in situ TEM experiments, respectively, during constant potential discharge at 5 V. i,k) The morphology evolution of two  $\alpha$ -MoO<sub>3</sub> nanobelts during the first sodiation process in a low magnification, in which the red arrows denote the reaction front. j) The measured relationship between the sodiation front position and the sodiation time for above two  $\alpha$ -MoO<sub>3</sub> nanobelts. l) Time-resolved TEM images from video frames show the sodiation process of an individual Co<sub>9</sub>S<sub>8</sub>-filled CNT with an open end. All scale bars are 200 nm. m) Time-resolved TEM images from video frames reveal the appearance of fractures during the electrochemical sodiation process of an individual Co<sub>9</sub>S<sub>8</sub>-filled CNT with closed ends. All scale bars are 100 nm. n) Schematic showing the setup of the in situ experiment. HAADF-STEM images showing o) pristine and p) sodiated FeF<sub>2</sub> NPs and q) cropped time-lapse frames throughout the sodiation process. a) Reproduced with permission.<sup>[131]</sup> Copyright 2015, Royal Society of Chemistry. b,c) Reproduced with permission.<sup>[132]</sup> Copyright 2013, American Chemical Society. d) Reproduced with permission.<sup>[133]</sup> Copyright 2016, Elsevier. e-h) Reproduced with permission.<sup>[134]</sup> Copyright 2018, Wiley-VCH. i-k) Reproduced with permission.<sup>[135]</sup> Copyright 2016, Elsevier. l,m) Reproduced with permission.<sup>[136]</sup> Copyright 2014, American Chemical Society. n-q) Reproduced with permission.<sup>[137]</sup> Copyright 2014, American Chemical Society.

continually stretch with the slight expansion of the V<sub>2</sub>O<sub>3</sub>/C-NTs (Figure 17h), indicating the rGO buffer framework plays a critical role in long-term sodiation/desodiation processes. In situ XRD and ex situ XPS analysis results demonstrated that the V<sub>2</sub>O<sub>3</sub> nanoparticles partially converted to V metal.

The  $\alpha$ -MoO<sub>3</sub> with a unique layered structure has been studied as a well-known sodium insertion compound, but the fundamental electrochemical reaction mechanisms and the phase transformation pathways are still rare.<sup>[139]</sup> Sun and co-workers<sup>[135]</sup> observed the  $\alpha$ -MoO<sub>3</sub> nanobelts undergo a unique

multistep phase evolution by in situ TEM. The radial expansions of the  $\alpha$ - $\text{MoO}_3$  nanobelts are  $\approx 26.6\%$  and  $\approx 29.1\%$ , respectively, compared to their original state (Figure 17i,k). From the plotted sodiation length versus time curves, the sodiation ratio which was reflected by the slope exhibits step wise increase feature (Figure 17j). During sodiation process, the  $\alpha$ - $\text{MoO}_3$  nanobelt is initially sodiated to amorphous  $\text{Na}_x\text{MoO}_3$ . And then, the intermediate phase is converted into crystalline  $\text{NaMoO}_2$ . Finally, the  $\text{NaMoO}_2$  was further sodiated to Mo metal nanoparticles surrounded by  $\text{Na}_2\text{O}$  matrix after fully sodiation. Therefore, the advanced in situ TEM experiment results provide direct evidences for deeply understanding the sodium storage mechanism of the  $\alpha$ - $\text{MoO}_3$  nanobelt anode for SIBs. The phase transformation and microstructural evolution of  $\text{Co}_9\text{S}_8$ -filled CNT during the initial sodiation were revealed by constructing an in situ cell inside TEM.<sup>[136]</sup> The sodiated phase showed a lighter contrast with a length of about 1075 nm after 44.5 s, indicating that the volume expansion is through axial elongation (Figure 17l). The diameter of filled CNT expanded from 164 to 282 nm when sodiated to 19.25 s. However, volume expansion and pulverization of the  $\text{Co}_9\text{S}_8$ -filled CNT propagated quickly after 27.75 s. Many cracks and fractures were observed when continuous sodiation (Figure 17m). Moreover, the selected area electron diffraction (SAED) pattern results demonstrated that the  $\text{Co}_9\text{S}_8$  was converted to Co metal and  $\text{Na}_2\text{S}$  during the electrochemical sodiation.  $\text{FeF}_2$  is another conversion-type anode material for SIBs. Su and co-workers revealed a complex sodiation mechanism of  $\text{FeF}_2$  anode by in situ TEM technique.<sup>[137]</sup> Figure 17n shows the detailed structure of the in situ cell. Before sodiation, the average size of the

$\text{FeF}_2$  nanoparticles is around 10–20 nm (Figure 17o). After sodiation, the volume of the each  $\text{FeF}_2$  nanoparticle will increase  $\approx 30\%$  (Figure 17p). From the in situ dynamic TEM images,  $\text{FeF}_2$  nanoparticles were gradually sodiated through the directly connected particles until fully sodiated (Figure 17q). That interesting work revealed that the  $\text{FeF}_2$  nanoparticle underwent two reaction mechanisms during sodiation process: 1) conversion-type reaction on surface and 2) disproportionation reaction in the core of the particles.

### 6.3. In Situ Raman

In situ Raman spectroscopy is an effective method to detect the formation process of SEI and electrochemical energy storage mechanism, since Raman peaks are very sensitive to composition and phase evolutions for the conversion-type anodes.<sup>[140]</sup> Fan and co-workers employed advanced in situ Raman tests to track the sodiation/desodiation processes of  $\text{MoS}_{2-x}\text{Se}_x$  anode.<sup>[141]</sup> The in situ Raman measurements of  $\text{MoS}_{2-x}\text{Se}_x$  anode during initial electrochemical processes in two work voltage ranges of 0.5–3.0 and 0.01–3.0 V (Figure 18). In the range of the 0.5–3.0 V, the Mo–Se and Mo–S peaks are gradually getting weaker until they disappear when discharged to 0.5 V (Figure 18a) and all of the peaks can be reappeared and gradually strengthen in the subsequent charge process (Figure 18b). By contrast, the Mo–Se and Mo–S peaks are also gradually disappearing when discharged to 0.01 V (Figure 18c), but all of the peaks never reappeared when the cell charged back to 3.0 V (Figure 18d). The in situ Raman analysis results

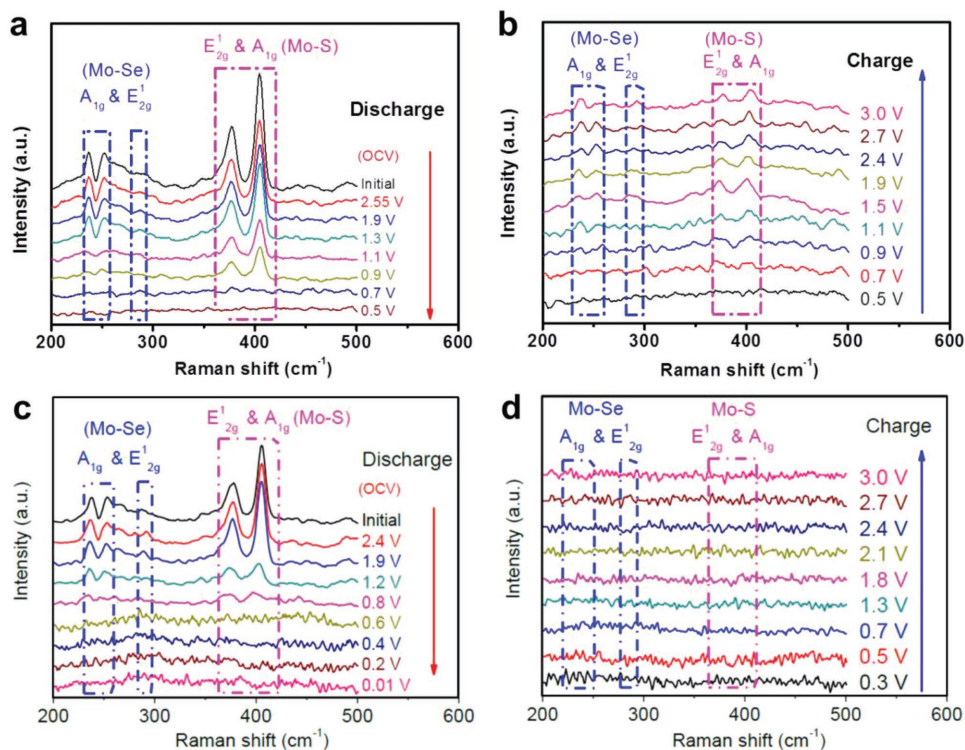


**Figure 18.** In situ Raman spectra of the  $\text{MoS}_{2-x}\text{Se}_x/\text{GF}$  electrode during the first sodiation and desodiation processes in two discharge/charge potential ranges: a,b) 0.5–3.0 V and c,d) 0.01–3.0 V. a–d) Reproduced with permission.<sup>[141]</sup> Copyright 2018, Elsevier.

demonstrated that the 2D layered crystal structure of  $\text{MoS}_{2-x}\text{Se}_x$  would be destroyed due to the conversion-type reaction. This work reveals that the optimization of the voltage range will give full play to the advantages of the 2D structure and achieving an excellent cycling performance.

## 7. Conclusions and Perspective

In summary, we have reviewed the recent progresses on nanostructured conversion-type negative electrode materials for SIBs. Conversion-type anodes are particularly promising and advantageous because of their high theoretical capacity, low cost, and tunable operation voltages. Nevertheless, many obstacles such as low ionic/electrical conductivity, large volume expansion, and undesirable side-reactions need to be tackled. To circumvent these problems, some research works have been done to explore effective strategies. Specifically, these strategies can be categorized into structure design, carbon modification, and electrolyte optimization. Structure design, such as low-dimensional nanostructure engineering and hierarchical porous architectures, can offer short ion diffusion path, increased active sites, and large void space, enhancing their reaction kinetics and alleviating the volume expansion. The construction of various carbon nanocomposites enhances the electrical conductivity and structural stability of electrodes, improving their overall electrochemical performance. The electrolyte optimization effectively minimizes the undesirable side reactions and capacity loss, improving the long-term cycling performance of electrodes. As a result, the adoption of these effective strategies can significantly enhance the sodium storage property of conversion-type anode materials.

Although the great advances have achieved in the synthesis of conversion-type anodes and their application in SIBs, many challenges still exist and need to be overcome. The most current methods for fabricating well-designed nanostructured conversion-type anodes involve complicated synthesis process and high cost. Facile and cost-effective synthetic strategies should be explored to prepare conversion-type anodes with well-defined structures. In addition, the substantial structural rearrangement and phase changes during initial few cycles cause voltage hysteresis issues, leading to poor cycling property. The in-depth understanding of intrinsic reaction mechanism and kinetics analysis are urgently required. To achieve a significant breakthrough in the electrochemical performance of conversion-type anodes, it is essential to use the theoretical calculation and advanced in situ characterization for further investigating the structure–property relationships of electrodes. Despite existing challenges, it is optimistic that the reasonable structure design and composition will promote the development of conversion-type anodes for SIBs.

## Acknowledgements

This work was supported by the National Key Research and Development Program of China (Grant Nos. 2016YFA0202603 and 2016YFA0202601), the Program of Introducing Talents of Discipline to Universities (Grant No. B17034), the National Natural Science Foundation of China (Grant Nos. 51521001 and 51602239), the National Natural Science

Fund for Distinguished Young Scholars (Grant No. 51425204), and the Hubei Provincial Natural Science Foundation of China (Grant No. 2016CFB267).

## Conflict of Interest

The authors declare no conflict of interest.

## Keywords

advanced characterization techniques, conversion-type anodes, optimization strategies, sodium-ion batteries

Received: June 29, 2018

Revised: July 25, 2018

Published online:

- 
- [1] J. M. Tarascon, M. Armand, *Nature* **2001**, 414, 359.  
 [2] M. Lao, Y. Zhang, W. Luo, Q. Yan, W. Sun, S. X. Dou, *Adv. Mater.* **2017**, 29, 1700622.  
 [3] Z. Hu, Q. Liu, S. L. Chou, S. X. Dou, *Adv. Mater.* **2017**, 29, 1700606.  
 [4] M. R. Palacin, *Chem. Soc. Rev.* **2009**, 38, 2565.  
 [5] a) Y. Wen, K. He, Y. Zhu, F. Han, Y. Xu, I. Matsuda, Y. Ishii, J. Cummings, C. Wang, *Nat. Commun.* **2014**, 5, 4033; b) S. Q. Wang, L. Xia, L. Yu, L. Zhang, H. H. Wang, X. W. Lou, *Adv. Energy Mater.* **2016**, 6, 1502217; c) H. S. Hou, X. Q. Qiu, W. F. Wei, Y. Zhang, X. B. Ji, *Adv. Energy Mater.* **2017**, 7, 1602898; d) D. Wu, X. Li, B. Xu, N. Twu, L. Liu, G. Ceder, *Energy Environ. Sci.* **2015**, 8, 195; e) S. H. Guo, J. Yi, Y. Sun, H. S. Zhou, *Energy Environ. Sci.* **2016**, 9, 2978; f) Z. Le, F. Liu, P. Nie, X. Li, X. Liu, Z. Bian, G. Chen, H. B. Wu, Y. Lu, *ACS Nano* **2017**, 11, 2952.  
 [6] a) Y. C. Liu, N. Zhang, L. F. Jiao, Z. L. Tao, J. Chen, *Adv. Funct. Mater.* **2015**, 25, 214; b) W. Luo, P. F. Zhang, X. P. Wang, Q. D. Li, Y. F. Dong, J. C. Hua, L. Zhou, L. Q. Mai, *J. Power Sources* **2016**, 304, 340; c) Y. Liu, A. Zhang, C. Shen, Q. Liu, X. Cao, Y. Ma, L. Chen, C. Lau, T. C. Chen, F. Wei, C. Zhou, *ACS Nano* **2017**, 11, 5530.  
 [7] a) B. Zhang, G. Rousse, D. Foix, R. Dugas, D. A. D. Corte, J. Tarascon, *Adv. Mater.* **2016**, 28, 9824; b) S. Liu, J. Feng, X. Bian, J. Liu, H. Xu, *Energy Environ. Sci.* **2016**, 9, 1229.  
 [8] a) Y. P. Zhou, W. P. Sun, X. H. Rui, Y. Zhou, W. J. Ng, Q. Y. Yan, E. Fong, *Nano Energy* **2016**, 21, 71; b) Y. Xiao, J.-Y. Hwang, I. Belharouak, Y.-K. Sun, *ACS Energy Lett.* **2017**, 2, 364; c) Y. Zhang, Q. Zhou, J. X. Zhu, Q. Y. Yan, S. X. Dou, W. P. Sun, *Adv. Funct. Mater.* **2017**, 27, 1702317; d) W. Li, S. L. Chou, J. Z. Wang, J. H. Kim, H. K. Liu, S. X. Dou, *Adv. Mater.* **2014**, 26, 4037; e) X. Wang, H. M. Kim, Y. Xiao, Y. K. Sun, *J. Mater. Chem. A* **2016**, 4, 14915; f) P. Ge, H. Hou, S. Li, L. Yang, X. Ji, *Adv. Funct. Mater.* **2018**, 28, 1801765; g) Y. Xiao, D. Su, X. Wang, S. Wu, L. Zhou, Y. Shi, S. Fang, H. M. Cheng, F. Li, *Adv. Energy Mater.* **2018**, 8, 1800930.  
 [9] F. Klein, B. Jache, A. Bhide, P. Adelhelm, *Phys. Chem. Chem. Phys.* **2013**, 15, 15876.  
 [10] Y. Lu, Y. Yu, X. W. Lou, *Chem.* **2018**, 4, 972.  
 [11] a) J. Meng, H. Guo, C. Niu, Y. Zhao, L. Xu, Q. Li, L. Mai, *Joule* **2017**, 1, 522; b) H. Zhang, I. Hasa, S. Passerini, *Adv. Energy Mater.* **2018**, 8, 1702582; c) P. Xiao, F. Bu, R. Zhao, M. F. Aly Aboud, I. Shakir, Y. Xu, *ACS Nano* **2018**, 12, 3947.  
 [12] a) L. Zhou, Z. Zhuang, H. Zhao, M. Lin, D. Zhao, L. Mai, *Adv. Mater.* **2017**, 29, 1602914; b) X. Y. Yu, X. W. Lou, *Adv. Energy*

- Mater.* **2018**, *8*, 1701592; c) Q. Wei, F. Xiong, S. Tan, L. Huang, E. H. Lan, B. Dunn, L. Mai, *Adv. Mater.* **2017**, *29*, 1602300.
- [13] a) Y. Zhao, L. P. Wang, M. T. Sougrati, Z. X. Feng, Y. Leconte, A. Fisher, M. Srinivasan, Z. C. Xu, *Adv. Energy Mater.* **2017**, *7*, 1601424; b) S. H. Yu, X. Feng, N. Zhang, J. Seok, H. D. Abruna, *Acc. Chem. Res.* **2018**, *51*, 273.
- [14] F. Wu, C. Zhao, S. Chen, Y. Lu, Y. Hou, Y.-S. Hu, J. Maier, Y. Yu, *Mater. Today* **2018**, <https://doi.org/10.1016/j.mattod.2018.03.004>.
- [15] a) F. Zhao, S. Shen, L. Cheng, L. Ma, J. Zhou, H. Ye, N. Han, T. Wu, Y. Li, J. Lu, *Nano Lett.* **2017**, *17*, 4137; b) M. Walter, T. Zund, M. V. Kovalenko, *Nanoscale* **2015**, *7*, 9158; c) L. Mai, J. Sheng, L. Xu, S. Tan, J. Meng, *Acc. Chem. Res.* **2018**, *51*, 950; d) L. Mai, X. Tian, X. Xu, L. Chang, L. Xu, *Chem. Rev.* **2014**, *114*, 11828.
- [16] a) T. Jin, Q. Han, Y. Wang, L. Jiao, *Small* **2018**, *14*, 1703086; b) X. Xu, C. Niu, M. Duan, X. Wang, L. Huang, J. Wang, L. Pu, W. Ren, C. Shi, J. Meng, B. Song, L. Mai, *Nat. Commun.* **2017**, *8*, 460; c) X. Xia, D. Chao, Y. Zhang, J. Zhan, Y. Zhong, X. Wang, Y. Wang, Z. Shen, J. Tu, H. Fan, *Small* **2016**, *12*, 3048.
- [17] a) Y. Xiao, J.-Y. Hwang, I. Belharouak, Y.-K. Sun, *Nano Energy* **2017**, *32*, 320; b) L. M. Zhou, K. Zhang, Z. Hu, Z. L. Tao, L. Q. Mai, Y. M. Kang, S. L. Chou, J. Chen, *Adv. Energy Mater.* **2018**, *8*, 1701415.
- [18] a) Y. Wang, W. Kang, D. Cao, M. Zhang, Z. Kang, Z. Xiao, R. Wang, D. Sun, *J. Mater. Chem. A* **2018**, *6*, 4776; b) M. Jing, Z. Chen, Z. Li, F. Li, M. Chen, M. Zhou, B. He, L. Chen, Z. Hou, X. Chen, *ACS Appl. Mater. Interfaces* **2018**, *10*, 704.
- [19] Y. He, P. Xu, B. Zhang, Y. Du, S. Bo, X. Han, H. Peng, *ACS Appl. Mater. Interfaces* **2017**, *9*, 38401.
- [20] Y. C. Du, X. S. Zhu, X. S. Zhou, L. Y. Hu, Z. H. Dai, J. C. Bao, *J. Mater. Chem. A* **2015**, *3*, 6787.
- [21] W. Huang, H. Sun, H. Shangguan, X. Cao, X. Xiao, F. Shen, K. Molhave, L. Ci, P. Si, J. Zhang, *Nanoscale* **2018**, *10*, 7851.
- [22] Y. Lin, Z. Qiu, D. Li, S. Ullah, H. Yang, H. Xin, W. Liao, B. Yang, H. Fan, J. Xu, C. Zhu, *Energy Storage Mater.* **2018**, *11*, 67.
- [23] G. L. Xu, R. Amine, A. Abouimrane, H. Che, M. Dahbi, Z. F. Ma, I. Saadoun, J. Alami, W. L. Mattis, F. Pan, Z. Chen, K. Amine, *Adv. Energy Mater.* **2018**, *8*, 1702403.
- [24] K. Zhang, Z. Hu, X. Liu, Z. Tao, J. Chen, *Adv. Mater.* **2015**, *27*, 3305.
- [25] D. W. Su, K. Kretschmer, G. X. Wang, *Adv. Energy Mater.* **2016**, *6*, 1501785.
- [26] a) C. Wu, S. X. Dou, Y. Yu, *Small* **2018**, *14*, 1703671; b) Y. X. Wang, K. H. Seng, S. L. Chou, J. Z. Wang, Z. Guo, D. Wexler, H. K. Liu, S. X. Dou, *Chem. Commun.* **2014**, *50*, 10730.
- [27] M. K. Devaraju, I. Honma, *Adv. Energy Mater.* **2012**, *2*, 284.
- [28] a) W. N. Ren, H. F. Zhang, C. Guan, C. W. Cheng, *Adv. Funct. Mater.* **2017**, *27*, 1702116; b) X. M. Geng, Y. C. Jiao, Y. Han, A. Mukhopadhyay, L. Yang, H. L. Zhu, *Adv. Funct. Mater.* **2017**, *27*, 1702998; c) F. E. Niu, J. Yang, N. N. Wang, D. P. Zhang, W. L. Fan, J. Yang, Y. T. Qian, *Adv. Funct. Mater.* **2017**, *27*, 1700522.
- [29] X. J. Wei, C. J. Tang, Q. Y. An, M. Y. Yan, X. P. Wang, P. Hu, X. Y. Cai, L. Q. Mai, *Nano Res.* **2017**, *10*, 3202.
- [30] K. Zhang, M. Park, L. Zhou, G.-H. Lee, W. Li, Y.-M. Kang, J. Chen, *Adv. Funct. Mater.* **2016**, *26*, 6728.
- [31] K. Zhang, M. Park, L. Zhou, G. H. Lee, J. Shin, Z. Hu, S. L. Chou, J. Chen, Y. M. Kang, *Angew. Chem., Int. Ed.* **2016**, *55*, 12822.
- [32] K. Chen, W. Zhang, L. Xue, W. Chen, X. Xiang, M. Wan, Y. Huang, *ACS Appl. Mater. Interfaces* **2017**, *9*, 1536.
- [33] W. Zhao, C. Guo, C. M. Li, *J. Mater. Chem. A* **2017**, *5*, 19195.
- [34] Q. Li, Q. Wei, W. Zuo, L. Huang, W. Luo, Q. An, V. O. Pelenovich, L. Mai, Q. Zhang, *Chem. Sci.* **2017**, *8*, 160.
- [35] I. Bilecka, M. Niederberger, *Nanoscale* **2010**, *2*, 1358.
- [36] a) D. Li, D. Yan, X. Zhang, J. Li, T. Lu, L. Pan, *J. Colloid Interface Sci.* **2017**, *497*, 350; b) J. Xiang, D. Dong, F. Wen, J. Zhao, X. Zhang, L. Wang, Z. Liu, *J. Alloys Compd.* **2016**, *660*, 11.
- [37] J. Li, D. Yan, T. Lu, W. Qin, Y. Yao, L. Pan, *ACS Appl. Mater. Interfaces* **2017**, *9*, 2309.
- [38] W. Qin, T. Q. Chen, T. Lu, D. H. C. Chua, L. K. Pan, *J. Power Sources* **2016**, *302*, 202.
- [39] W. Qin, T. Q. Chen, L. K. Pan, L. Y. Niu, B. W. Hu, D. S. Li, J. L. Li, Z. Sun, *Electrochim. Acta* **2015**, *153*, 55.
- [40] Z.-J. Zhang, Y.-X. Wang, S.-L. Chou, H.-J. Li, H.-K. Liu, J.-Z. Wang, *J. Power Sources* **2015**, *280*, 107.
- [41] X. Liu, T. Chen, H. Chu, L. Niu, Z. Sun, L. Pan, C. Q. Sun, *Electrochim. Acta* **2015**, *166*, 12.
- [42] Y. W. Zhu, S. Murali, M. D. Stoller, A. Velamakanni, R. D. Piner, R. S. Ruoff, *Carbon* **2010**, *48*, 2118.
- [43] X. J. Zhang, T. Q. Chen, D. Yan, W. Qin, B. W. Hu, Z. Sun, L. K. Pan, *Electrochim. Acta* **2015**, *180*, 616.
- [44] X. Y. Yang, L. H. Chen, Y. Li, J. C. Rooke, C. Sanchez, B. L. Su, *Chem. Soc. Rev.* **2017**, *46*, 481.
- [45] Q. Guo, Y. Ma, T. Chen, Q. Xia, M. Yang, H. Xia, Y. Yu, *ACS Nano* **2017**, *11*, 12658.
- [46] T. Chen, Y. Ma, Q. Guo, M. Yang, H. Xia, *J. Mater. Chem. A* **2017**, *5*, 3179.
- [47] a) Y. X. Wang, J. Yang, S. L. Chou, H. K. Liu, W. X. Zhang, D. Zhao, S. X. Dou, *Nat. Commun.* **2015**, *6*, 8689; b) Y. Tang, Z. Zhao, Y. Wang, Y. Dong, Y. Liu, X. Wang, J. Qiu, *Electrochim. Acta* **2017**, *225*, 369; c) B. Fu, X. Zhou, Y. P. Wang, *Mater. Lett.* **2016**, *170*, 21.
- [48] a) J. W. Jung, C. L. Lee, S. Yu, I. D. Kim, *J. Mater. Chem. A* **2016**, *4*, 703; b) H. G. Wang, S. Yuan, D. L. Ma, X. B. Zhang, J. M. Yan, *Energy Environ. Sci.* **2015**, *8*, 1660.
- [49] X. Wang, Y. Liu, Y. Wang, L. Jiao, *Small* **2016**, *12*, 4865.
- [50] C. Zhu, X. Mu, P. A. van Aken, Y. Yu, J. Maier, *Angew. Chem., Int. Ed.* **2014**, *53*, 2152.
- [51] X. Xiong, W. Luo, X. Hu, C. Chen, L. Qie, D. Hou, Y. Huang, *Sci. Rep.* **2015**, *5*, 9254.
- [52] J. S. Cho, J. K. Lee, Y. C. Kang, *Sci. Rep.* **2016**, *6*, 23699.
- [53] J. S. Cho, S. Y. Lee, Y. C. Kang, *Sci. Rep.* **2016**, *6*, 23338.
- [54] Q. H. Wang, W. C. Zhang, C. Guo, Y. J. Liu, C. Wang, Z. P. Guo, *Adv. Funct. Mater.* **2017**, *27*, 1703390.
- [55] X. Li, J. Li, Q. Gao, X. Yu, R. Hu, J. Liu, L. Yang, M. Zhu, *Electrochim. Acta* **2017**, *254*, 172.
- [56] Y. Q. Teng, M. S. Mo, Y. Li, J. L. Xue, H. L. Zhao, *J. Alloys Compd.* **2018**, *744*, 712.
- [57] Z. Liu, T. Lu, T. Song, X.-Y. Yu, X. W. Lou, U. Paik, *Energy Environ. Sci.* **2017**, *10*, 1576.
- [58] Y. Liu, X. He, D. Hanlon, A. Harvey, J. N. Coleman, Y. Li, *ACS Nano* **2016**, *10*, 8821.
- [59] J. H. Kim, Y. C. Kang, *Nano Res.* **2017**, *10*, 3178.
- [60] a) N. Zhang, X. Han, Y. Liu, X. Hu, Q. Zhao, J. Chen, *Adv. Energy Mater.* **2015**, *5*, 1401123; b) G. Xia, Q. Gao, D. Sun, X. Yu, *Small* **2017**, *13*, 1701561; c) C. Li, Q. Hu, Y. Li, H. Zhou, Z. Lv, X. Yang, L. Liu, H. Guo, *Sci. Rep.* **2016**, *6*, 25556; d) T. Li, A. Qin, L. Yang, J. Chen, Q. Wang, D. Zhang, H. Yang, *ACS Appl. Mater. Interfaces* **2017**, *9*, 19900; e) D. Li, J. Zhou, X. Chen, H. Song, *ACS Appl. Mater. Interfaces* **2016**, *8*, 30899.
- [61] Y. Liu, N. Zhang, C. Yu, L. Jiao, J. Chen, *Nano Lett.* **2016**, *16*, 3321.
- [62] Q. He, K. Rui, C. Chen, J. Yang, Z. Wen, *ACS Appl. Mater. Interfaces* **2017**, *9*, 36927.
- [63] a) Y. Wu, J. Meng, Q. Li, C. Niu, X. Wang, W. Yang, W. Li, L. Mai, *Nano Res.* **2017**, *10*, 2364; b) D. Chen, L. Peng, Y. Yuan, Y. Zhu, Z. Fang, C. Yan, G. Chen, R. Shahbazian-Yassar, J. Lu, K. Amine, G. Yu, *Nano Lett.* **2017**, *17*, 3907; c) H. Kim, H. Kim, H. Kim, J. Kim, G. Yoon, K. Lim, W. S. Yoon, K. Kang, *Adv. Funct. Mater.* **2016**, *26*, 5042.
- [64] J. P. Yang, T. F. Zhou, R. Zhu, X. Q. Chen, Z. P. Guo, J. W. Fan, H. K. Liu, W. X. Zhang, *Adv. Mater. Interfaces* **2016**, *3*, 1500464.

- [65] H. H. Li, Z. Y. Li, X. L. Wu, L. L. Zhang, C. Y. Fan, H. F. Wang, X. Y. Li, K. Wang, H. Z. Sun, J. P. Zhang, *J. Mater. Chem. A* **2016**, *4*, 8242.
- [66] W. Kang, Y. Zhang, L. Fan, L. Zhang, F. Dai, R. Wang, D. Sun, *ACS Appl. Mater. Interfaces* **2017**, *9*, 10602.
- [67] a) R. Alcántara, M. Jaraba, P. Lavela, J. L. Tirado, *Chem. Mater.* **2002**, *14*, 2847; b) L. J. Wu, J. W. Lang, P. Zhang, X. Zhang, R. S. Guo, X. B. Yan, *J. Mater. Chem. A* **2016**, *4*, 18392; c) X. Wang, K. Cao, Y. Wang, L. Jiao, *Small* **2017**, *13*, 1700873; d) G. Fang, J. Zhou, Y. Cai, S. Liu, X. Tan, A. Pan, S. Liang, *J. Mater. Chem. A* **2017**, *5*, 13983.
- [68] F. Zou, Y. M. Chen, K. Liu, Z. Yu, W. Liang, S. M. Bhoway, M. Gao, Y. Zhu, *ACS Nano* **2016**, *10*, 377.
- [69] W. P. Sun, X. H. Rui, J. X. Zhu, L. H. Yu, Y. Zhang, Z. C. Xu, S. Madhavi, Q. Y. Yan, *J. Power Sources* **2015**, *274*, 755.
- [70] L. Chang, K. Wang, L. A. Huang, Z. S. He, H. B. Shao, J. M. Wang, *New J. Chem.* **2017**, *41*, 14072.
- [71] S. Yuan, X. L. Huang, D. L. Ma, H. G. Wang, F. Z. Meng, X. B. Zhang, *Adv. Mater.* **2014**, *26*, 2273.
- [72] Y. Lu, N. Zhang, Q. Zhao, J. Liang, J. Chen, *Nanoscale* **2015**, *7*, 2770.
- [73] C. C. Chen, Y. Y. Dong, S. Y. Li, Z. H. Jiang, Y. J. Wang, L. F. Jiao, H. T. Yuan, *J. Power Sources* **2016**, *320*, 20.
- [74] P. Chandra Rath, J. Patra, D. Saikia, M. Mishra, J.-K. Chang, H.-M. Kao, *J. Mater. Chem. A* **2016**, *4*, 14222.
- [75] X. Zhang, W. Qin, D. Li, D. Yan, B. Hu, Z. Sun, L. Pan, *Chem. Commun.* **2015**, *51*, 16413.
- [76] a) Y. Chen, X. Hu, B. Evanko, X. Sun, X. Li, T. Hou, S. Cai, C. Zheng, W. Hu, G. D. Stucky, *Nano Energy* **2018**, *46*, 117; b) D. Li, D. Yang, X. Yang, Y. Wang, Z. Guo, Y. Xia, S. Sun, S. Guo, *Angew. Chem.* **2016**, *128*, 1; c) S. Y. Lee, Y. C. Kang, *Chem.* **2016**, *22*, 2769; d) W. H. Chen, S. H. Qi, L. Q. Guan, C. T. Liu, S. Z. Cui, C. Y. Shen, L. W. Mi, *J. Mater. Chem. A* **2017**, *5*, 5332.
- [77] J. S. Cho, J.-S. Park, Y. C. Kang, *Nano Res.* **2016**, *10*, 897.
- [78] Z. J. Cao, H. H. Song, B. Cao, J. Ma, X. H. Chen, J. S. Zhou, Z. K. Ma, *J. Power Sources* **2017**, *364*, 208.
- [79] L. Li, S. Peng, N. Bucher, H.-Y. Chen, N. Shen, A. Nagasubramanian, E. Eldho, S. Hartung, S. Ramakrishna, M. Srinivasan, *Nano Energy* **2017**, *37*, 81.
- [80] F. Han, C. Z. Zhang, B. Sun, W. Tang, J. X. Yang, X. K. Li, *Carbon* **2017**, *118*, 731.
- [81] Q. D. Li, L. Li, K. A. Owusu, W. Luo, Q. Y. An, Q. L. Wei, Q. J. Zhang, L. Q. Mai, *Nano Energy* **2017**, *41*, 109.
- [82] L. M. Zhou, K. Zhang, J. Z. Sheng, Q. Y. An, Z. L. Tao, Y. M. Kang, J. Chen, L. Q. Mai, *Nano Energy* **2017**, *35*, 281.
- [83] S. Peng, X. Han, L. Li, Z. Zhu, F. Cheng, M. Srinivasan, S. Adams, S. Ramakrishna, *Small* **2016**, *12*, 1359.
- [84] F. Han, C. Y. J. Tan, Z. Q. Gao, *J. Power Sources* **2017**, *339*, 41.
- [85] X. Liu, K. Zhang, K. X. Lei, F. J. Li, Z. L. Tao, J. Chen, *Nano Res.* **2016**, *9*, 198.
- [86] T. Wang, P. Hu, C. Zhang, H. Du, Z. Zhang, X. Wang, S. Chen, J. Xiong, G. Cui, *ACS Appl. Mater. Interfaces* **2016**, *8*, 7811.
- [87] F. P. Zhao, Q. F. Gong, B. Traynor, D. Zhang, J. J. Li, H. L. Ye, F. J. Chen, N. Han, Y. Y. Wang, X. H. Sun, Y. G. Li, *Nano Res.* **2016**, *9*, 3162.
- [88] D. Zhang, W. P. Sun, Y. Zhang, Y. H. Dou, Y. Z. Jiang, S. X. Dou, *Adv. Funct. Mater.* **2016**, *26*, 7479.
- [89] R. Sun, S. Liu, Q. Wei, J. Sheng, S. Zhu, Q. An, L. Mai, *Small* **2017**, *13*, 1701744.
- [90] D. H. Liu, W. H. Li, Y. P. Zheng, Z. Cui, X. Yan, D. S. Liu, J. Wang, Y. Zhang, H. Y. Lu, F. Y. Bai, J. Z. Guo, X. L. Wu, *Adv. Mater.* **2018**, *30*, 1706317.
- [91] Z. Zhang, X. Shi, X. Yang, Y. Fu, K. Zhang, Y. Lai, J. Li, *ACS Appl. Mater. Interfaces* **2016**, *8*, 13849.
- [92] H. Fan, H. Yu, Y. Zhang, J. Guo, Z. Wang, H. Wang, N. Zhao, Y. Zheng, C. Du, Z. Dai, Q. Yan, J. Xu, *Energy Storage Mater.* **2018**, *10*, 48.
- [93] M. Wan, R. Zeng, K. Chen, G. Liu, W. Chen, L. Wang, N. Zhang, L. Xue, W. Zhang, Y. Huang, *Energy Storage Mater.* **2018**, *10*, 114.
- [94] X. Wang, Z. Yang, C. Wang, L. Ma, C. Zhao, J. Chen, X. Zhang, M. Xue, *Nanoscale* **2018**, *10*, 800.
- [95] G. D. Park, Y. C. Kang, *Nanoscale* **2018**, *10*, 8125.
- [96] Y. J. Hong, J. H. Kim, Y. Chan Kang, *J. Mater. Chem. A* **2016**, *4*, 15471.
- [97] C. Wu, Y. Jiang, P. Kopold, P. A. van Aken, J. Maier, Y. Yu, *Adv. Mater.* **2016**, *28*, 7276.
- [98] Y. Zhang, A. Pan, L. Ding, Z. Zhou, Y. Wang, S. Niu, S. Liang, G. Cao, *ACS Appl. Mater. Interfaces* **2017**, *9*, 3624.
- [99] G. D. Park, Y. C. Kang, *Chem.* **2016**, *22*, 4140.
- [100] Y. C. Tang, Z. B. Zhao, X. J. Hao, Y. W. Wang, Y. Liu, Y. N. Hou, Q. Yang, X. Z. Wang, J. S. Qiu, *J. Mater. Chem. A* **2017**, *5*, 13591.
- [101] S.-K. Park, J. K. Kim, Y. Chan Kang, *J. Mater. Chem. A* **2017**, *5*, 18823.
- [102] Y. Fang, X. Y. Yu, X. W. D. Lou, *Adv. Mater.* **2018**, *30*, 1706668.
- [103] P. Ge, H. Hou, S. Li, L. Huang, X. Ji, *ACS Appl. Mater. Interfaces* **2018**, *10*, 14716.
- [104] H. Fan, H. Yu, X. Wu, Y. Zhang, Z. Luo, H. Wang, Y. Guo, S. Madhavi, Q. Yan, *ACS Appl. Mater. Interfaces* **2016**, *8*, 25261.
- [105] S. Zhu, Q. Li, Q. Wei, R. Sun, X. Liu, Q. An, L. Mai, *ACS Appl. Mater. Interfaces* **2017**, *9*, 311.
- [106] X. Yang, J. Zhang, Z. Wang, H. Wang, C. Zhi, D. Y. W. Yu, A. L. Rogach, *Small* **2018**, *14*, 1702669.
- [107] X. J. Xu, J. Liu, J. W. Liu, L. Z. Ouyang, R. Z. Hu, H. Wang, L. C. Yang, M. Zhu, *Adv. Funct. Mater.* **2018**, *28*, 1707573.
- [108] H. Li, J. Jiang, J. Huang, Y. Wang, Y. Peng, Y. Zhang, B. J. Hwang, J. Zhao, *ACS Appl. Mater. Interfaces* **2018**, *10*, 13491.
- [109] C. Tang, X. Wei, X. Cai, Q. An, P. Hu, J. Sheng, J. Zhu, S. Chou, L. Wu, L. Mai, *ACS Appl. Mater. Interfaces* **2018**, *10*, 19626.
- [110] W. J. Zhang, M. Dahbi, S. Amagasa, Y. Yamada, S. Komaba, *Electrochem. Commun.* **2016**, *69*, 11.
- [111] Z. Q. Li, L. Y. Zhang, X. L. Ge, C. X. Li, S. H. Dong, C. X. Wang, L. W. Yin, *Nano Energy* **2017**, *32*, 494.
- [112] K. Zhang, M. Park, J. Zhang, G. H. Lee, J. Shin, Y. M. Kang, *Nano Res.* **2017**, *10*, 4337.
- [113] W. J. Li, Q. R. Yang, S. L. Chou, J. Z. Wang, H. K. Liu, *J. Power Sources* **2015**, *294*, 627.
- [114] D. Zhou, L. Z. Fan, *J. Mater. Chem. A* **2018**, *6*, 2139.
- [115] C. Wu, P. Kopold, P. A. van Aken, J. Maier, Y. Yu, *Adv. Mater.* **2017**, *29*, 1604015.
- [116] X. Miao, R. Yin, X. Ge, Z. Li, L. Yin, *Small* **2017**, *13*, 1702138.
- [117] J. Fullenwarth, A. Darwiche, A. Soares, B. Donnadieu, L. Monconduit, *J. Mater. Chem. A* **2014**, *2*, 2050.
- [118] M. Fan, Y. Chen, Y. Xie, T. Yang, X. Shen, N. Xu, H. Yu, C. Yan, *Adv. Funct. Mater.* **2016**, *26*, 5019.
- [119] F. Zhao, N. Han, W. Huang, J. Li, H. Ye, F. Chen, Y. Li, *J. Mater. Chem. A* **2015**, *3*, 21754.
- [120] Z. H. Cui, C. L. Li, P. F. Yu, M. H. Yang, X. X. Guo, C. L. Yin, *J. Mater. Chem. A* **2015**, *3*, 509.
- [121] M. Kong, K. Liu, J. Ning, J. Zhou, H. Song, *J. Mater. Chem. A* **2017**, *5*, 19280.
- [122] a) G. B. Zhang, T. F. Xiong, L. He, M. Y. Yan, K. N. Zhao, X. Xu, L. Q. Mai, *J. Mater. Sci.* **2017**, *52*, 3697; b) X. Wei, X. Wang, Q. An, C. Han, L. Mai, *Small Methods* **2017**, *1*, 1700083.
- [123] Y. F. Yuan, K. Amine, J. Lu, R. Shahbazian-Yassar, *Nat. Commun.* **2017**, *8*, 15806.
- [124] L. Mai, M. Yan, Y. Zhao, *Nature* **2017**, *546*, 469.
- [125] a) H. Liu, F. C. Strobridge, O. J. Borkiewicz, K. M. Wiaderek, K. W. Chapman, P. J. Chupas, C. P. Grey, *Science* **2014**, *344*, 1252817; b) X. Wang, X. Xu, C. Niu, J. Meng, M. Huang, X. Liu, Z. Liu, L. Mai, *Nano Lett.* **2017**, *17*, 544.
- [126] a) X. Wang, P. Hu, C. Niu, J. Meng, X. Xu, X. Wei, C. Tang, W. Luo, L. Zhou, Q. An, L. Mai, *Nano Energy* **2017**, *35*, 71; b) P. Bleith,

- H. Kaiser, P. Novak, C. Villevieille, *Electrochim. Acta* **2015**, *176*, 18; c) X. P. Wang, C. J. Niu, J. S. Meng, P. Hu, X. M. Xu, X. J. Wei, L. Zhou, K. N. Zhao, W. Luo, M. Y. Yan, L. Q. Mai, *Adv. Energy Mater.* **2015**, *5*, 1500716.
- [127] X. Ou, J. Li, F. Zheng, P. Wu, Q. Pan, X. Xiong, C. Yang, M. Liu, *J. Power Sources* **2017**, *343*, 483.
- [128] X. Ou, X. Liang, F. Zheng, P. Wu, Q. Pan, X. Xiong, C. Yang, M. Liu, *Electrochim. Acta* **2017**, *258*, 1387.
- [129] P. Bleith, P. Novak, C. Villevieille, *J. Electrochem. Soc.* **2013**, *160*, A1534.
- [130] E. M. Erickson, C. Ghanty, D. Aurbach, *J. Phys. Chem. Lett.* **2014**, *5*, 3313.
- [131] H. Liu, F. Cao, H. Zheng, H. Sheng, L. Li, S. Wu, C. Liu, J. Wang, *Chem. Commun.* **2015**, *51*, 10443.
- [132] M. Gu, A. Kushima, Y. Shao, J. G. Zhang, J. Liu, N. D. Browning, J. Li, C. Wang, *Nano Lett.* **2013**, *13*, 5203.
- [133] F. Xu, Z. R. Li, L. J. Wu, Q. P. Meng, H. L. L. Xin, J. Sun, B. H. Ge, L. T. Sun, Y. M. Zhu, *Nano Energy* **2016**, *30*, 771.
- [134] S. Tan, Y. Jiang, Q. Wei, Q. Huang, Y. Dai, F. Xiong, Q. Li, Q. An, X. Xu, Z. Zhu, X. Bai, L. Mai, *Adv. Mater.* **2018**, *30*, 1707122.
- [135] W. Xia, F. Xu, C. Zhu, H. L. Xin, Q. Xu, P. Sun, L. Sun, *Nano Energy* **2016**, *27*, 447.
- [136] Q. Su, G. Du, J. Zhang, Y. Zhong, B. Xu, Y. Yang, S. Neupane, W. Li, *ACS Nano* **2014**, *8*, 3620.
- [137] K. He, Y. N. Zhou, P. Gao, L. P. Wang, N. Pereira, G. G. Amatucci, K. W. Nam, X. Q. Yang, Y. M. Zhu, F. Wang, D. Su, *ACS Nano* **2014**, *8*, 7251.
- [138] X. X. An, H. L. Yang, Y. P. Wang, Y. Tang, S. Q. Liang, A. Q. Pan, G. Z. Cao, *Sci. China Mater.* **2017**, *60*, 717.
- [139] S. Li, H. Hou, Z. Huang, H. Liao, X. Qiu, X. Ji, *Electrochim. Acta* **2017**, *245*, 949.
- [140] J. F. Yan, A. Kraytsberg, Y. Ein-Eli, *J. Power Sources* **2015**, *282*, 294.
- [141] G. Jia, D. Chao, N. H. Tiep, Z. Zhang, H. J. Fan, *Energy Storage Mater.* **2018**, *14*, 136.